Chapter 8

Magnetic Moment Formation in Graphene Detected by Scattering of Pure Spin Currents

8.1 Introduction

Many fascinating predictions have been made regarding magnetism in graphene including the formation of magnetic moments from dopants, defects, and edges [315, 316, 363, 364, 320, 317, 322, 365]. While several experimental techniques provide insight into this problem [330, 309, 329, 328, 327, 325, 324, 326, 332, 333, 165, 366, 367], lack of clear evidence for magnetic moment formation hinders development of this nascent field. Studies based on bulk magnetometry [330, 309, 329, 328, 327, 325, 324, 326] directly measure magnetic properties, but because it measures the total magnetic moment (not just the signal from graphene) it is difficult to rule out artifacts from environmental magnetic impurities. Transport [332, 333, 165] and scanning tunneling microscopy (STM) [366, 367] locally probe the graphene, but so far these measurements have been charge-based, so data are subject to various interpretations [334]. Thus, in order to convincingly demonstrate the formation of magnetic moments inside graphene due to dopants and defects, it is essential to employ techniques that directly probe the intrinsic spin degree-of-freedom of the magnetic moment while ensuring the signal originates from the graphene sheet under investigation.

Here, we utilize pure spin currents to demonstrate that hydrogen adatoms and lattice vacancies generate magnetic moments in single layer graphene. Pure spin currents are injected into graphene spin valve devices and clear signatures of magnetic moment formation emerge in the non-local spin transport signal as hydrogen adatoms or lattice vacancies are systematically introduced in an ultrahigh vacuum (UHV) environment. Specifically, introduction of these point defects generate a characteristic dip in the non-local signal as a function of magnetic field. This feature is due to scattering (relaxation) of pure spin currents by localized magnetic moments in graphene and is explained quantitatively by a phenomenological theory based on spin-spin exchange coupling between conduction electrons and magnetic moments. Furthermore, we observe effective exchange fields due to this spin-spin coupling, which are of interest for novel phenomena and spintronic functionality [190, 210, 199, 207] but have not been seen previously in graphene. This work provides the strongest and most clear evidence for magnetic moment formation in graphene to date, and does so for the following reasons:

(1) certainty that the signal comes from the graphene flake, (2) as a spin-dependent measurement, it directly probes the magnetic moments spin degree of freedom, (3) systematic *in-situ* measurement with appropriate control experiments, (4) comprehensive phenomenological theory developed in conjunction with the experimental data, and (5) the observation of similar effects resulting from hydrogen and vacancies, which are structurally and chemically dissimilar, thereby supporting the mechanism predicted for both systems based on removal of p_z-orbitals from the π-band. Lastly, these results demonstrate a method for utilizing localized magnetic moments to manipulate conduction electron spins and demonstrate magnetic field effect behavior as demonstrated by gate tunability of the effective g-factor.

8.1.1 The Proposed Experiment

For a systematic investigation, the spin transport measurement is first performed on a pristine single layer graphene (SLG) spin valve as a control measurement. Then, dopants/defects are controllably introduced to the SLG and the measurement is repeated. The sample remains in UHV during the entire process. Therefore, observed signatures of magnetic moment formation are caused by the adsorbed hydrogen or lattice vacancies. A schematic of the proposed experiment is displayed in Fig. 8.1.

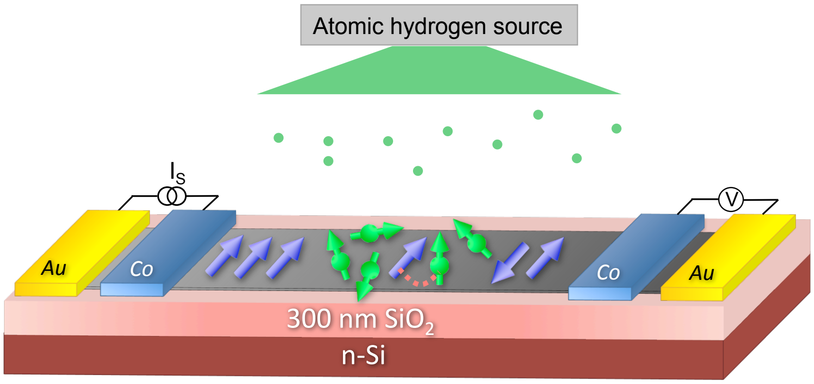

Figure 8.1: Schematic of the *in-situ* deposition of H and Interaction with the Spin Current. The magnetic moments (green arrows) induced by hydrogen doping interact (red dashed line) via exchange with the injected spins (blue arrows) diffusing along the graphene channel.

8.2 Spin Transport in Pristine Graphene

Experiments are performed on non-local SLG spin valves [29, 32, 25] (Fig. 8.2 a)) consisting of two outer Au/Ti electrodes (a and d) and two ferromagnetic (FM) Co electrodes that make contact to SLG across MgO/TiO_2 tunnel barriers (b and c). The Co electrodes are capped with 5 nm Al_2O_3 to protect from hydrogen exposure. The tunnel barrier and capping layer are present only at the site of the FM electrodes, leaving the rest of the graphene uncovered. The device is fabricated on a SiO_2/Si substrate (300 nm thickness of SiO_2) where the Si is used as a back gate. Details of device fabrication are published elsewhere [71, 25, 34].

The charge and spin transport properties of pristine SLG spin valves are measured at 15 K using lock-in techniques. The gate dependent resistivity (ρ_G) of a representative sample A (black curve in Fig. 8.2 b)) exhibits a maximum at the gate voltage (V_G) of 0 V, which defines the Dirac point ($V_D = 0$ V). This sample exhibits mobility (μ) of 6105 cm^2/Vs. To investigate spin transport in the SLG device (Fig. 8.2 a)), a current (I) is applied between electrodes b

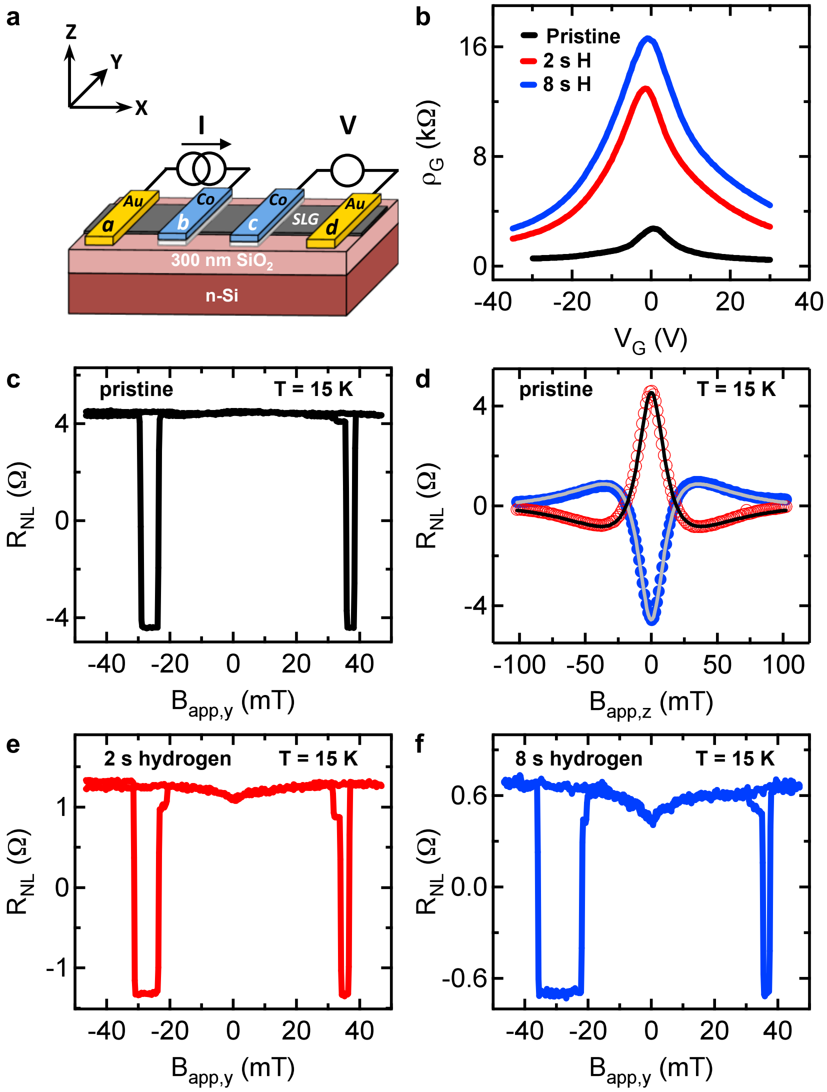

Figure 8.2: The Effect of Hydrogen Exposure on Charge and Spin Transport in SLG at 15 K. a) Schematic illustration of the non-local spin valve device. b) Gate dependent resistivity for the pristine graphene (black) and following exposure to atomic hydrogen for 2 s (red) and 8 s (blue). Upon hydrogen doping, the Dirac point shifts from 0 V to -1 V. c) Non-local spin transport measurement for pristine graphene. d) Hanle spin precession measurement on pristine graphene. e), f) Non-local spin transport measurements after atomic hydrogen exposure for 2 s and 8 s, respectively. Both curves exhibit a dip in R_{NL} at zero applied field, which is caused by spin relaxation induced by localized magnetic moments.

and a, injecting spin-polarized carriers into graphene directly below the FM injector, b. The spin population diffuses along the sample as a pure spin current (x-axis) and the spin density is measured at the FM spin detector, c, as a voltage difference (V) between electrodes c and d. An applied magnetic field ($B_{app,y}$) along the electrode magnetization direction (y-axis) is used to control the relative orientation of spin injector and detector magnetizations. For parallel alignment, the measured non-local resistance ($R_{NL} = V/I$) is positive whereas for antiparallel alignment R_{NL} is negative. The non-local spin signal is defined as the difference between parallel and antiparallel states ($\Delta R_{NL} = R^{P}_{NL} - R^{AP}_{NL}$). A typical scan of R_{NL} as a function of $B_{app,y}$ (Fig. 8.2 c)) displays discrete jumps as the electrode orientation changes between parallel and antiparallel. This sample exhibits a ΔR_{NL} of 8.8 Ω (sample A with $V_G - V_D$ = -15 V). A constant spin-independent background is subtracted from all R_{NL} data presented in this study. Out-of-plane magnetic fields are applied to generate spin precession, and the resulting data (Fig. 8.2 d), red for parallel, blue for antiparallel) are fit by the standard Hanle equation [32, 25] (solid curves) to determine the spin lifetime (τ_{so} = 479 ps) and diffusion coefficient (D = 0.023 m^2/s). The corresponding spin diffusion length is $\lambda = \sqrt{D\tau^{so}}$ = 3.3 μm. Based on these values and a non-local spin signal of 8.8 Ω, the spin polarization of the junction current (P_J) is calculated to be 20% [31].

8.3 Hydrogen Doping of Graphene Spin Valves

A commercial Omicron source is used to expose SLG spin valve devices to atomic hydrogen at 15 K. Diatomic hydrogen is cracked inside a tungsten capillary tube that is heated by electron bombardment. The amount of hydrogen introduced to the chamber is controlled via a leak valve, which is tuned to maintain a chamber pressure of 1×10^{-6} torr (the base pressure of the chamber is below 1×10^{-9} torr). The heating power of the Omicron source is determined by the high voltage (HV) applied to the capillary and the emission current between capillary and filament (I_{em}). We use the parameters HV=1 kV and I_{em}=80 mA. The distance from source to sample is 100 mm. A shutter positioned between the SLG spin valve and hydrogen source is used in order to control the exposure time. Additionally, deflector plates are used to steer any charged ions away from the sample.

The exposure of SLG spin valves to atomic hydrogen substantially modifies charge transport properties, such as ρ_G and μ (Fig. 8.2). We obtain an order of magnitude estimate for the hydrogen concentration based upon the changes in charge transport properties assuming adsorbed hydrogen induces resonant scattering. Comparing with previous experimental work on resonant scattering in graphene via fluorine doping [165] and lattice vacancies [161], the hydrogen concentration is estimated to be on the order of 0.1% for 8 s hydrogen exposure to sample A. This indicates samples are in the dilute limit of hydrogen coverage.

Atomic hydrogen is introduced to spin valve devices at 15 K at a chamber pressure of 1×10^{-6} torr. Following 2 s hydrogen exposure, the gate dependent ρ_G (red curve in Fig. 8.2b) is dramatically increased. An additional 6 s of exposure (8 s total) further increases ρ_G (blue curve of Fig. 8.2 b)) and decreases the mobility to 495 cm^2/Vs. Based on the change in the resistivity, we make an order of magnitude estimate for the hydrogen coverage of 0.1%. Accompanying the changes in charge transport are also changes in spin transport. Figures 8.2 e) and 8.2 f) display R_{NL} of sample A at $V_G - V_D$ = -15 V as a function of $B_{app,y}$ following 2 s and 8 s of exposure, respectively. The initial ΔR_{NL} of 8.8 Ω is reduced to 2.6 Ω after 2 s of hydrogen exposure and further reduced to 1.4 Ω after 8 s. Interestingly, the R_{NL} scans exhibit a dip centered at zero applied field. The dip in R_{NL} is prevalent for both up and down sweeps of $B_{app,y}$ at all measured gate voltages and has been reproduced on multiple samples following hydrogen exposure. The ratio of the dip magnitude to ΔR_{NL} is found to increase with increasing hydrogen exposure (comparing Fig. 8.2 e) and 8.2 f)), indicating the dip feature is dependent on the amount of adsorbed hydrogen.

8.4 Origin of the Dip in R_{NL}: Control Experiments

To understand the origin of the dip in R_{NL}, we examine the expression for non-local resistance generated by spin transport [31],

$$R_{NL}^{(P/AP)} = \pm 2R_G e^{\frac{-L}{\lambda}} \prod_{i=1}^{2} \left(\frac{P_J \frac{R_i}{R_G}}{1-P_J^2} + \frac{P_F \frac{R_F}{R_G}}{1-P_F^2} \right) \times \left[\prod_{i=1}^{2} \left(1 + \frac{2\frac{R_i}{R_G}}{1-P_J^2} + \frac{2\frac{R_F}{R_G}}{1-P_F^2} \right) - e^{\frac{-2L}{\lambda}} \right]^{-1} \tag{8.1}$$

where $R_G = \rho_G \lambda / w$ is the spin resistance of graphene, w is the graphene width, $R_F = \rho_F \lambda_F / A_J$ is the spin resistance of the cobalt, ρ_F is the cobalt resistivity, λ_F is the cobalt spin diffusion length, A_J is the junction area, P_F is the spin polarization of cobalt, R_1 and R_2 are the contact resistances of the spin injector and detector, respectively, and L is the distance from injector to detector. This equation shows that the spin density at the detector electrode depends on both charge and spin properties. First, we confirm that the SLG resistivity does not change with magnetic field, so the dip is not related to changes in charge transport (8.4.1). Also, we verify that the dip is not related to hydrogen-induced changes to the magnetic properties of the FM electrodes. Specifically, the effect of hydrogen exposure is reversible upon thermal cycling to room temperature and the anisotropic magnetoresistance of the Co electrodes are not affected by hydrogen exposure (8.4.3). Next, we perform minor loop analysis on sample B (Fig. 8.8 a)) by reversing the magnetic field sweep immediately after the first magnetization reversal. The inversion of the dip in the antiparallel state (red curve) proves that the dip is due to increased spin relaxation at low fields. Furthermore, we rule out hyperfine coupling to nuclear spins as the origin of this increased spin relaxation (8.4.2).

8.4.1 Excluding Field-Dependent Resistivity Effects

Equation 8.1 shows that changes in the resistivity of graphene could change the spin density at the detector electrode. Thus, magnetic field dependent changes to the graphene resistivity could in principle produce variations in R_{NL}. To investigate this possibility in hydrogen-doped graphene, gate dependent ρ_G measurements are performed on sample B at three distinct in-plane magnetic fields (Fig. 8.3). The three curves are indistinguishable, showing that the applied magnetic field has no effect on the measured ρ_G of hydrogen-doped samples. As presented in the Figs. 8.2 e), f) and 8.8 a), b), the R_{NL} signal increases by tens of mΩ as the magnetic field is increased away from $B_{app,y}$= 0 mT, corresponding to an increase of several percent. If this change is due to a magneto-resistance effect, the gate dependent resistivity curves measured at discrete in plane fields must also differ by hundreds of Ω to kΩ and will be clearly detected in the scan presented in Figure 8.3. As evident in Fig. 8.3, ρ_G vs. V$_G$ is unaffected by the applied magnetic field, confirming the source of the measured dip in R_{NL} does not stem from any magnetoresistance effects.

For completeness, we present a detailed scan of the four point (4pt.) resistance vs. $B_{app,y}$ performed on Sample C and compare it to the field dependence of non-local resistance. Fig. 8.4 a displays a large dip feature on a hydrogen doped graphene sample at T=15 K and associated minor loop to verify the signal is due to spin scattering. On this sample, the R_{NL} signal at $B_{app,y}$=0 mT is 24% of the high field value. In Fig. 8.4 b), we show the in-plane field dependence ($B_{app,y}$) of the 4pt resistance. The noise level of the data is 8-10 Ω while 4pt Resistance is 7535 Ω which is 0.1% of the signal and no dip feature is observed. 8.4 c) compares the relative change in resistances, $\Delta R_{NL}/R_{NL}$ (left axis) and 4pt $\Delta R/R$ (right axis), normalized to the high field values. The data shows there is no field dependence in the charge transport of hydrogen-doped graphene, therefore excluding variations in ρ_G as the source of the measured dip in R_{NL}.

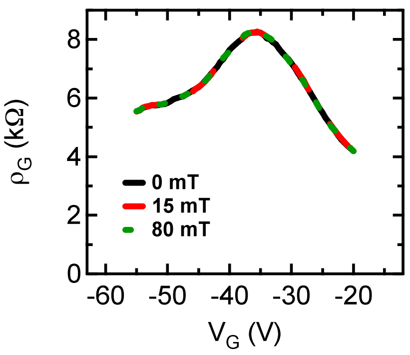

Figure 8.3: Investigating the Source of the Dip Measured in R_{NL}: Changes in Resistivity. Gate-dependent ρ_G of SLG after hydrogen exposure measured at several discrete in-plane applied magnetic fields. The applied field has no effect on the charge transport behavior of the graphene device.

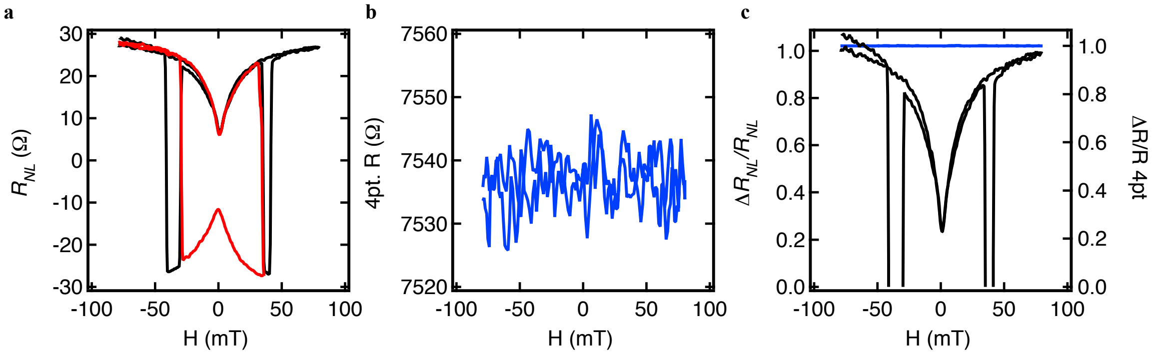

Figure 8.4: Comparison of Percent Change for R_{NL} and Resistivity. a) Non-local MR (R_{NL}) (black curve) and corresponding minor loop (red curve) for hydrogen doped graphene sample C at T = 15 K. b) Four point (4pt.) resistance of the same graphene channel as a function of the in-plane applied field ($B_{app,y}$)). Noise level is 8-10 Ω for 7.5 kΩ or 0.1% of the signal. c) Relative change of R_{NL} (black) and the 4pt Resistance (blue).

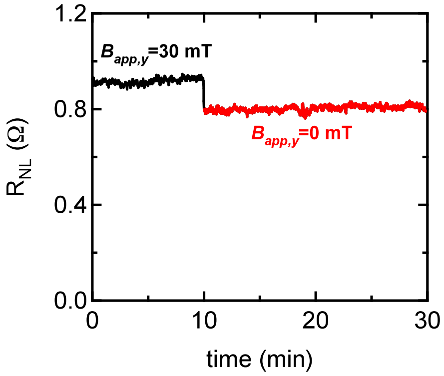

Figure 8.5: Test of Nuclear Spin Effects. The non-local spin transport signal is measured for 10 min while $B_{app,y}$=30 mT (black). This ensures any possible nuclear spins will reach steady state. The field is ramped to zero, and held constant for the following 20 min (red). The observed response excludes hyperfine coupling to nuclear spins as the origin of the dip in R_{NL}.

8.4.2 Excluding Nuclear Spin Effects

We investigate the possibility that the observed dip in the non-local resistance originates from hyperfine coupling between conduction electrons and nuclear spins. In graphene, this scenario is unlikely due to the small abundance of intrinsic nuclear spins in carbon (>98% of carbon is ^{12}C, which has no nuclear spin) and a lack of contact hyperfine coupling in the p_z-orbitals that make up the conduction and valence bands. Nevertheless, investigating the situation is necessary because the adsorption of hydrogen on graphene may alter the hyperfine coupling. Two effects that could in principle alter the non-local resistance include hyperfine coupling to dynamically polarized nuclear spins [368, 369] and organic magnetoresistance (OMAR) [370, 371].

The effect of OMAR has previously been observed in carbon C_{60} and functionalized carbon-based polymers [370, 371]. OMAR originates from hyperfine induced spin mixing between singlet and triplet states and manifests itself as a magnetic field dependent resistivity. However, as shown in Fig. 8.3, resistivity does not change as a function of applied in-plane magnetic field. This confirms OMAR is not responsible for the observed dip in R_{NL}.

The effect of dynamic nuclear polarization (DNP) was demonstrated clearly by Salis *et al.* [369] and Chan *et al.* [368] who investigated GaAs non-local spin valves at low temperatures. Specifically, Salis et al. observed a dip in R_{NL} at zero applied magnetic field, similar to the dip we observe in hydrogen-doped graphene. They attributed their dip to precessional spin dephasing caused by hyperfine coupling to dynamically polarized nuclear spins. To determine whether such nuclear spin effects are present in hydrogen-doped graphene we perform a series of tests.

Test 1: Nuclear spin relaxation times are typically long (∼minutes), and therefore, slow dynamics at this time scale are a characteristic of effects related to DNP. This is manifested in non-local spin transport data as a "lab time" dependence [369]. In our investigation of hydrogen-doped graphene, we do not observe a lab time dependence or a magnetic field ramp rate dependence.

Test 2: A characteristic feature of hyperfine coupling to the nuclear spin bath through DNP is the nuclear field's linear dependence on the applied field [369]. Specifically, at zero field the nuclear spin bath depolarizes slowly over time. The depolarization of the nuclear spin bath is evident in R_{NL} data as the gradual decrease and eventual disappearance (after a few minutes) of the dip when the applied field is set to zero (Figure 1 of Salis *et al.* [369]). We perform this test on hydrogen-doped graphene spin valves, as shown in Fig. 8.5. First, the magnetic field is held at -30 mT for 10 minutes to ensure any possible nuclear spin transients reach steady state. The R_{NL} is measured continuously during this period and exhibits a value of ∼0.92 Ω. Then the magnetic field is quickly reduced to zero, coinciding with the immediate drop of R_{NL} to ∼0.80 Ω. This drop occurs because $B_{app,y}$=0 mT is at the center of the dip in R_{NL}. The R_{NL} is measured over the following 20 minutes, for which the observed value remains unchanged at ∼0.80 Ω. This indicates that the magnitude of the dip is independent of lab time. If the dip were due to hyperfine coupling to dynamically polarized nuclear spins, then the magnitude of the dip would gradually decrease to zero (i.e. R_{NL} would increase back to ∼0.92 Ω). Because this behavior is not observed, the dip in R_{NL} cannot be due to DNP.

Test 3: For the case of DNP, applying a constant out-of-plane magnetic field during a non-local spin transport measurement (in-plane field scan) results in a characteristic feature of nuclear depolarization and repolarization as the in-plane field crosses zero (Figure 1 of Chan *et al.* [368]). We perform this measurement on hydrogen-doped graphene and observe no evidence of depolarization/repolarization features. Together, these three tests show that the dip in R_{NL} is not due to hyperfine coupling to dynamically polarized nuclear spins.

The above investigations of OMAR and DNP conclusively exclude the possibility of hyperfine coupling with nuclear spins as the source of the observed dip in the non-local spin transport.

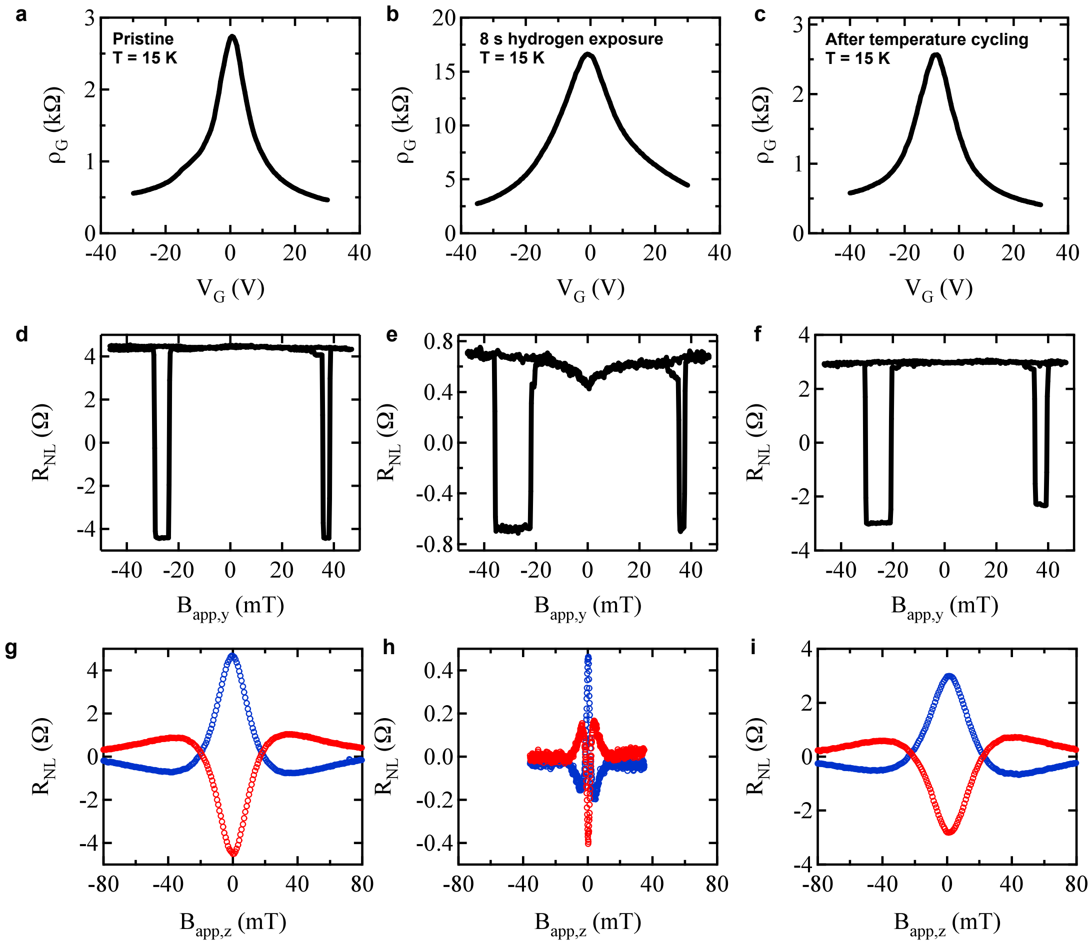

Figure 8.6: Reversibility of effects due to hydrogen doping of SLG. a) Gate dependent resistivity for pristine SLG at T=15 K. Data set corresponds to sample A. b) Gate dependent resistivity after 8 s hydrogen exposure at T=15 K. c) Gate dependent resistivity at T=15 K, measured after hydrogen exposure at 15 K followed by warming to room temperature and subsequent cooling to 15 K. d) R_{NL} for pristine SLG. e) R_{NL} after 8 s hydrogen exposure. f) R_{NL} after temperature cycling. g) Hanle spin precession data for pristine SLG. Blue (red) data is for parallel (antiparallel) magnetizations. h) Hanle spin precession data after 8 s hydrogen exposure. i) Hanle spin precession data after temperature cycling. All R_{NL} and spin precession data are measured at $V_G - V_D$=-15 V.

8.4.3 Excluding Changes in Magnetization of the Electrodes

Here we examine the possibility that the observed behavior in R_{NL} after hydrogen exposure is caused by spurious changes to the magnetic electrodes. It is known that hydrogen adsorption onto ferromagnetic materials can alter their magnetic properties [372, 373, 374, 375, 376]. In the present experiment, following the standard fabrication procedure for tunneling contacts to graphene as discussed in previous work [374], the magnetic electrodes are capped with 5 nm Al_2O_3. Also, we note that in the R_{NL} data presented in this work, the coercive fields of the electrodes remain unchanged after hydrogen exposure.

Further it is known that the bonding energy for hydrogen adsorption on transition metals is several eV ($\sim$2.6 eV for Co [376]), suggesting that H-Co chemisorption would be robust to temperature cycling. Here we observe that the behavior in R_{NL} and spin precession data after the introduction of atomic hydrogen at T=15 K is reversible upon temperature cycling (Fig. 8.6). At cryogenic temperatures, exposure of SLG graphene spin valves to hydrogen dramatically alters the charge and spin properties. The gate dependent resistivity increases, whereas the magnitude of R_{NL} decreases and exhibits a dip at low field. The observed dip is due to an increase in the spin scattering. Also, precession measurements exhibit a narrowing of the Hanle curve. Next, the sample is warmed to room temperature and subsequently re-cooled to T=15 K. The spin and charge transport properties are then re-measured. We have found that the charge transport properties of the gate dependent resistivity and mobility nearly recover to the pristine values. For instance, for sample A, the mobility is μ=6105 cm^2/Vs for pristine graphene. After 8 s hydrogen exposure the mobility decreases to μ=495 cm^2/Vs. After temperature cycling, the mobility recovers to μ=5450 cm^2/Vs. The recovery indicates the effect of hydrogen is removed through desorption, cluster formation, or a combination of the two. After temperature cycling, the spin signal R_{NL} contains no indication of a dip near low field and has increased to 5.95 Ω. Also, the spin precession data broadens and conventional Hanle analysis (equation 8.17) yields τ^{so}=353 ps and D=0.022 m^2/s. As mentioned above, changes in the Co electrodes should persist after temperature cycling and so cannot explain the observed behavior. Upon re-hydrogenation at cryogenic temperatures the key features (dip in R_{NL}, narrowed Hanle curve) return. Fig. 8.6 summarizes the changes in resistivity, R_{NL}, and spin precession upon temperature cycling.

To comprehensively verify that changes in magnetism of the Co electrodes is not the cause of the observed dip, we fabricate Co wires in the same fashion as for tunnel barrier contacts to graphene. Three 300 nm wide Co wires with equal length (L=200 μm) and 80 nm thick are oriented at 0 °, 45 °, and 90 ° with respect to an in-plane applied field. Figure 8.7 shows the magnetoresistance plotted as ΔR/R (%) vs. $B_{app,y}$ for the three different orientations before and after 20 s hydrogen exposure. We note that 20 s hydrogen exposure is significantly more than typically needed to generate observable effects in R_{NL}. As can be seen in Fig. 8.7, no effect is seen in the magnetoresistance of the Co wires upon hydrogen exposure. The switching fields and shape remain unchanged along with the anisotropy behavior. Therefore, we rule out effects of alterations in the Co wire magnetization as a possible source for the origin of the observed dip at zero field in R_{NL}.

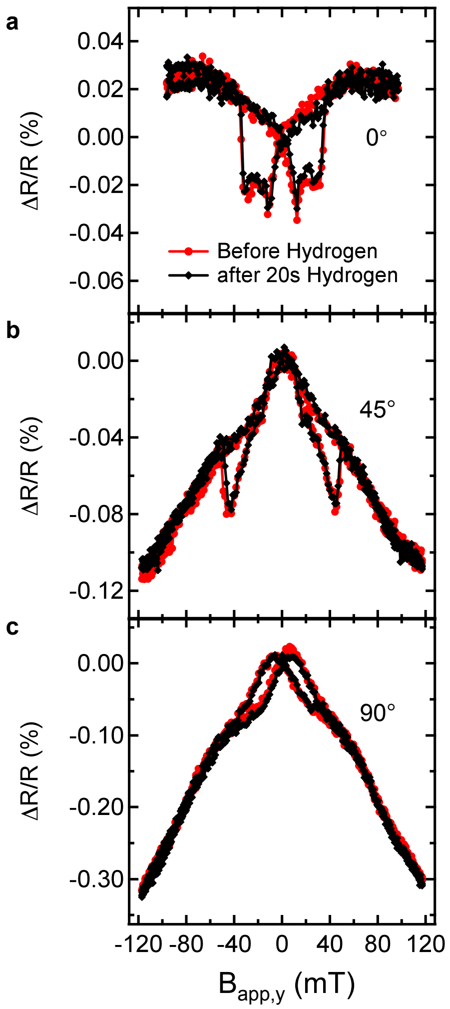

Figure 8.7: Magnetoresistance of Co Wires Before and After Hydrogen Exposure at T=10 K. a) ΔR/R (%) of a single Co wire measured before hydrogen exposure (red circles) for a wire oriented along $B_{app,y}$ (0 °). The wires were fabricated using standard e-beam lithography and angle evaporation in the same fashion as for producing tunnel barrier electrodes on SLG. The observed features are due to anisotropic magnetoresistance (AMR) and reflect the magnetization of the Co wire. No effect is observed after 20 s of hydrogen exposure (black diamonds). b) ΔR/R (%) of a Co wire oriented 45 ° with respect to $B_{app,y}$ before hydrogen exposure (red circles) and after 20 s exposure (black diamonds). c) ΔR/R (%) of a Co wire oriented 90 ° with respect to $B_{app,y}$ before hydrogen exposure (red circles) and after 20 s exposure (black diamonds). In all cases the wires are oriented in-plane.

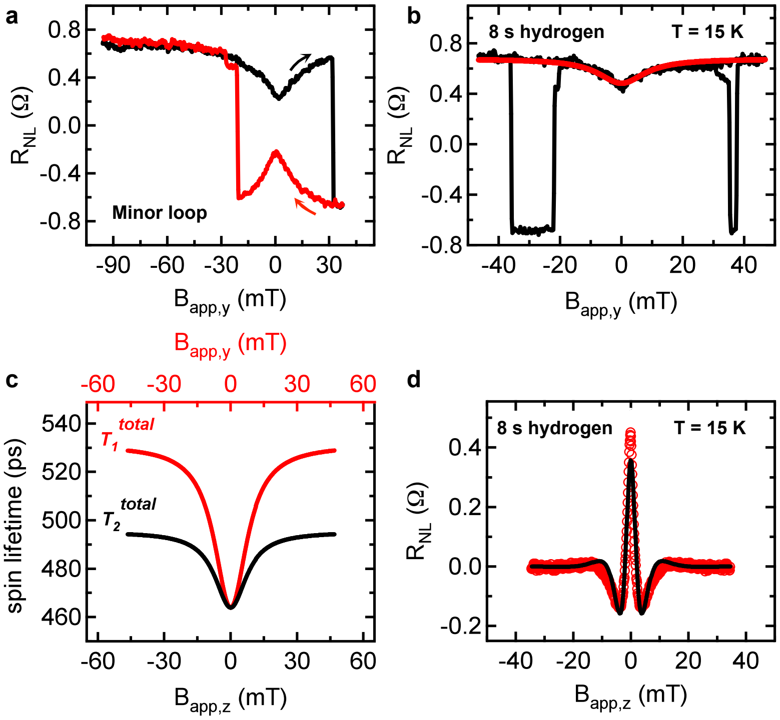

Figure 8.8: Minor Loop of Hydrogen-doped Graphene and Analysis of R_{NL}. a) A minor loop scan shows that the dip in R_{NL} for parallel alignment (black) becomes a peak for antiparallel alignment (red), indicating the feature is due to increased spin relaxation, as opposed to an artifact of the background level. b) Fitting the dip in R_{NL} based on the model of spin relaxation by paramagnetic moments (data in black, fit in red). c) Field dependence of longitudinal (red) and transverse (black) spin lifetimes. (d) Hanle precession data following 8 s hydrogen exposure (red) is fit using equation 9.1 (black curve).

8.5 Effective Exchange Field Model

8.5.1 Single Spin-Moment Model

As we discuss in the following, emergence of the dip following hydrogen adsorption identifies magnetic moment formation in graphene. The dip in R_{NL} is a characteristic feature of spin relaxation from exchange coupling with localized magnetic moments, and can be illustrated from a simple textbook example of two coupled spins in a magnetic field. The

Hamiltonian is given by $H = A_{ex}\vec{S}_e \cdot \vec{S}_M + g_e\mu_B\vec{S}_e \cdot \vec{B}_{app} + g_M\mu_B\vec{S}_M \cdot \vec{B}_{app}$, where $\vec{S}_e$ is the conduction electron spin, $\vec{S}_M$ is the spin of the magnetic moment, g_e and g_M are the respective g-factors, and A_{ex} is the exchange coupling strength [377, 378]. Due to the presence of the exchange coupling, the individual spins are not conserved; only the total spin $\vec{S}_{tot} = \vec{S}_e + \vec{S}_M$ is conserved. For the case where both $\vec{S}_e$ and $\vec{S}_M$ are spin-$\frac{1}{2}$, the quantum mechanical eigenstates in zero magnetic field are the well-known singlet ($S_{tot} = 0$) and triplet ($S_{tot} = 1$) spin states [379]. At higher magnetic fields the Zeeman terms dominate and the two spins decouple so that the magnitudes and z-components of $\vec{S}_e$ and $\vec{S}_M$ become good quantum numbers, similar to the Paschen-Back effect [379]. Thus, the dip in R_{NL} is qualitatively explained by the non-conservation of $\vec{S}_e$ at low fields due to the presence of exchange coupling with magnetic moments.

8.5.2 Interaction of an Electron Spin With Many Induced Moments

To quantitatively model the experiment, we consider electron spins $\vec{S}_e$ moving in an effective magnetic field of randomly positioned local magnetic moments $\vec{S}_M$ of filling density η_M. Each electron feels the average spin interaction

$$\begin{aligned} H_e &= \eta_M A_{ex}\vec{S}_e \cdot \langle\vec{S}_M\rangle + g_e\mu_B\vec{S}_e \cdot \vec{B}_{app} \\ &= g_e\mu_B\vec{S}_e \cdot (\overline{\vec{B}}_{ex} + \vec{B}_{app}) \end{aligned} \tag{8.2}$$

and

$$\overline{\vec{B}}_{ex} = \eta_M A_{ex} \langle \vec{S}_M \rangle / g_e \mu_B \tag{8.3}$$

where $\overline{\vec{B}}_{ex}$ is the effective exchange magnetic field, g_e is the electron g-factor, μ_B is the Bohr magneton, and A_{ex} is the strength of the exchange coupling between $\vec{S}_e$ and $\vec{S}_M$. The averaging $\langle ... \rangle$ is over the ensemble of magnetic moments. The effective exchange field $\overline{\vec{B}}_{ex}$ contributes to the Larmor frequency and enhances the electron g-factor.

As the spins diffuse through the lattice they experience varying magnetic moments which results in varying Larmor frequencies. In the local frame associated with the electrons this can be described by a time-dependent, randomly fluctuating magnetic field, $\vec{B}_{ex}(t) = \overline{\vec{B}}_{ex} + \Delta\overline{\vec{B}}_{ex}(t)$ with the rms value given by the time average

$$(\Delta B_{ex}^{rms})_{\alpha}^2 = \langle [\Delta B_{ex,\alpha}(t)]^2 \rangle_t \tag{8.4}$$

$$(\Delta B_{ex}^{rms})^2 = (\Delta B_{ex}^{rms})_x^2 + (\Delta B_{ex}^{rms})_y^2 + (\Delta B_{ex}^{rms})_z^2 \tag{8.5}$$

where α is an xyz component index. The time scale of the fluctuation is given by a correlation time τ_c defined by

$$\langle \Delta\vec{B}_{ex}(t) \cdot \Delta\vec{B}_{ex}(t-t') \rangle_t \propto \exp(-t'/\tau_c) \tag{8.6}$$

Spin relaxation resulting from a randomly fluctuating magnetic field has been solved in the review article by J. Fabian [20, Section IV.B.2] and is mathematically analogous to the D'yakanov-Perel model [92]. For the non-local spin signal geometry, the injected spin polarization and the applied magnetic field lie along the same axis (y-axis) and the spin relaxation rate is given by longitudinal spin relaxation equation IV.36 of [20] The equation is rewritten using $\omega_\alpha = g_e \mu_B \Delta B_{ex,\alpha}/\hbar$ and $\omega_0 = g_e \mu_B \overline{B}_{total}/\hbar = g_e \mu_B (B_{app,y} + \overline{B}_{ex,y}/\hbar)$ to yield,

$$\frac{1}{\tau_1^{ex}} = \frac{(\Delta B)^2}{\tau_c} \frac{1}{(B_{app,y} + \overline{B}_{ex,y})^2 + \left(\frac{\hbar}{g_e \mu_B \tau_c}\right)^2} \tag{8.7}$$

where $(\Delta B)^2 = (\Delta B_{ex})_z^2 + (\Delta B_{ex})_z^2$. In other words, precession around randomly fluctuating exchange fields along the x- and z-axes induce spin relaxation. Equation (8.7) also shows that the spin relaxation is suppressed by a large applied magnetic field. Intuitively, this occurs because the precession axis is defined by the large applied field (along y-axis) and fluctuating fields along the x- and z-axes have very little ability to tilt the precession axis. This peak in spin relaxation at low magnetic fields produces the observed dip in R_{NL}.

The presence of the average exchange field $\overline{B}_{ex,y}$ in equation (8.7) shows that the spin relaxation is maximized when the $B_{app,y} + \overline{B}_{ex,y} = 0$, or $B_{app,y} = -\overline{B}_{ex,y}$. Because $\overline{B}_{ex,y}$, is proportional to the magnetization, paramagnetic moments will generate a dip in R_{NL} centered at zero applied field while ferromagnetic ordering will generate a hysteretic dip centered away from zero applied field. The observed dip (Figs. 8.2 e), f) and 8.4) is centered at zero applied field and is not hysteretic, signifying the observed magnetic moments are paramagnetic.

For paramagnetic moments, $\overline{B}_{ex,y}$ takes the form of the Brillouin function (B_J) and is given by

$$\overline{B}_{ex,y} = \eta_M A_{ex} \langle S_{M,y} \rangle / g_e \mu_B = \eta_M A_{ex} J B_J(\xi) / g_e \mu_B \tag{8.8}$$

$$B_J(\xi) = \frac{2J+1}{2J} \coth\left(\frac{2J+1}{2J}\xi\right) - \frac{1}{2J} \coth\left(\frac{1}{2J}\xi\right) \tag{8.9}$$

where J is the total angular momentum quantum number of the magnetic moment, $\xi = \frac{J g_e \mu_B}{k_B \mathrm{T}} B_{app,y}$, k_B is Boltzmanns constant, and T is temperature. For our experiments at T=15 K, this reduces to $\xi = J g_e B_{app,y} / (22.32 \text{ Tesla})$. Thus, for the values of $B_{app,y}$ in our experiments $\xi \ll 1$ so that $B_J \approx (J+1)\xi/3J$ to yield

$$\overline{B}_{ex,y} = \frac{\eta_M A_{ex} J(J+1)}{3\mu_B} \left(\frac{B_{app,y}}{22.32 \text{ Tesla}}\right) \tag{8.10}$$

Thus, the total field can be written as

$$B_{total} = B_{app,y} + \overline{B}_{ex,y}$$

$$= B_{app,y} + \frac{\eta_M A_{ex} J(J+1)}{3\mu_B} \left(\frac{B_{app,y}}{22.32 \text{ Tesla}}\right)$$

$$= \left(1 + \frac{\eta_M A_{ex} J(J+1)}{3\mu_B (22.32 \text{ Tesla})}\right) B_{app,y} = \frac{g_e^*}{g_e} B_{app,y} \tag{8.11}$$

where the g_e^* is the enhanced g-factor due to the presence of the exchange field. Substituting this into equation (8.7) yields the expression for spin relaxation from paramagnetic moments in the linear regime,

$$\frac{1}{\tau_1^{ex}} = \frac{(\Delta B)^2}{\tau_c} \frac{1}{\left(\frac{g_e^*}{g_e} B_{app,y}\right)^2 + \left(\frac{\hbar}{g_e \mu_B \tau_c}\right)^2} = \frac{\frac{(\Delta B)^2}{\tau_c}\left(\frac{g_e}{g_e^*}\right)^2}{(B_{app,y})^2 + \left(\frac{\hbar}{g_e^* \mu_B \tau_c}\right)^2} \tag{8.12}$$

Thus, the longitudinal spin relaxation rate is a Lorentzian with a peak at zero applied field.

For the Hanle geometry, the injected spin polarization is along the y-axis and the applied magnetic field is along the z-axis. In this case the spin relaxation rate is given by transverse spin relaxation equation IV.38 in [20] The equation is rewritten using $\omega_\alpha = g_e \mu_B \Delta B_{ex,\alpha}/\hbar$ (for $\alpha = x, y, z$) and $\omega_0 = g_e \mu_B \overline{B}_{total}/\hbar$ = $g_e \mu_B (B_{app,z} + \overline{B}_{ex,z})/\hbar$ to yield

$$\frac{1}{\tau_2^{ex}} = \frac{1}{2}\left[\frac{(\Delta B)^2}{\tau_c \left(\frac{\hbar}{g_e \mu_B \tau_c}\right)^2}\right] + \frac{1}{2}\left[\frac{(\Delta B)^2}{\tau_c} \frac{1}{(B_{app,z} + \overline{B}_{ex,z})^2 + \left(\frac{\hbar}{g_e \mu_B \tau_c}\right)^2}\right] \tag{8.13}$$

where the fluctuating field is assumed to be isotropic: $(\Delta B_{ex})_x^2 = (\Delta B_{ex})_y^2 = (\Delta B_{ex})_z^2$. For paramagnetic moments, this becomes

$$\frac{1}{\tau_2^{ex}} = \frac{1}{2}\left[\frac{\frac{(\Delta B)^2}{\tau_c}\left(\frac{g_e}{g_e^*}\right)^2}{\left(\frac{\hbar}{g_e^* \mu_B \tau_c}\right)^2}\right] + \frac{1}{2}\left[\frac{\frac{(\Delta B)^2}{\tau_c}\left(\frac{g_e}{g_e^*}\right)^2}{(B_{app,z})^2 + \left(\frac{\hbar}{g_e^* \mu_B \tau_c}\right)^2}\right] \tag{8.14}$$

8.6 Application of the Exchange Field Model to Experimental R_{NL} and Hanle Data

In Brief

To quantitatively analyze the experimental data, we must consider that a conduction electron will interact with many localized magnetic moments. Thus, the terms in the Hamiltonian involving the conduction electron are given by $H_e = \eta_M A_{ex} \vec{S}_e \cdot \langle \vec{S}_M \rangle + g_e \mu_B \vec{S}_e \cdot \vec{B}_{app} = g_e \mu_B \vec{S}_e \cdot \left(\overline{\vec{B}}_{ex} + \vec{B}_{app} \right)$ where η_M is the filling density of magnetic moments. The averaging $\langle \cdots \rangle$ is over the ensemble of magnetic moments and the effective field generated by the exchange interaction is $\overline{\vec{B}}_{ex} = \frac{\eta_M A_{ex} \langle \vec{S}_M \rangle}{g_e \mu_B}$. As the spins diffuse through the lattice they experience varying magnetic moments which results in varying Larmor frequencies. In the local frame associated with the electrons this can be described by a time-dependent, randomly fluctuating magnetic field, $\vec{B}_{ex}(t) = \overline{\vec{B}}_{ex} + \Delta \vec{B}_{ex}(t)$. For the R_{NL} measurements, the longitudinal spin relaxation due to a fluctuating field is given by [20],

$$\frac{1}{\tau_1^{ex}} = \frac{(\Delta B)^2}{\tau_c} \frac{1}{\left(B_{app,y} + \overline{B}_{ex,y}\right)^2 + \left(\frac{\hbar}{g_e \mu_B \tau_c}\right)^2} \tag{8.15}$$

where ΔB is the rms fluctuation and τ_c is the correlation time.

The spin relaxation rate due to the exchange field is described by a Lorentzian curve which depends explicitly on the applied field, $B_{app,y}$, resulting in strong spin relaxation at low fields and suppressed spin relaxation at high fields. Due to the presence of $\overline{B}_{ex,y}$ in equation 8.15, ferromagnetic ordering will produce a dip in R_{NL} that is centered away from zero and is hysteretic, while paramagnetic ordering will produce a non-hysteretic dip centered at zero field. Thus, the magnetic moments measured in these experiments are paramagnetic. The total longitudinal spin lifetime, T_1^{total}, of conduction electrons is dependent on both the usual spin relaxation due to spin orbit coupling (τ_{so}) and longitudinal spin relaxation from the exchange field (τ_1^{ex}), such that $\left(T_1^{total}\right)^{-1} = \left(\tau_1^{ex}\right)^{-1} + \left(\tau^{so}\right)^{-1}$. We apply the above model to the non-local spin transport data presented in Fig. 8.2 f) (sample A) and fit using equation (8.1), $\lambda = \sqrt{DT_1^{total}}$, and equation (8.15). The resulting fit (red line in Fig. 8.8 b)) replicates the shape and magnitude of the dip measured in R_{NL} (black line in Fig. 8.8 b)). The field dependent T_1^{total} (Fig. 8.8 c)), exhibits a minimum of 464 ps at zero field and increases asymptotically towards τ_{so} = 531 ps for large $B_{app,y}$. The values obtained for ΔB and τ_c are 6.78 mT and 192 ps, respectively. The field-dependent spin relaxation following atomic hydrogen exposure, which emerges as a dip in R_{NL}, is a clear signature of paramagnetic moment formation.

Spin precession measurements provide further evidence for the presence of magnetic moments. Figure 8.8 d) shows spin precession data for sample A (8 s exposure, $V_G - V_D$ = -15 V) with FM electrodes in the parallel alignment state. The Hanle curve has considerably narrowed compared to the precession measurements obtained prior to hydrogen adsorption (Fig. 8.2 d)). The sharpening of the Hanle curve results from the presence of an exchange field. The injected spins precess around a total field $B_{tot} = B_{app,z} + \overline{B}_{ex,z}$ (along z-axis) that includes not only the applied field, but also the exchange field from the paramagnetic moments. At 15 K and $B_{app,z} < 100$ mT, the magnetization is proportional to the applied field so that $\overline{B}_{ex,z} = kB_{app,z}$, where k is a proportionality constant. Thus, the spins precess about B_{tot} with frequency $\omega = g_e \mu_B B_{tot}/\hbar = g_e(1+k)\mu_B B_{app,z}/\hbar = g_e^* \mu_B B_{app,z}/\hbar$. To properly account for the enhanced g-factor induced by the magnetic moments, the Hanle equation must be modified to

$$R_{NL} = S \int_0^\infty \frac{e^{-L^2/4Dt}}{\sqrt{4\pi Dt}} \cos\left(\frac{g_e^* \mu_B B_{app,z} t}{\hbar}\right) e^{-t/T_2^{total}} dt \tag{8.16}$$

where T_2^{total} is the transverse spin lifetime. As shown in Fig. 8.8 c), the T_2^{total} is related to, but different from T_1^{total}. Using the field dependent T_2^{total}, the precession data (red circles of Fig. 8.8 d)) is fit to equation 9.1 (black line) to yield a value of $g_e^* = 7.13$. Physically, $g_e^* > 2$ corresponds to an enhanced spin precession frequency resulting from the exchange field. The dramatic narrowing of the Hanle peak combined with the emergence of a dip in R_{NL} provides the most direct evidence to date for the formation of magnetic moments in graphene due to the adsorption of atomic hydrogen.

In Detail

The spin relaxation, diffusion coefficient, and interfacial spin polarization of the pristine sample are determined though analysis of R_{NL} and spin precession measurements. Fitting of spin precession data to the Hanle equation

$$R_{NL} = S \int_{0}^{\infty} \frac{e^{-L^2/4Dt}}{\sqrt{4\pi D t}} \cos\left(\frac{g_e \mu_B}{\hbar} B_{app,z} t \right) e^{-t/\tau^{so}} \, dt \tag{8.17}$$

provides values of spin lifetime (τ^{so}), diffusion coefficient (D), Hanle amplitude (S), and spin diffusion length ($\lambda = \sqrt{D\,\tau^{so}}$). For pristine graphene, the electron g-factor, g_e, is assumed to be 2. It should be noted that in the case of pristine graphene, the longitudinal spin relaxation (τ_1^{so}) and transverse spin relaxation (τ_2^{so}) due to spin orbit coupling are equivalent ($\tau_1^{so} = \tau_2^{so} = \tau^{so}$) [32]. Data measured on sample A (Fig. 8.2 d)), yields τ^{so}=479 ps, D=0.023 m^2/s and λ=3.3 μm for the channel length, L=5.25 μm. The corresponding R_{NL} data is fit with the non-local resistance equation (eq. 8.1) [31],

$$R_{NL}^{(P/AP)} = \pm 2 R_G e^{\frac{-L}{\lambda}} \prod_{i=1}^{2} \left(\frac{P_J \frac{R_i}{R_G}}{1 - P_J^2} + \frac{P_F \frac{R_F}{R_G}}{1 - P_F^2} \right) \times \left[\prod_{i=1}^{2} \left(1 + \frac{2 \frac{R_i}{R_G}}{1 - P_J^2} + \frac{2 \frac{R_F}{R_G}}{1 - P_F^2} \right) - e^{\frac{-2L}{\lambda}} \right]^{-1} \tag{8.18}$$

to obtain the interfacial spin polarization, P_J, for the graphene device.

In the above equation, R_G is the graphene spin resistance defined by, $R_G = \rho_G \lambda / w$, where ρ_G is the resistivity and w is the graphene width. $R_{1,2}$ denotes the contact resistances of injector and detector electrodes, P_F is the ferromagnetic electrode spin polarization (assumed to be 0.35 for cobalt), and $R_F = \rho_F \frac{\lambda_F}{l_j w}$ is the spin resistance of the ferromagnet, where $\rho_F = 5.8 \times 10^{-8}$ Ωm is the resistivity of cobalt, l_j=50 nm is the effective spin injector contact length of the ferromagnetic electrode and is determined by the fabrication procedures (see [25, 34] for details), and lastly, λ_F is the spin diffusion length of the ferromagnet, taken to be 38 nm in cobalt. The measured ΔR_{NL}=8.8 Ω for Sample A (Fig. 8.2 c)) corresponds to a P_J=0.20 for parameters λ=3.3 μm, ρ_G=898 Ω, w=2.3 μm, R_1=15.76 kΩ, and R_2=4.00 kΩ. The contact resistances are measured in a three terminal geometry [71] and are found to be unaffected by hydrogen exposure. The measured value of 20% interfacial spin polarization is comparable to previously reported values for efficient spin injection into SLG through tunneling contacts [71]. P_J is assumed to remain constant throughout hydrogen exposure, a reasonable assumption since the graphene at the site of spin injection is protected by the electrode, the hydrogen does not alter the cobalt (see section 8.4.3), and contact resistances remain unchanged.

As discussed above, exposure to atomic hydrogen results in the formation of magnetic moments, detected as a dip in R_{NL}. Additionally, a sharpened Hanle curve signifies enhanced precession of injected spins due to the presence of an exchange field caused by the moments. The exchange field is not accounted for in the standard Hanle equation (8.17), preventing direct determination of τ^{so} and D through Hanle fitting. Instead, the Einstein relation

$$D = \frac{\sigma}{e^2 \nu} \tag{8.19}$$

is employed to obtain D for hydrogen-doped samples, where ν denotes the density of states and e is the electron charge. Assuming ν is unchanged by exposure to hydrogen, which is reasonable in the dilute limit, the diffusion coefficient of hydrogen-doped samples D_{hyd} is determined from the pristine diffusion coefficient $D_{pristine}$ and the conductivities of hydrogen-doped (σ_{hyd}) and pristine ($\sigma_{pristine}$) graphene.

$$\frac{D_{hyd}}{D_{pristine}} = \left(\frac{\sigma_{hyd}}{e^2\nu}\right) \Big/ \left(\frac{\sigma_{pristine}}{e^2\nu}\right) = \frac{\sigma_{hyd}}{\sigma_{pristine}} \tag{8.20}$$

The change in conductivity from 1.113 mS to 0.143 mS following hydrogen exposure results in D_{hyd}=0.0029 m^2/s.

The longitudinal spin lifetime is evaluated by examining R_{NL} for the hydrogen-doped sample. As shown in equation (8.12) the spin relaxation rate arising from the presence of magnetic moments is described by a Lorentzian centered at $B_{app,y}$=0, and can be fit using the general form

$$\frac{1}{\tau_1^{ex}} = \Gamma \frac{\gamma^2}{(B_{app,y})^2 + \gamma^2} \tag{8.21}$$

The total longitudinal spin lifetime, T_1^{total}, depends on both τ_1^{ex} and τ^{so} through the relation

$$\frac{1}{T_1^{total}} = \frac{1}{\tau^{so}} + \frac{1}{\tau_1^{ex}} \tag{8.22}$$

subsequently affecting the spin diffusion length λ

$$\lambda = \sqrt{D\,T_1^{total}} = \sqrt{D\left(\frac{1}{\tau^{so}} + \frac{1}{\tau_1^{ex}}\right)^{-1}} = \sqrt{D\left(\frac{1}{\tau^{so}} + \Gamma\frac{\gamma^2}{(B_{app,y})^2 + \gamma^2}\right)^{-1}}. \tag{8.23}$$

The field dependent λ directly translates to a field dependence in the non-local resistance causing the experimentally observed dip in R_{NL} at zero applied field. Values for τ^{so}, Γ, and γ are determined by fitting the measured R_{NL} data to the non-local resistance equation (8.18), where λ is field dependent and defined by equation (8.23). The best fit to sample A is obtained by τ^{so}=531 ps, Γ=2.73$\times$10^8 s^{-1}, and γ=8.32 mT and is displayed as the red curve in Fig. 8.8 b), using, R_F=0.019 Ω, ρ_G=6.99 kΩ R_1=15.76 kΩ, R_2=4.00 kΩ, P_J=0.20, P_F=0.35, and L=5.25 μm. The field dependent values of T_1^{total} are displayed as the red curve in Fig. 8.8 c). Clearly, this model explains the data well and may also be relevant for dip features observed recently in metallic lateral spin valves [380].

Following the determination of τ^{so}, Γ, and γ, the spin precession data for the hydrogen-doped sample is analyzed in order to obtain values for g_e^*. The standard Hanle equation (8.17) must be modified to account for precession induced by both the applied field and the exchange field ($B_{ex,z}$) produced by magnetic moments as well as the field dependent transverse spin lifetime T_2^{total}, where $\frac{1}{T_2^{total}} = \frac{1}{\tau^{so}} + \frac{1}{\tau_2^{ex}}$. For the Hanle geometry, the spin relaxation rate from the magnetic moments is given by equation (8.14). Thus, in terms of the Lorentzian parameters Γ and γ, the total spin relaxation rate is,

$$\frac{1}{T_2^{total}} = \frac{1}{\tau^{so}} + \frac{\Gamma}{2}\left(1 + \frac{\gamma^2}{(B_{app,z})^2 + \gamma^2}\right) \tag{8.24}$$

For comparison, Fig. 8.8 c) displays the total longitudinal spin lifetime T_1^{total} (red curve) and total transverse spin lifetime T_2^{total} (black curve) for hydrogen-doped graphene sample A.

The modified Hanle equation is dependent on T_2^{total} and takes the form

$$R_{NL} = S \int_0^\infty \frac{e^{-L^2/4Dt}}{\sqrt{4\pi Dt}} e^{-t\left[\frac{1}{\tau^{so}} + \frac{\Gamma}{2}\left(1 + \frac{\gamma^2}{(B_{app,z})^2 + \gamma^2}\right)\right]} \times \cos\left(\frac{g_e \mu_B}{\hbar}(B_{app,z} + \overline{B}_{ex,z})t\right) dt \quad (8.25)$$

For paramagnetic moments, $\overline{B}_{ex,z}$ is described by the Brillouin function. Additionally, $\frac{JB_{app,z}}{(22.32\text{Tesla})} \ll 1$, so that $\overline{B}_{ex,z}$ can be represented by the low field approximation

$$\overline{B}_{ex,z} = \frac{\eta_M A_{ex} J(J+1)}{3\mu_B \,(22.32 \text{ Tesla})} B_{app,z} \quad (8.26)$$

resulting in,

$$R_{NL} = S \int_0^\infty \frac{e^{-L^2/4Dt}}{\sqrt{4\pi Dt}} e^{-t\left[\frac{1}{\tau^{so}} + \frac{\Gamma}{2}\left(1 + \frac{\gamma^2}{(B_{app,z})^2 + \gamma^2}\right)\right]} \quad (8.27)$$
$$\times \cos\left[\frac{g_e \mu_B}{\hbar}\left(B_{app,z} + \frac{\eta_M A_{ex} J(J+1)}{3\mu_B}\left(\frac{B_{app,z}}{22.32 \text{ Tesla}}\right)\right)t\right] dt$$

which simplifies to,

$$R_{NL} = S \int_0^\infty \frac{e^{-L^2/4Dt}}{\sqrt{4\pi Dt}} e^{-t\left[\frac{1}{\tau^{so}} + \frac{\Gamma}{2}\left(1 + \frac{\gamma^2}{(B_{app,z})^2 + \gamma^2}\right)\right]} \times \cos\left(\frac{g_e^* \mu_B}{\hbar} B_{app,z} t\right) dt \quad (8.28)$$

with,

$$g_e^* = g_e\left[1 + \frac{\eta_M A_{ex} J(J+1)}{3\mu_B (22.32 \text{ Tesla})}\right] \quad (8.29)$$

Fitting of precession data to equation (8.28) yields values for Hanle amplitude (S) and g_e^*. In the fit, fixed parameters are: Γ=2.73×10^8 s^{-1} and γ=8.32 mT, as determined by analysis of non-local resistance, D=0.0029 m^2/s from the Einstein relation, and L=5.25 μm. The best fit of Hanle data (presented in Fig. 8.8 d)) results in a g_e^* value of 7.13. We take a reasonable value for the exchange coupling of $A_{ex} \sim 1$ eV and the paramagnetic spin of $J = 1/2$ expected for the unpaired electrons due to hydrogen adatoms on graphene. Using the value g_e^*=7.13, we can independently estimate the fractional filling density of hydrogen induced magnetic moments to be $\eta_M \sim 1$ % using equation (8.29). This is in reasonable agreement with the order of magnitude estimate of 0.1% determined from the resistivity for 8 s hydrogen exposure to sample A.

The correlation time (τ_c) and the rms fluctuations in exchange field (ΔB) are determined by comparing equations (8.12) and (8.21) to give

$$\tau_c = \frac{\hbar}{g_e^* \mu_B} \frac{1}{\gamma} \tag{8.30}$$

$$(\Delta B)^2 = \gamma \left(\frac{g_e^*}{g_e} \right) \frac{\hbar \Gamma}{g_e \mu_B} . \tag{8.31}$$

Using g_e^*=7.13 from the Hanle fit and Γ=2.73×10^8 s^{-1} and γ=8.32 mT from the non-local fit, we obtain values of τ_c=192 ps and $(\Delta B)^2$=4.59×10^{-5} T^2 (or $\Delta B = \sqrt{(\Delta B_{ex,x})^2 + (\Delta B_{ex,z})^2}$ = 6.78 mT).

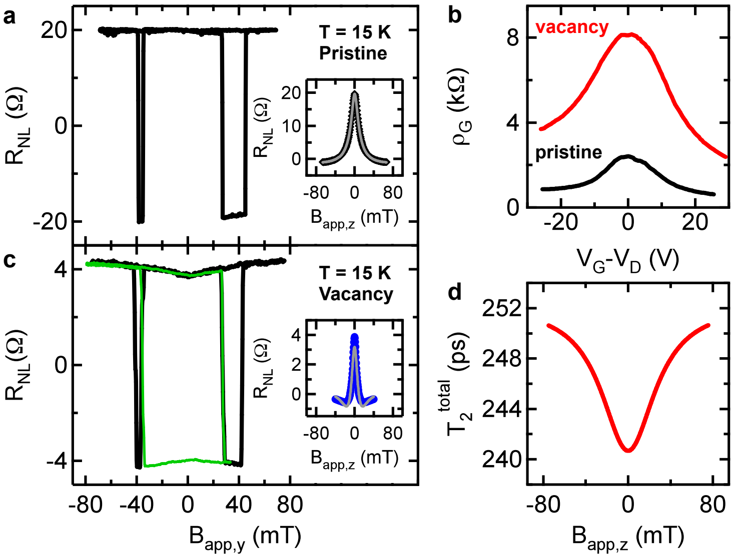

Figure 8.9: The Effect of Lattice Vacancies on Charge and Spin Transport in SLG at 15 K. a) Non-local spin transport data in pristine graphene with ΔR_{NL}=38.9 Ω. Hanle precession data (inset) yields values of τ^{so}= 859 ps and D=0.023 m^2/s. b) Gate dependent ρ_G for pristine graphene (black) and following lattice vacancy formation via Ar-sputtering (red). c) Non-local spin transport data in SLG containing vacancies. After Ar-sputtering, ΔR_{NL} is decreased to 8.2 Ω and exhibits a dip at zero applied field. The minor loop (green) confirms the observed dip is a spin dependent effect, caused by paramagnetic moment formation. The best fit to the Hanle precession data (inset) yields g_e^*=5.86. d) The field dependent T_2^{total} used to fit the Hanle data in c).

8.7 Magnetic Moments Generated by Lattice Vacancies

We investigate the effect of lattice vacancy defects in graphene. Several theoretical works suggest the similarity of magnetism due to vacancies and hydrogen-doping [315, 364], as both should create magnetic moments in graphene due to the removal/hybridization of p_z-orbitals. It is therefore reasonable to expect that similar effects will be observable in graphene spin transport following the introduction of lattice vacancies. To induce vacancies on pristine SLG spin valves, *in-situ* Ar-sputtering is performed at a sample temperature of 15 K. Argon partial pressures of 1×10^{-6} torr and energies between 100 eV and 500 eV combined with short sputtering times (several seconds) produce dilute lattice vacancies. Prior to exposure to Ar-sputtering, the SLG device exhibits a ΔR_{NL} of 38.9 Ω at $V_G - V_D$=20 V and displays no dip in non-local resistance at zero applied field (Fig. 8.9 a)). Fitting of the corresponding precession data (inset of Fig. 8.9 a)) results in values of τ^{so}=859 ps and D=0.023 m^2/s for the pristine SLG device. The black (red) curve presented in Fig. 8.9 b) displays ρ_G before (after) sputtering. After the introduction of vacancies, the resistivity is substantially increased and the mobility is reduced from 4945 cm^2/Vs to 949 cm^2/Vs. Ar-sputtering results in a large decrease in the magnitude of ΔR_{NL} as well as the emergence of a dip in R_{NL} at zero applied field (Fig. 8.9 c)). The minor loop, shown in green, indicates the observed dip is due to a decrease in the spin signal at low fields, signifying the formation of paramagnetic moments. The Hanle data (Fig. 8.9 c) inset) narrows following Ar-sputtering. The Hanle data combined with fitting the dip in R_{NL} yields values of g_e^*=5.86, ΔB=13.9 mT, τ_c=64.1 ps, and the field dependent T_2^{total} shown in Fig. 8.9 d). Given the very different chemical and structural properties of lattice vacancies compared to adsorbed hydrogen, the observation of similar features in the spin transport data provide strong evidence that the magnetic moments are created by the removal of p_z orbitals from the π-band, as predicted theoretically.

8.8 Properties of the Exchange Field

In this section, we discuss properties of the exchange field stemming from the formation of magnetic moments with the introduction of hydrogen. Specifically, we examine the relation between the exchange field and narrowing of the Hanle curve, and we investigate the gate dependence and accuracy of g_e^*.

8.8.1 Exchange Field and Narrowing of the Hanle Curve

Conventional Hanle analysis, as described at the beginning of section 8.6, consists of fitting spin precession data to the Hanle equation (8.17), yielding values for the spin lifetime (τ^{so}), the diffusion coefficient (D), and the amplitude (S). This relies on the assumption, g_e^*=2, and the absence of an exchange field. In conventional Hanle analysis, a narrowing of the Hanle curve is typically associated with an increase of the spin lifetime. Therefore, a valid question is whether the observed narrowing in the spin precession data after hydrogen doping is due to an enhanced spin lifetime instead of the emergence of an exchange field. Comprehensive analysis comprising the full data set (conductivity, non-local spin resistance (R_{NL}), and Hanle spin precession) provides compelling evidence that the narrowing of the Hanle curve is due primarily to an exchange field as opposed to enhanced spin lifetime. First, an increase in the spin lifetime cannot explain the observed dip in R_{NL}, while a fluctuating exchange field explains the dip and lineshape very well (see sections 8.5.2 and 8.6). Second, conventional Hanle analysis (g_e^*=2) of the hydrogen-doped sample A yields values for the diffusion coefficient that are inconsistent with the values obtained from the conductivity (differ by a factor of $\sim$6) and values for spin lifetime T_2^{total} that are inconsistent with the values obtained from the non-local spin resistance (differ by factor of 5-60). These inconsistencies can be resolved if an exchange field is present ($g_e^* > 2$). Key features of the full data

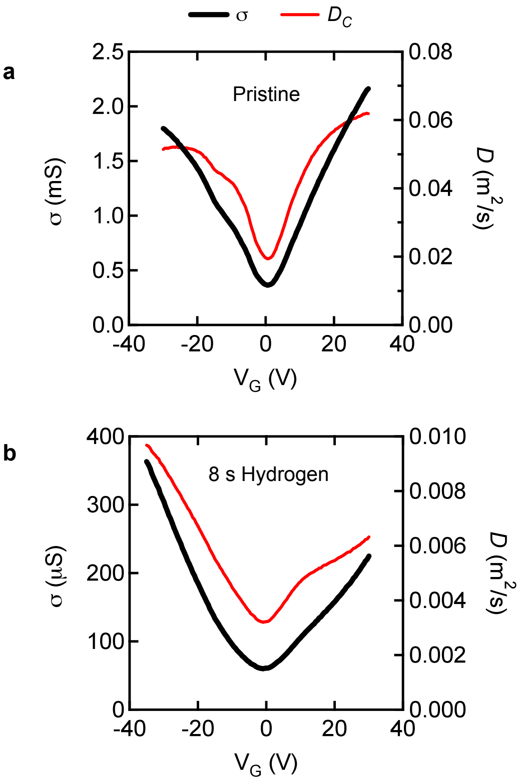

Figure 8.10: Conductivity and Calculated Diffusion Coefficient for Pristine and Hydrogen-doped SLG at 15 K. a) Gate dependent conductivity for pristine graphene (black curve) plotted on the left axis and the calculated diffusion coefficient, D_C (red curve), plotted on the right axis. b) Gate dependent conductivity for 8 s hydrogen exposure of SLG (black curve) plotted on the left axis and D_C (red curve) plotted on the right axis.

set emerge only after hydrogen doping and are best explained with a single effect, providing strong evidence for the presence of exchange fields.

In the following, we provide a detailed analysis of the discussion outlined above. First, we investigate the Hanle spin lifetime, $T_2^{total} = \tau^{so}$, without any consideration of an exchange field (i.e. g_e^*=2). Fig 8.11 a) and 8.11 c) show the gate dependence of Hanle lifetimes obtained from fitting spin precession data using Hanle equation (8.17) for pristine and 8 s hydrogen exposure to sample A, respectively. As can be seen in Fig. 8.11 c), when the Hanle fit parameters D and T_2 are allowed to vary, best-fit values yield long spin lifetimes. Values of

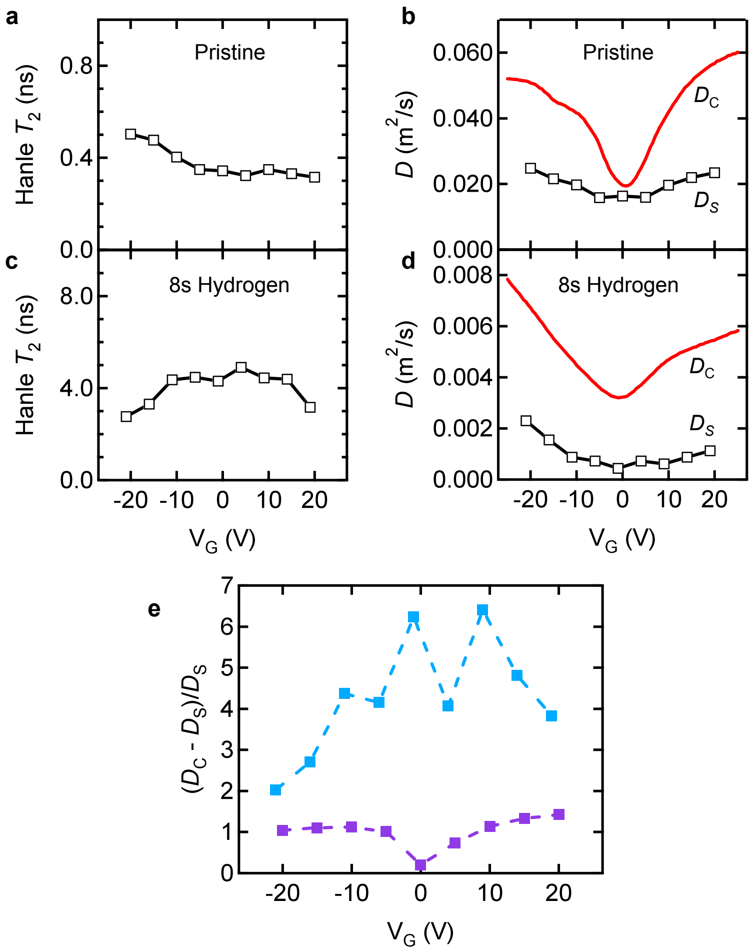

Figure 8.11: Conventional Hanle Fitting Assuming g_e^*=2 (No Exchange Field). a) Gate dependence of the Hanle spin lifetime for pristine SLG obtained by the Hanle equation. b) Gate dependence of the diffusion coefficients D_S (black open squares), obtained from the Hanle equation and the calculated diffusion coefficient, D_C (red curve), obtained by calculation from the conductivity and the broadened DOS for pristine SLG. c) Gate dependence of the Hanle spin lifetime for 8 s hydrogen exposure obtained by the conventional Hanle method. d) Gate dependence of the diffusion coefficients D_S (black open squares), obtained from the Hanle equation, and D_C (red curve) for 8 s hydrogen-doped SLG. e) Relative difference between D_S and D_C for pristine (purple solid squares) and 8 s hydrogen-doped (light blue solid squares) graphene.

D from the Hanle fit are denoted as D_S and are displayed (black open squares) in Fig. 8.11 b) and 8.11 d) for pristine and 8 s hydrogen-doped SLG.

Alternatively, one can use the gate-dependent conductivity to determine D via the Einstein relation (8.19),

$$D = \frac{\sigma}{e^2\nu}$$

where σ is the experimentally measured conductivity, e is the electron charge, and ν is the broadened density of states (DOS). This value of diffusion coefficient is denoted as D_C. Spatial fluctuations of the Fermi level due to inhomogeneities in the SiO_2/Si substrate lead to broadening of the DOS. For Gaussian broadening [70], the DOS is

$$\nu(E) = \frac{g_v g_s 2\pi}{h^2 v_F^2}\left[\frac{2b}{\sqrt{2\pi}}e^{-\frac{E^2}{2b^2}} + E\,\mathrm{erf}\left(\frac{E}{b\sqrt{2}}\right)\right] \tag{8.32}$$

where g_v is the valley g-factor, g_s is the electron spin g-factor, h is Plancks constant, v_F=1$\times$$10^6$ m/s is the Fermi velocity, and b is the Gaussian broadening parameter. In Figure 8.10 a) and 8.10 b) we show the conductivity (black curve) for both pristine and 8 s hydrogen exposure, respectively. These conductivity curves correspond with the resistance data of sample A as shown in Fig. 8.2 b). We find reasonable agreement for b=100 meV and use this throughout the remainder of this section for D_C. On the right axis of Figures 8.10 a) and 8.10 b) we plot the calculated diffusion coefficient (red curve) (b=100 meV) for pristine and 8 s hydrogen, respectively. We have found that a broadening parameter between 75 and 125 meV, which is reasonable for graphene on SiO_2/Si substrate [70, 154], gives generally similar results for the present discussion.

We next examine the difference between these two methods for determining the diffusion coefficient. Figure 8.11 b) and 8.11 d) plots D_S (black open squares) and D_C (red curve) for the pristine sample and the hydrogen-doped sample as a function of gate voltage, respectively. Interestingly, D_S is much smaller than D_C for the hydrogen-doped sample, particularly when compared to the pristine sample. To quantify this, we plot the relative difference $(D_C - D_S)/D_S$ in Figure 8.11 e) and find it to be as large as ~6 for the hydrogen-doped sample. On the other hand, the relative difference is less than ~1 for the pristine sample. Therefore, for the hydrogen-doped sample, the values of D determined from the conventional Hanle method (D_S) and the charge transport measurement (D_C) are inconsistent. There are two possible explanations for the appearance of a large discrepancy in D_S and D_C upon hydrogen doping. First, a system with an exchange field and increased effective g-factor yields a very low value of D_S when fit using conventional Hanle with g_e^*=2. Alternatively, it is well known that D_S and D_C can differ drastically if there are significant electron-electron interactions present in the system [381]. As discussed below, we find that the presence of an exchange field also resolves other inconsistencies generated by conventional Hanle fitting.

We now consider values of spin lifetime determined by the in-plane R_{NL} data and compare it to values determined from conventional Hanle fitting assuming no exchange field. Following the same procedure outlined in section 8.6 from equation (8.18) to (8.23), we obtain values of τ^{so} based on best fits to the high field data of R_{NL}. The method utilized in section 8.6 takes the diffusion coefficient, D_S, from the conventional Hanle fitting of the *pristine* sample, then scales it based on the Einstein relation according to equation (8.20). In this section, we denote this value as D_{SS}. The resulting spin lifetime values from R_{NL} are plotted in Figure 8.11 b) as a function of gate voltage and labeled "D_{SS}". Alternatively, best-fit values for the gate dependence of spin lifetime using the calculated diffusion coefficient, D_C, given by equations (8.19) and (8.32), are plotted in Figure 8.12 b) (blue open diamonds) and labeled "D_C". The light blue shaded region in the range of 300-600 picoseconds represents the values of spin lifetime consistent with the non-local resistance data and is labeled "R_{NL}". We compare this with the spin lifetimes determined by conventional Hanle fitting. The spin lifetime from the conventional Hanle fitting for 8 s hydrogen exposure displayed in Figure 8.11 c) is re-plotted in Figure 8.12 b) and labeled "D_S" (black open squares). Alternative values for spin lifetime are obtained by performing the Hanle fit with the diffusion coefficient as a fixed parameter given by D_C (and g_e^*=2). The resulting spin lifetime as a function of gate voltage is plotted in Figure 8.12 b) and labeled "D_C" (black open diamonds). The grey shaded region between 3 and 33 nanoseconds represents the values of spin lifetime consistent with the Hanle data assuming g_e^*=2 and is labeled "*Conventional Hanle*". Based on Figure 8.12 b), the spin lifetime determined by conventional Hanle analysis (with g_e^*=2) is inconsistent with the spin lifetimes determined by non-local resistance.

To summarize, with the introduction of atomic hydrogen (or lattice vacancies) to SLG, conventional Hanle fitting with the assumption of g_e^*=2 yields two inconsistencies: (i) values of D_S that are improbably low when compared to D_C and (ii) values of spin lifetime that are too large compared to values obtained from the non-local resistance. Notably, both of these inconsistencies can be alleviated if $g_e^* > 2$. This can be understood by considering the

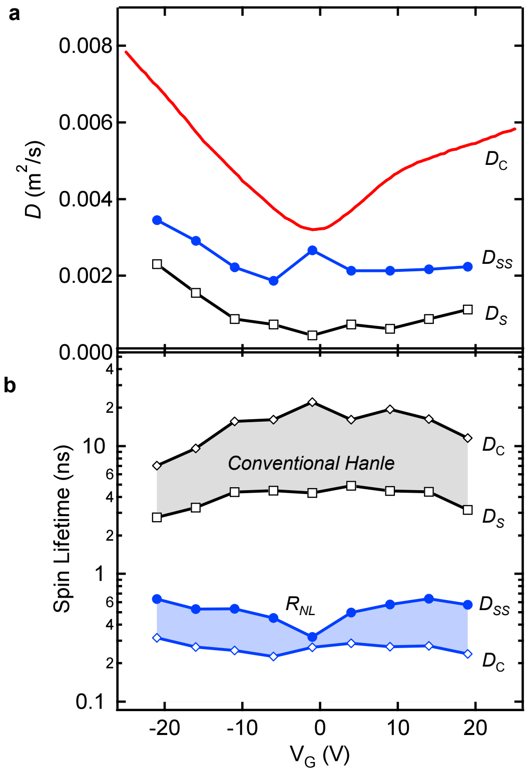

Figure 8.12: Comparison of the Spin Lifetimes. a) Gate dependence of the diffusion coefficients D_S (black open squares), D_C (red curve), and D_{SS} (blue solid circles) for 8 s hydrogen-doped graphene. b) Gate dependence of spin lifetimes for graphene after hydrogen exposure. Grey shaded region represents spin lifetimes by conventional Hanle fitting with D_C (black open diamonds) and D_S (black open squares) without taking the possibility of magnetic moments into account (g_e^*=2). A maximum T_2 of 33 ns is obtained at the charge neutrality point (V_G= -1 V) for D_C=0.0032 m^2/s. Blue shaded region represents spin lifetimes consistent with the in- plane R_{NL} data. Best fits solutions for τ^{so} using D_C (blue open diamonds) and D_{SS} (blue solid circles) according to the procedure outlined in section 8.6.

symmetries of the Hanle equation (8.33),

$$R_{NL} = S \int_0^\infty \frac{e^{-L^2/4D_S t}}{\sqrt{4\pi D_S t}} \cos\left(\frac{g_e^* \mu_B}{\hbar} B_{app,z} t\right) e^{-t/T_2} dt. \tag{8.33}$$

This equation is invariant under the transformation $g_e^* \to c\, g_e^*$, $T_2 \to T_2/c$, $D_S \to c\, D_S$, $S \to c\, S$, where c is a constant. For a given parameter set (g_e^*, T_2, D_S, S), the transformed

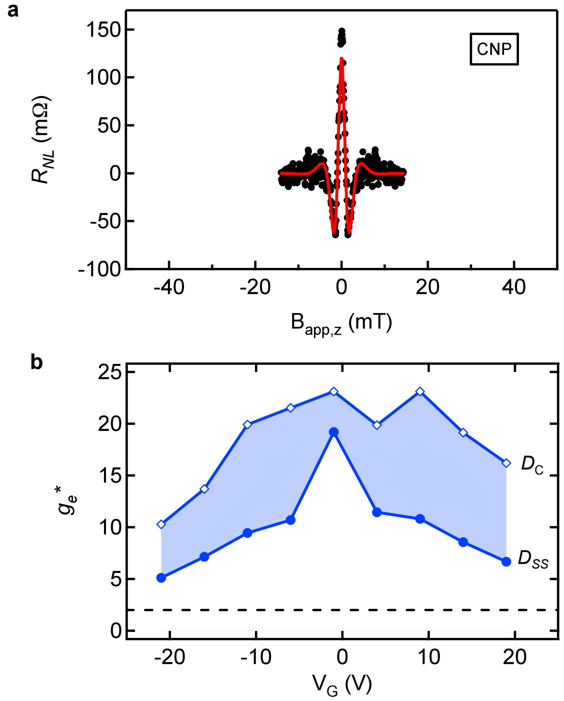

Figure 8.13: Gate Dependence of the Enhanced Precession due to the Exchange Field. a) Hanle precession data at the charge neutrality point (V_G=-1 V) for 8 s hydrogen exposure at T=15 K. A sharp increase in the observed precession due to the exchange field is seen at the charge neutrality point. Best fit to the Hanle equation (red curve) taking into account the Lorentzian shape of the spin lifetime and the scaled diffusion coefficient, D_{SS}, yields an effective g-factor, g_e^*=19.2. b) Gate dependence of g_e^* for both D_C (blue open diamonds) and D_{SS} (blue solid circles).

parameter set $(c\,g_e^*, T_2/c, c\,D_S, c\,S)$ will generate the same Hanle curve. Therefore, if we begin with a conventional Hanle fit that assumes g_e^*=2, a transformation that increases g_e^* (i.e. $c > 1$) has the effect of decreasing T_2 and increasing D_S. This simultaneously alleviates the discrepancies in spin lifetime and diffusion coefficient mentioned earlier, and therefore provides strong evidence for the presence of exchange fields.

The discussion above highlights several key points about the analysis of Hanle data. In the presence of an exchange field, g_e^* becomes a free parameter and the fitting parameters cannot be determined uniquely from the Hanle data alone. Therefore, it becomes necessary to analyze the in-plane R_{NL} data and the Hanle data together (as detailed in section 8.6) in order to determine key parameters such as spin lifetime and g_e^*. The nature of this data set, with *in-situ* doping, makes it straightforward to apply this analysis, but this may not be true in other studies utilizing Hanle spin precession. Consequently, it brings to light an important question about the use of Hanle fitting in general: how does one tell whether changes in the Hanle curve are due to changes in spin lifetime or g_e^*? Fortunately, the above analysis leads to a useful rule of thumb: If values of D_C and D_S are similar for conventional Hanle fitting, this provides support for the assumption that g_e^*=2. This is important for future Hanle studies of spin relaxation in order to recognize when changes in spin precession data are due to changes in spin lifetime. For systems with an exchange field, this analysis motivates the need for alternative experimental techniques that can independently measure g_e^* and T_2, such as electrically-detected electron spin resonance (ESR) and time resolved spectroscopies.

8.8.2 Gate Dependence and Accuracy of g_e^*

In this section we examine the gate dependence of the effective electron g-factor, g_e^*, due to the presence of an exchange field. Following the procedure of section 8.6, g_e^* values are obtained by Hanle fits to the spin precession data for 8 s hydrogen exposure to sample A using equation 8.28. Figure 8.13 a) shows the spin precession data (black closed circles) at the charge neutrality point (CNP) (V_G=-1 V) where the fastest precession is observed. The best fit solution (Fig. 8.13 a) red curve) to the spin precession data by equation 8.28 is determined through the free parameters S and g_e^*. Fig. 8.13 b) displays the gate dependence of g_e^* for both D_{SS} (blue solid circles) and D_C (blue open diamonds). The minimum value is g_e^*=5.1 obtained at V_G=-21 V and the maximum is g_e^*=19.2 at the CNP assuming D_{SS}. For D_C, the minimum g_e^* value is 10.3 for V_G= -21 V and the maximum is g_e^*=21.1 at the CNP. Uncertainty of the D value leads to uncertainty in g_e^*, again highlighting the need for techniques in graphene spintronics to directly measure g_e^* and T_2.

We can now examine the viability of performing Hanle analysis in the absence of consideration of R_{NL} data. This is important for experiments in which the contacts might induce additional spin relaxation or in apparatus for which the in-plane field cannot be applied. Next, we can fit the 8 s hydrogen doped spin precession data for Sample A using only D_C as a fixed parameter and allowing S, T_2, and g_e^* to vary. It must be noted that this analysis ignores the field dependence of T_2, but that does not significantly diminish the importance of this approach since the field dependence of T_2 is small when compared to the effect of g_e^* on the Hanle curve shape. In Fig. 8.14 b) we plot the resulting g_e^* (green curve) compared to the previous gate dependence determined using D_{SS} and D_C and Fig. 8.14 a) shows the resulting T_2 values in comparison with the other approaches from Fig. 8.12. It is a great result that the g_e^* values from this approach lie on top of the blue shaded region. This verifies that differences between D_C and D_S signify the presence of an effective g-factor. Interestingly, the best fit T_2 suggests a slight increase in τ_{so}, which may possibly be caused by DP mechanism which is expected to be important in SLG [88, 89, 84]. This analysis approach does not require any input from R_{NL} data and has recently been shown to be extremely useful in

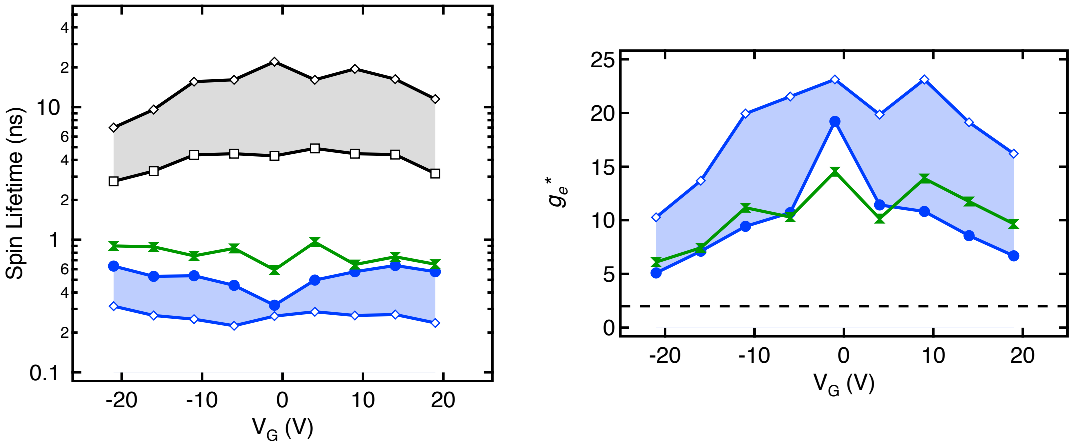

Figure 8.14: Analysis of Hanle Spin Precession Data Without Consideration of R_{NL} Data. a) Gate dependence of spin lifetimes of the Hanle only approach plotted in green. Grey shaded region represents spin lifetimes by conventional Hanle fitting with D_C (black open diamonds) and D_S (black open squares) without taking the possibility of magnetic moments into account (g_e^*=2). b) Gate dependence of the enhanced precession due to the exchange field. Analysis of the Hanle data only assuming a value of D_C is plotted in green compared to g_e^* for both D_C (blue open diamonds) and D_{SS} (blue solid circles). The green curve falls within the expected range indicating that this approach is valid.

understanding the behavior of doped and defected graphene [382, 383], as well as graphene on SiC [383, 78, 79].

8.9 Conclusion

In conclusion, clear signatures of magnetic moment formation are observed in both the non-local spin transport and Hanle precession data, which emerge only after exposure to atomic hydrogen or lattice vacancies. The technique used here, which investigates magnetic moment formation through the scattering of pure spin currents has significant advantages over other experimental attempts to investigate magnetism in graphene. The results and techniques presented here are important for future developments in magnetism and spintronics. In particular, the combination of improvements in tunneling contacts for spin injection into graphene and the ability to perform these measurements *in-situ* with molecular beam epitaxy have been crucial in the completion of this important work.

The investigation by spin-spin interactions is an entirely new way of looking at the induced moments and sheds light on the nature of these magnetic moments and is not expected according to the current theoretical understanding of magnetic moment formation in graphene. For flat graphene, symmetry forbids hybridization of the σ and π bands thus making exchange coupling between conduction spins and the localized moment not possible. These results clearly demonstrate such exchange coupling and has motivated re-examination of the nature of the induced moments as discussed in a recent Castro Neto paper [384].

Further, the observed behavior in the Hanle data can only be explained by the presence of an exchange field. Numerous theorists have examined the possibility of exchange fields as well as their impact on gate tunable magnetism, quantized anomalous Hall effect, the spin rotator, and spin filter as discussed in Chapters 3 and 7. Yet, there have been no experimental signatures of exchange coupling or fields in graphene for any type of system (impurity, proximity, etc...) until now. Our results demonstrate the first observation of exchange fields in graphene. Further, this is the first system to incorporate a spin transistor device with magnetic graphene and demonstrate control over the exchange coupling and exchange field with a back gate. Not only does this work demonstrate new and unexpected spin physics, but it also opens the door to a new area of research that has appeal for both fundamental and applied physicists and engineers. Very recently, Nair et al., [331] (on the arxiv) have reported a doping effect on the magnetic moments introduced into graphene ‘laminates’ which seems to qualitatively agree with the results presented here.

Chapter 9

Effect of *in-situ* Deposition of Mg Adatoms on Spin Relaxation in Graphene

9.1 Introduction

Graphene's gate tunable transport, tabletop relativistic physics, chemical attributes, and mechanical properties have interested researchers in a wide variety of fields [44, 45, 43, 385]. In particular, graphene is a candidate material for spintronics due to its weak hyperfine coupling and low intrinsic spin-orbit (SO) coupling strength (Δ_{SO}) [61, 62, 63, 32], which should theoretically lead to long spin lifetimes. Beyond scientific interest, recent progress in large area production by chemical vapor deposition [48, 49] combined with significant advances in efficient spin injection by improved tunneling contacts [71, 77] has greatly improved the potential for advanced information processing utilizing spin-based logic [386]. In particular, the introduction of efficient tunneling contacts has increased the observed spin lifetime by an order of magnitude (to $\sim$1 nanosecond in exfoliated graphene) by lengthening the escape time due to the back-flow of electrons into the ferromagnetic leads [71, 75, 72]. While graphene remains a highly promising candidate for carbon based spintronics, the observed spin lifetimes are still well below the theoretical expectations and the nature of spin relaxation remains an open question.

In graphene, two possible spin relaxation mechanisms are discussed in the literature: the Elliot-Yafet (EY) mechanism, for which the spin relaxation time (τ_s) is proportional to the momentum scattering time (τ_p), and the D'yakonov-Perel (DP) mechanism, for which $\tau_s \propto \tau_p^{-1}$ [75, 72, 83, 84, 85, 86, 87, 88, 70, 69, 89]. Complicating the situation are the many possible sources of spin relaxation in experiments on SiO_2 substrate including charged impurity (CI) scatterers [83, 84], Rashba SO coupling due to adatoms [85, 93, 86], ripples [87, 88], and edge effects [84, 69]. Early experiments on spin transport in exfoliated graphene were able to take advantage of the tunable carrier concentration (n) and observe a linear relationship between τ_s and τ_p, thus suggesting EY [70, 72]. However, recent theoretical studies have shown that DP is expected to dominate over EY [88, 89] and that Elliot's approach applied to graphene predicts $\tau_s = (\epsilon_F)^2\tau_p/(\Delta_{SO})^2$ [84], for which both Fermi energy ϵ_F and τ_p depend on carrier concentration, thus highlighting the need for experiments that can tune τ_p at fixed carrier concentration, n.

In this work we systematically introduce CI scatterers on non-local single-layer graphene (SLG) spin valves with high quality tunneling contacts. The experiment takes place in an ultra-high vacuum (UHV) deposition chamber with *in-situ* measurement capability at cryogenic temperatures. All measurements and doping are performed in the same chamber at T=12 K and the sample is never exposed to air. We choose Mg adsorbates as the CI scatterer since elements with low atomic weight should introduce minimal SO coupling. This substantially improves on earlier doping studies that utilized heavy atoms (Au) and ohmic contacts for shorter spin lifetimes ($\tau_s \sim 100$ ps) [171], which are dominated by contact induced spin relaxation [71]. We find that doping with Mg causes large shifts in the charge neutrality point (CNP), indicating significant charge transfer to the graphene layer, accompanied by increased momentum scattering. Spin transport measurements, however, indicate minimal effect on the spin relaxation despite pronounced changes in charge transport. These results indicate that CI scattering is not an important source of spin relaxation in SLG in the current regime of spin lifetimes of $\sim$1 ns.

9.2 Results and Discussion

Graphene flakes are obtained by mechanical exfoliation of HOPG (SPI, ZYA) onto 300 nm SiO_2/Si. SLG flakes are identified under an optical microscope and confirmed by Raman spectroscopy. The graphene flakes are electrically contacted using standard bilayer (PMMA/MMA) e-beam lithography and lift-off procedures. First, outer Au/Ti electrodes (60 nm/8 nm) are defined and deposited by e-beam evaporation to serve as spin insensitive reference contacts. The sample is then annealed for 3 hours in UHV at 150°C immediately

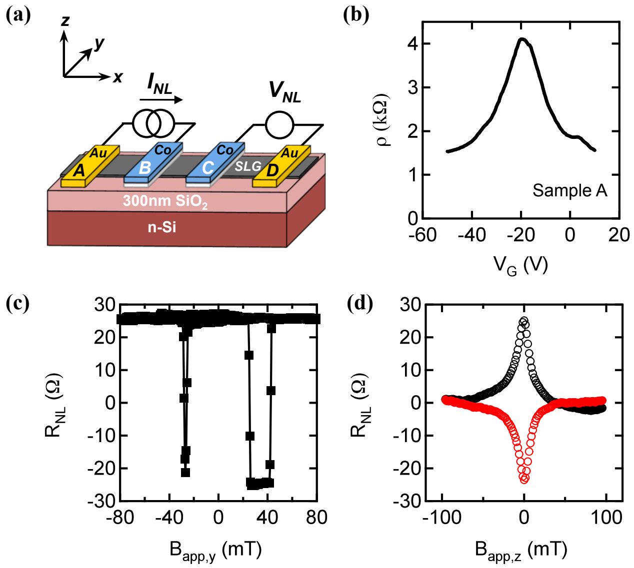

Figure 9.1: Spin Transport in Pristine Graphene. a) Device schematic of the non-local spin valve geometry with inner Co electrodes (blue) and outer Au electrodes (yellow). b) Gate dependent resistivity for sample A at $T = 12$ K. c) R_{NL} for pristine SLG at $V_G = 0$ V. d) Hanle spin precession data in parallel (black) and anti-parallel (red/grey) configuration between electrodes B and C for pristine SLG at $V_G = 0$ V. A constant spin-independent background has been subtracted.

prior to the second lithography step, which defines the inner ferromagnetic electrodes. Angle evaporation is utilized to deposit sub-monolayer TiO$_2$, which serves as a diffusion barrier for the 0.9 nm MgO tunnel barrier, and 80 nm Co. These tunneling contacts are deposited in a molecular beam epitaxy (MBE) chamber with base pressure of 1×10^{-10} torr. The electrodes are then capped with 5 nm Al$_2$O$_3$. A detailed description for the fabrication of tunneling contacts is described elsewhere [72].

Charge and spin transport measurements at T=12 K are performed on non-local devices as shown in Fig. 9.1 a). The gate dependent resistivity of pristine SLG (sample A) is shown in Fig. 9.1 b) with maximum resistivity at the charge neutrality point, $V_{CNP} = -20$ V. The mobility is calculated by taking the slope of the conductivity ($\mu = \Delta\sigma/e\Delta n$) where the carrier concentration, n (positive for holes), is determined using the relation $n = -\alpha(V_G - V_{CNP})$ and $\alpha = 7.2 \times 10^{10}$ V^{-1}cm^{-2} for 300 nm SiO$_2$ gate dielectric. The resulting electron and hole mobilities are $\mu_e = 1774$ cm^2/Vs and $\mu_h = 1508$ cm^2/Vs, respectively. For spin transport measurements, an AC current, $I_{NL} = 1$ μA (11 Hz), is applied to inject spin-polarized carriers into SLG at electrode B. This spin polarization diffuses through the graphene channel along the x-axis to electrode C. A non-local voltage, V_{NL}, is detected using standard lock-in techniques between electrodes C and D due to the accumulation of spins beneath electrode C. The detected voltage, V_{NL}, is proportional to the spin-dependent chemical potential difference between electrodes C and D [32]. The non-local resistance, $R_{NL} = V_{NL}/I_{NL}$, depends on the relative orientation of the two inner ferromagnetic electrodes and is positive (negative) for parallel (antiparallel) alignment. An external magnetic field, $B_{app,y}$, is applied along the electrode easy axis (y-axis) and is used to control the relative alignment of the magnetic electrodes. A typical sweep of $B_{app,y}$ for sample A at $V_G = 0$ V ($n = -1.44 \times 10^{12}$ cm^{-2}) is shown in Figure 9.1 c), for which the spin signal $\Delta R_{NL} = R^P_{NL} - R^{AP}_{NL}$ is 50.5 Ω. The dimensions of the graphene spin channel for sample A are defined by the channel length $L = 2.2$ μm and width $w = 2.4$ μm. The spin lifetime can be determined from Hanle spin precession measurements in which a magnetic field, $B_{app,z}$, is applied out of plane allowing the injected spins to precess around $B_{app,z}$. At large fields, the ensemble spin population dephases as $B_{app,z}$ is increased due to a distribution of arrival times at electrode C. In the tunneling limit, the ensemble spin precession can be fit using the Hanle equation [32, 72],

$$R_{NL} \propto \int_0^\infty \frac{e^{-L^2/4Dt}}{\sqrt{4\pi Dt}} \cos\left(\frac{g\mu_B B_{app,z} t}{\hbar}\right) e^{-t/\tau_s} dt \tag{9.1}$$

where D is the diffusion coefficient, g is the electron g-factor, μ_B is the Bohr magneton, and $\hbar$ is the reduced Planck's constant. Figure 9.1 d) shows characteristic Hanle curves for parallel and antiparallel alignment for $n = -1.44 \times 10^{12}$ cm^{-2}, where best fits to the Hanle equation yield the diffusion coefficient $D = 0.058$ m^2/s, spin lifetime $\tau_s = 1.10$ ns, and spin diffusion length $\lambda_s = 8.0$ μm.

Next, Mg adsorbates are deposited *in-situ* in the UHV MBE chamber with base pressure 3×10^{-10} torr while the sample is maintained at T=12 K. Elemental Mg (99.99%) is evaporated from an effusion cell at a rate of 0.055 Å/min calibrated by a quartz crystal monitor and corresponds to a doping rate of 0.02% of a monolayer (ML) per second, where 1 ML is defined as 1.908×10^{15} atoms/cm^2. After 1 s Mg deposition, the charge and spin transport are re-measured. Figure 9.2 summarizes the effect on the charge transport on sample A following Mg doping. Figure 9.2 a) shows conductivity σ vs. V_G for Mg doping of sample A up to 7 s deposition time. After 7 s of Mg doping, V_{CNP} has shifted to $V_G = -70$ V. This indicates that Mg donates electrons to the graphene, consistent with other work on transition metals [148, 51, 144]. Figure 9.2 b) displays V_{CNP} for each doping time and demonstrates a linear relation between charge transfer and Mg coverage at a rate of -1438 V/ML. Also, Mg doping introduces CI scattering which decreases the conductivity and the mobility. Figure

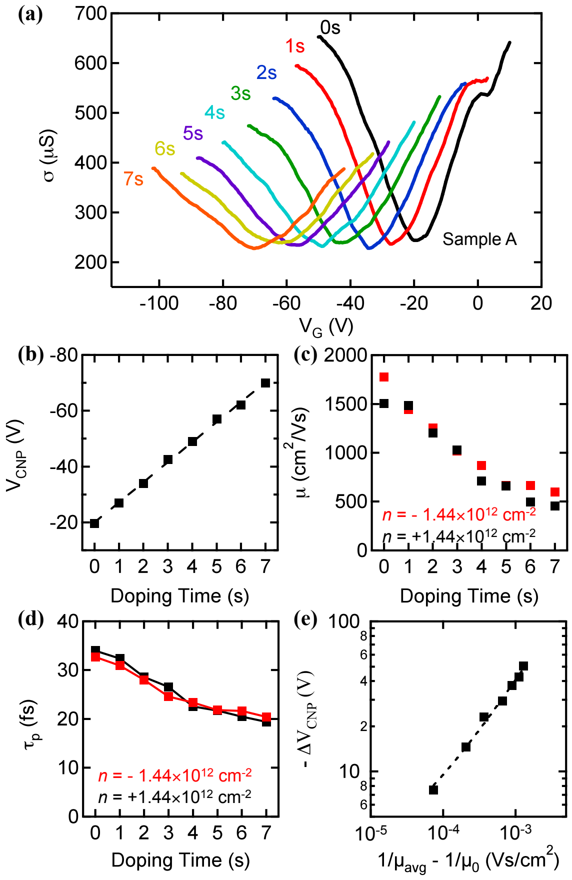

Figure 9.2: Effect on Charge Transport by Mg Doping. a) Gate dependent conductivity as the SLG (sample A) is systematically doped up to 7 s with Mg adsorbates at T=12 K. b) Charge neutrality point (CNP) plotted against the Mg doping time. c) Electron (red/grey) and hole (black) mobility as a function of Mg coverage. d) Calculated momentum scattering time for electrons (red/grey) and holes (black) as a function of Mg coverage. e) Shift in the charge neutrality point, $-\Delta V_{CNP}$, plotted against the change in inverse mobility. The dashed line is a power law fit (best fit exponent $b = 0.72$).

9.2 c) displays the effect of systematic Mg doping on the electron and hole mobilities. For undoped graphene, the mobility is $\mu_e = 1774$ cm^2/Vs and and $\mu_h = 1508$ cm^2/Vs, and decreases to $\mu_e = 599$ cm^2/Vs and $\mu_h = 453$cm^2/Vs after 7 s deposition time. The momentum scattering time can be determined using Boltzmann transport theory [50],

$$\tau_p = \frac{h\sigma}{e^2 v_F \sqrt{n\pi g_s g_v}} \tag{9.2}$$

where h is Planck's constant, e is the electron charge, $v_F \sim 1 \times 10^6$ m/s is the Fermi velocity, and $g_e = 2$ and $g_v = 2$ are the spin and valley degeneracies. Fig. 9.2 d) shows τ_p vs. Mg doping for electrons and holes at $n = \pm 1.44 \times 10^{12}$ cm^{-2}. With increasing Mg coverage, the momentum scattering time decreases due to increased CI scattering. Lastly, we investigate the nature of Mg morphology on the graphene surface. Figure 9.2 e) shows the shift in charge neutrality point plotted against $1/\mu_{avg} - 1/\mu_0$, where μ_{avg} is the average of the electron and hole mobilities and μ_0 is the average electron and hole mobility for pristine graphene. The dashed line is a power law fit of $-\Delta V_{CNP} \propto (1/\mu_{avg} - 1/\mu_0)^b$, for which values of $1.2 < b < 1.3$ indicates a $1/r$ scattering potential for point-like scatterers [387, 159, 51, 144]. The best fit value of $b = 0.72$ indicates that the Mg adatoms do not transfer charge as well as they add momentum scattering when compared to point-like scatterers. This suggests the possibility of clustering even at cryogenic temperatures [51, 144]. This does not introduce a theoretical difficulty because the relationship $\tau_s = (\epsilon_F)^2 \tau_p / (\Delta_{SO})^2$ for EY scattering in SLG has been shown to hold for a wide variety of scattering sources including weak scatterers, strong scatterers (i.e. vacancies), CI scatterers, and clusters [84]. Lastly, we note that the gate dependent resistance curves exhibited no measurable change as a function of time in between Mg depositions.

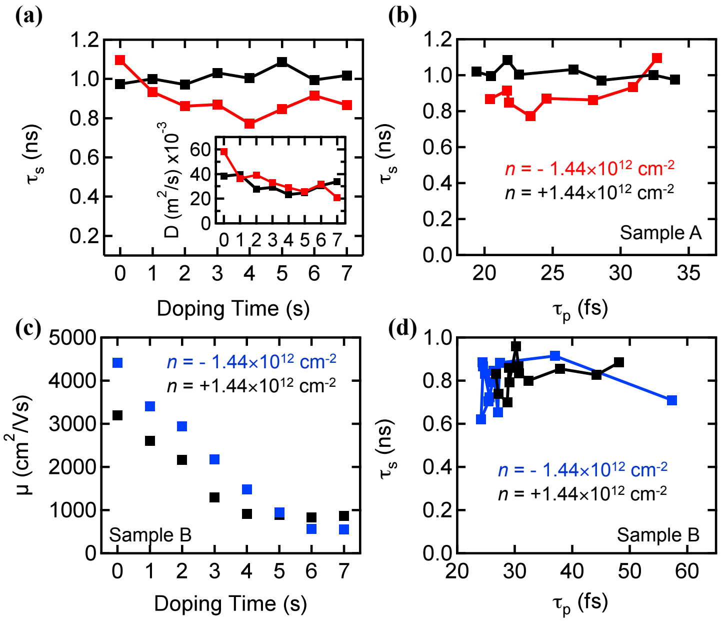

Figure 9.3: Effect on Spin Transport by Mg Adatoms. a) Hanle spin lifetime for sample A plotted against Mg coverage. Inset is the diffusion coefficient obtained from the Hanle fit as a function of Mg coverage at T=12 K. b) Hanle spin lifetime for sample A plotted against the calculated momentum scattering times for each doping. c) Electron (blue/grey) and hole (black) mobility as a function of Mg coverage for sample B at T=12 K. d) Hanle spin lifetime for sample B plotted against the calculated momentum scattering times.

We now turn to the effect on spin relaxation in SLG by Mg doping. After each Mg deposition at 1 s intervals, Hanle spin precession measurements were performed for $n = \pm 1.44 \times 10^{12}$ cm^{-2}. The resulting fits to the Hanle curves yield values for τ_s and D which are plotted against Mg doping time in Figure 9.3 a) and 9.3 a) inset, respectively. The diffusion coefficient decreases with increasing Mg coverage starting at 0.058 m^2/s (0.038 m^2/s) for pristine graphene and decreases to 0.021 m^2/s (0.033 m^2/s) for 7 s doping time for electrons (holes). This is in agreement with the observed charge transport behavior for which momentum scattering increases with Mg doping. Interestingly, the spin lifetimes (Fig. 9.3 a)) shows minimal variation, without a significant trend for electrons and holes. In Figure

9.3 b) we plot the Hanle spin lifetime for sample A against the momentum scattering time calculated from the conductivity using Eq. 9.2 from Boltzmann transport theory for sample A. With increasing Mg doping, τ_p decreases from $\sim$ 35 fs to $\sim$ 20 fs, but the spin relaxation time is constant for holes (black squares) while decreasing only slightly for electrons (red/grey squares). This experiment was repeated on several samples and in general τ_s does not display any substantial variations as a function of τ_p. For instance, results for a sample with higher initial mobility (sample B) are summarized in Fig. 9.3 c) and 9.3 d). Figure 9.3 c) displays the change in mobility for electrons and holes under Mg doping. For sample B, the mobility decreases from 4415 cm^2/Vs (3200 cm^2/Vs) for the pristine spin valve to 598 cm^2/Vs (1290 cm^2/Vs) after 7 s Mg doping for electrons (holes). In Fig. 9.3 d), we show τ_s displayed against the momentum scattering times for sample B at $n = \pm 1.44 \times 10^{12}$ cm^{-2}. Here, τ_s is near 800 ps and stays relatively unchanged as τ_P decreases from $\sim$ 60 fs to $\sim$ 24 fs.

As Fig. 9.3 b) and 9.3 d) show, τ_s does not vary substantially as τ_p is varied by CI scattering. This is in agreement with and goes beyond recent reports on CI scattering by organic-ligand bound nanoparticles, which are able to reversibly tune the mobility and momentum scattering [97]. However, due to the relatively large size ($\sim$ 13 nm, which is over 50 lattice constants) of the nanoparticles used in that study, it is not possible to draw conclusions for atomic-scale CI scatterers such as surface adatoms and impurities in the SiO$_2$ substrate. In contrast, Mg adsorbates are able to probe the atomic-scale regime. With the agreement between two quite different experiments (Mg adsorbates deposited in UHV and organic-ligand bound nanoparticles deposited by drop casting) probing different length scales of the scattering potential, it is clear that spin relaxation in graphene is not determined by CI scattering despite its importance for momentum scattering.

It is also worth mentioning that this result is not incompatible with the early experiments showing a linear relation between τ_s and D by tuning the carrier concentration [70, 72]. While Mg adsorbates modify τ_p by introducing CI scattering and possibly local Rashba SO coupling, there are many alternative sources which might contribute to EY (i.e. weak scatterers, resonant scattering, phonon scattering) which could still present themselves as the carrier concentration is tuned leading to $\tau_s \sim D$. Thus, EY spin relaxation originating from sources other than CI scattering is still viable.

Some other possibilities to consider are DP spin relaxation in spatially inhomogeneous Rashba SO fields. It has recently been proposed that this type of SO coupling can result in a competition between EY-like and DP-like scaling behavior to yield unconventional scaling between τ_s and τ_p [86]. Another possibility is that the spin lifetime is limited by contact effects such as inhomogeneous stray fields [96]. Due to its atomically thin nature, this could have a larger effect for graphene compared to semiconductor or metallic spin transport systems that are typically much thicker.

9.3 Conclusion

In conclusion, we have investigated charge and spin transport in SLG by systematically introducing CI scatterers in the form of Mg adsorbates. The introduction of Mg was shown to transfer electrons to the SLG and decrease the momentum scattering time. Despite pronounced changes in momentum scattering, no significant variation was seen in spin relaxation. This indicates that CI scattering is not an important source of spin relaxation in SLG in the current regime of spin lifetimes ($\sim$1 ns).

Chapter 10

Appendix A: Growth Recipes

10.1 Introduction

In this section I will outline the step-by-step growth procedures for a variety of growths to serve as a guide to other group members. All detailed recipes were developed in the Kawakami group main chamber for growths on ‘Adrian’s’ sample platen (pocket). ‘Jared’s’ pocket registers similar sample thermocouple temperatures.

10.2 Mg Distillation and MgO Homoepitaxy

10.2.1 A (Recent) Growth Perspective on MgO

Our group has looked for various ways to grow flat crystalline MgO. Before I joined the group, several key results had already been achieved for FPP projects and graphene spintronics. Yan Li developed a reactive growth using elemental Mg and molecular oxygen which she was able to deposit single crystal on GaAs. However, through her work on FPP, these films were shown to have Mg-rich interfaces [48]. Wei-Hua Wang, Wei Han, and Kyle Pi had demonstrated that by using a single crystal MgO target, e-beam MgO can grow flat on HOPG and graphene with a small amount of Ti seeding [388]. This led directly to huge success in achieving high quality tunneling spin injecting contacts to graphene [71]. Lastly, and most relevant for what follows, Jared Wong and Richard Chiang showed that annealing MgO(001) substrate can often bring contaminants to the surface of the MgO substrate and that metals growths (Co, Fe, Ag) directly on bare MgO substrate resulted in contaminated films. Therefore, they developed a recipe for growing homoepitaxial MgO buffer layers that were flattest at around 350 °C [289]. The RHEED patterns of the underlying MgO substrate is vastly improved after adding a 10 nm buffer layer of e-beam MgO (see Fig. 10.1). For the e-beam MgO deposition on Ge, following Jared's approach with homoepitaxy, Wei discovered that there is an optimal temperature around 250 °C where the films demonstrate best crystallinity and smoothness [342]. This work directly led to my realization that the same should be true for Si and GaAs. And both recipes for e-beam MgO growth on Si demonstrate an optimal temperature for best crystallinity and smoothness. We have since learned, mainly from experience with EuO, that the reason for this optimal temperature is most likely related to a distillation effect.

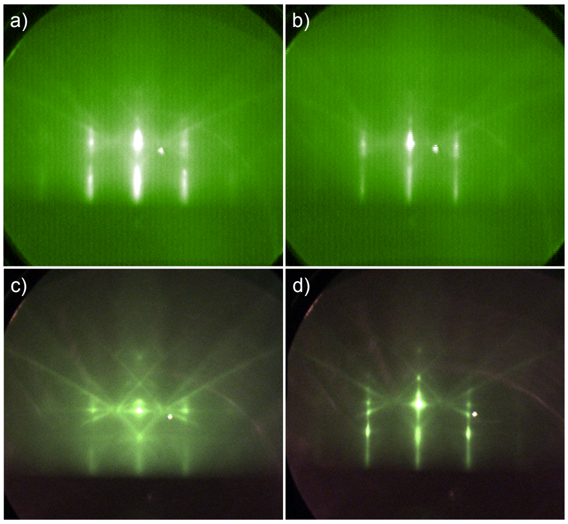

Figure 10.1: Homoepitaxy of e-beam MgO on MgO(001). a) RHEED pattern of MgO(001) substrate along [100]. This substrate has been DI rinsed and annealed at 600 °C for 30 min. Annealing greatly improves the RHEED quality. b) 10 nm homoepitaxy of e-beam MgO at 350 °C on the substrate shown in a). Images taken in 2010. c) RHEED images of MgO(001) along [100] after annealing at a steeper rocking angle using the new CCD camera. Image is from May 2011. d) Subsequent homoepitaxy of 10 nm MgO(001) along [100]. Sharpened streaks, spots, and Kikuchi lines indicated improvement in the crystalline surface. The anomalous spot in each image is a hole in the phosphorous screen. The screen was eventually replaced (after these images were taken) with a STAIB phosphorous screen with Al coating, which significantly reduces IR background from the heater. Images are taken at 15 keV.

10.2.2 Mg Distillation

At UHV pressures, Mg evaporates at reasonably low temperatures (< 500°C). Using a low temperature effusion cell, I have followed the procedure for investigating distillation as developed for Eu. Fig. 10.2 illustrates this procedure. Fig. 10.2 a) shows a 4 nm e-beam MgO buffer layer on MTI Corp. MgO(001) substrate. The substrate has been treated by deionized (DI) water rinse followed by 600 °C anneal in UHV. A 4 nm MgO e-beam buffer layer is deposited at 350 °C. The sample is then heated to 500 °C for distillation testing. At 500 °C, the Mg cell is opened under UHV condition (no molecular oxygen leak). If the MgO

RHEED pattern remains precisely unaltered, except for some possibility of a slight decrease in intensity, then Mg is under distillation condition. Fig. 10.2 b) displays the MgO buffer layer exposed to the Mg flux rate of what is supposed to be 4 Å/min as calibrated by the quartz crystal monitor. The RHEED pattern remains unaltered indicating that Mg has zero sticking probability to MgO at above 500 °C. The sample is then cooled to 300 °C and this temperature is maintained for $\sim$10 min. Again the RHEED pattern is unaltered, indicating distillation. The sample is then subsequently cooled to 200 °C and then 150 °C, which both indicate distillation, despite being below the temperature of evaporation according to the thermal cell. At 55 °C (Fig. 10.2 f)), we see that the RHEED pattern is altered by increased Mg sticking probability and resulting Mg overlayer. The Mg cell is then closed and the sample is heated to 150 °C, where the Mg overlayer RHEED pattern begins to undergo changes possibly due to re-evaporation or atomic diffusion and smoothing associated with annealing process. Heating to 300 °C, as shown in Fig. 10.2 h) returns the sample to it's original RHEED pattern of the MgO buffer layer, demonstrating full re-evaporation of the deposited Mg layer of approximate thickness $\leq$ 8 nm. This is a remarkable result.

We can then understand the excellent quality of e-beam MgO homoepitaxy in the following way. In the e-beam source, electrons bombard the source crystalline MgO target and dissociate Mg and O which normally leads to MgO with oxygen vacancies. However, deposition at elevated temperatures allows for surface diffusion of any Mg atoms, as well as distillation of excess Mg, leading to stoichiometric films.

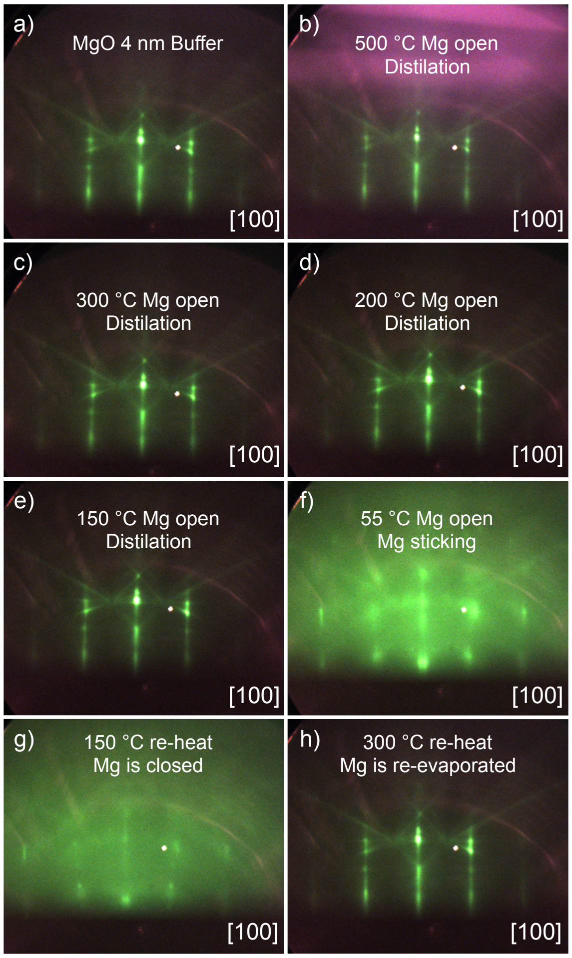

Figure 10.2: Evolution of Mg Distillation. a) MgO (4 nm) e-beam buffer layer grown at 350 °C on MgO(001). b) same 4 nm MgO buffer layer exposed to a Mg flux at 500 °C. c) - d) The substrate temperature is the decreased sequentially with stops at 300 °C (c), 200 °C (d), 150 °C (e), and 55 °C (f). The sticking probability of Mg increases below 150 °C allowing for the growth of a metallic Mg overlayer. After 20 minutes of deposition at 55 °C, the Mg shutter is closed. g) The sample is then re-heated to 150 °C and the Mg overlayer pattern begins to change. h) The original MgO e-beam buffer layer pattern returns after post annealing the Mg/MgO system to 300 °C. This can be understood as re-evaporation of the Mg overlayer.

10.2.3 MgO Homoepitaxy by rMBE

While e-beam MgO homoepitaxy provides excellent single crystal MgO surfaces for growth studies, the e-beam style of deposition is limited by growth rate and total thickness. The higher the rate of e-beam deposition (higher the power), the more oxygen vacancies are in-

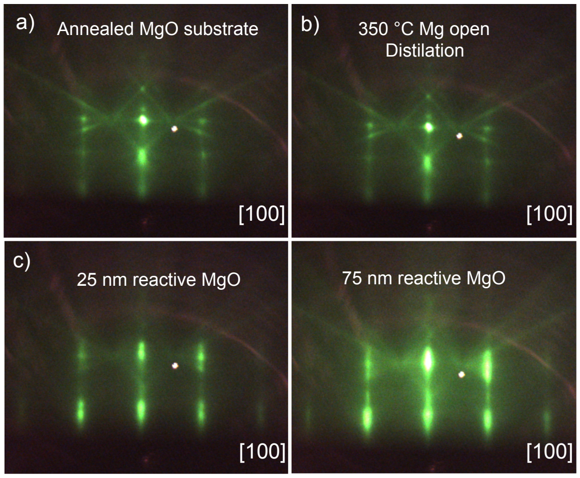

Figure 10.3: Homoepitaxy of Reactively Grown MgO on MgO(001). a) Annealed MgO(001) substrate. b) MgO substrate maintained at 350 °C and with incident Mg flux in distillation mode. c) 25 nm reactive growth of MgO through oxidation of elemental Mg flux. d) Final RHEED pattern of 75 nm rMBE MgO homoepitaxial film on MgO(001).

troduced. Also, e-beam rates in our MBE chamber, generally never exceed 3 Å/min because the source will run out of material very quickly. For this same reason, thick films above 10 nm are not experimentally realistic. For instance, while doing growth studies that involve 10 nm buffer layers, running out of MgO is the main reason for chamber vents, on the order of every 2 months. For each vent, it takes 1.5 - 2 weeks to get the chamber back up and fully running with clean material leading to a down time of 20%, which is not good for research. On the other hand, thermal evaporation sources of the high temperature variety, need refilling approximately every 2 vents (∼4 – 6 months depending on usage). The low temperature effusion cells require filling at most once per year. Therefore, having thermal sources is desirable if thicker MgO films are needed. With the discovery of Mg distillation, it then became feasible to grow thick (> 100 nm) films, with only a moderate decrease in quality from the e-beam MgO growths.

Fig. 10.3 shows the RHEED patterns for rMBE homoepitaxy of MgO on MgO(001) substrate. The substrate is first DI rinsed and the subsequently UHV annealed at 600 °C for 1 hour (Fig. 10.3 a)). The sample is then cooled to RT to take a Mg deposition rate, which was determined to be 4.1 Å/min. The sample is then heated to 350 °C and the temperature is allowed to stabilize. Next, the Mg shutter is opened and the incident Mg flux, in distillation condition, re-evaporates off the substrate surface leaving the RHEED pattern unaltered (Fig. 10.3 b)). The growth commences with the introduction of an oxygen partial pressure. Growth in the distillation regime for MgO differs, and is in fact simpler, from that of EuO growth. As MgO is the thermodynamically stable oxide [287], there is no need to worry about other oxidation states, and therefore no need to worry about limiting the oxygen content supplied during the growth. Therefore, we can simply overpressure with oxygen such that the flux of oxygen exceeds the Mg flux supplied to the substrate. For the reactive growth shown in Fig. 10.3 c) and d), $P_{O_2} \sim 1 \times 10^{-7}$ Torr. After 75 nm of growth. To terminate the growth, since there is no concern for over-oxidation of the MgO overlayer, the Mg shutter is first closed. (This is opposite of EuO growth termination). The total chamber pressure increases from 1.0×10^{-7} to 1.6×10^{-7} Torr, indicating that at 4.1 Å/min of Mg, about $\sim 5 \times 10^{-8}$ Torr molecular oxygen partial pressure is needed to fully oxidize the incoming Mg flux. The final homoepitaxial MgO film of 75 nm is shown in figure 10.3 d). The RHEED indicates some islanding, and that the e-beam MgO produces higher quality crystalline surfaces (compare with fig. 10.1 d) and 10.2 a)), but that the growth by rMBE is really quite good.

10.2.4 Recipes for MgO Homoepitaxy

Homoepitaxy of e-beam MgO buffer layers

1. Rinse MgO(001) substrate with DI water ($\sim$ several seconds). Substrate is usually 10 mm x 10 mm x 0.5 mm double side polished from MTI corp.

2. Blow dry with nitrogen.

3. Mount with Ta foil on corners to Thermionics sample platen (pocket).

4. Load into load-lock and pump down. Once pumped, Transfer to main chamber.

5. Take initial RHEED images along MgO(001) [100] and [110]. Pattern should appear slightly blurry.

6. Anneal in UHV at 600 °C for 1 hour. (Optional: Anneal in O_2 partial pressure of $\sim 5 \times 10^{-8}$ – 1×10^{-7} Torr.) Cool to RT when done.

7. Take post-anneal RHEED images along MgO(001) [100] and [110]. RHEED patterns should be much improved, but there should be some obvious broadening of the diffraction streaks.

8. Warm up e-beam MgO cell to deposition power. HV = 4.8 kV. Emission $>$ 8 mA. 17mA is maximum power and usually means you are out of MgO and the e-beam is now punching through the MgO crystal to the Ta crucible and your samples will be contaminated with Ta. This can be verified checking for Ta in Auger spectroscopy data.

9. Move sample into deposition monitor position (beyond x = 1.9 inches) and load in deposition monitor. Take MgO rate. When done, close MgO shutter, wheel out the deposition

monitor, and return sample to growth position (x = 1.3 inches). Typical MgO rate is ~ 1 – 1.5 Å/min with a background pressure of $\sim 1 \times 10{-}8$ Torr.

10. Heat substrate to T$_S = 350$°C (T$_M \sim 440$°C) and allow temperature to stabilize. Temperature stabilization is certain once T$_M$ is constant.

11. Deposit 10 nm e-beam MgO, which should take $\sim$ 1 - 1.5 hours. Close MgO shutter at end of growth and turn off e-beam power supply.

12. Cool sample to RT and take final RHEED patterns along MgO(001) [100] and [110].

Homoepitaxy of Reactive MgO Layers

1. Rinse MgO(001) substrate with Di water ($\sim$ several seconds). Substrate is usually 10 mm x 10 mm x 0.5 mm double side polished from MTI corp.

2. Blow dry with nitrogen.

3. Mount with Ta foil on corners to Thermoinics sample platen (pocket).

4. Load into load-lock and pump down. Once pumped, Transfer to main chamber.

5. Warm up Mg cell to growth temperature.

6. Take initial RHEED images along MgO(001) [100] and [110]. Pattern should appear slightly blurry.

7. Anneal in UHV at 600 °C for 1 hour. (Optional: Anneal in O$_2$ partial pressure of $\sim 5 \times 10^{-8}$ – 1×10^{-7} Torr.) Cool to RT when done.

8. Take post-anneal RHEED images along MgO(001) [100] and [110]. RHEED patterns should be much improved, but there should be some obvious broadening of the diffraction streaks.

9. Move sample into deposition monitor position (beyond x = 1.9 inches) and load in deposition monitor. Take Mg rate. When done, close Mg shutter, wheel out the deposition monitor, and return sample to growth position (x = 1.3 inches). Typical Mg rate can be anywhere between $\sim$ 1 – 8 Å/min depending on the desired final thickness and available growth time. We have found that 4 Å/min produces good film quality.

10. Heat substrate to T$_S$ $= 350$ °C (T$_M$ ~ 440 °C) and allow temperature to stabilize. Temperature stabilization is certain once T$_M$ is constant.

11. Open Mg shutter and allow for Mg distillation for a few minutes to allow the cell and system to come into steady state.

12. Open O_2 leak valve and stabilize oxygen partial pressure depending on Mg deposition rate. Typically 1×10^{-7} Torr should suffice for an Mg rate of $\sim$ 4 Å/min. Deposit for the desired time and monitor the total chamber pressure to make sure the oxygen partial pressure remains stable.

13. Terminate growth by closing the Mg shutter and oxygen leak valve. The order is irrelevant. This is because closing the oxygen leak first, with Mg flux still incident on the sample, will just result in Mg distillation. On the other hand, closing the Mg first, with oxygen still in the chamber, does not over-oxidize the MgO film as it is already stoichiometric and thermo-

dynamically stable. However, closing the Mg shutter first will tell you the amount of oxygen partial pressure that was used for full conversion. For instance, if the total pressure during growth is 1.0×10^{-7} Torr, and then the growth is terminated my closing the Mg shutter, the resulting chamber pressure may increase to 1.3×10^{-7} Torr, indicating that only 3×10^{-8} Torr was needed for achieving stoichiometric growth.

14. Cool sample to RT and take final RHEED patterns along MgO(001) [100] and [110].

10.3 MgO on Semiconductors by e-beam Deposition

10.3.1 MgO on GaAs(001)

There are several GaAs substrates that have been involved in growths here at UCR. We have examined substrates provided by three sources: i) collaboration with the Awschalom group at UC Santa Barbara, ii) AXT, inc., and iii) MTI Corporation. The samples provided by the Awschalom group are by far the best in terms of versatility, crystalline quality, and spin properties. GaAs supplied by AXT has shown to have moderate spin lifetimes of several nanoseconds (see Fig. 10.4). MTI substrates show characteristic semiconducting properties, but time resolved TRKR measurements showed no spin signals. The substrates provided by Awschalom's group are best for high quality optical studies of spin dynamics, the AXT substrate is acceptable for large wafer (>1 cm) spin injection for experiments such as the slow muons projects. Much of the substrate preparation, growth, and subsequent processing for optical experiments, is discussed in detail in Yan Li's Ph.D. thesis [389] and will not be

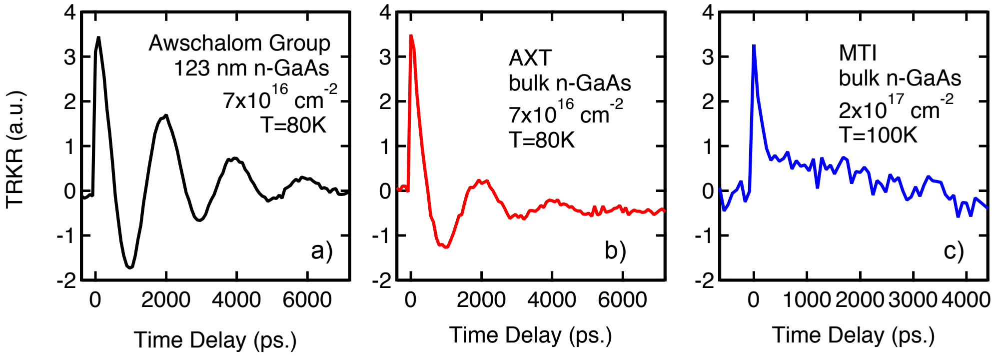

Figure 10.4: Comparison of Spin Lifetimes by TRKR on Different GaAs Substrates. a) Time resolved Kerr rotation (TRKR) measurements tuned to the band gap of GaAs at T = 80 K on a sample of n-GaAs with optimal doping of 7×10^{16} cm^{-2}. The sample structure is MgO 2(nm) / n-GaAs (123 nm) / Al$_x$Ga$_{1-x}$As (400 nm) / GaAs(001). The applied field of $B = 900$ Oe allows for the optically injected spin population to precess, which generates the oscillations observed in the data. b) TRKR measured on bulk substrate from AXT for $B = 900$ Oe. There is a slight decrease in spin lifetime as can bee seen in the faster decoherence (faster damping of the oscillating curve) as a function of time. c) TRKR measured on bulk n-GaAs from MTI for $B = 900$ Oe. There is no evidence for optical spin orientation.

discussed here. Below I will briefly outline the step-by-step procedure for growing e-beam MgO on 2x4 reconstructed GaAs surfaces. 2x4 reconstructed surfaces can be achieved on samples provided by the Awschalom group which are As capped. Desorbing of the arsenic cap and subsequent annealing to $\sim$ 420 °C yields 2x4 reconstructed surfaces. See [390] for a review on GaAs reconstructed surfaces.

Recipe

1. Cleave the GaAs(001) substrate provided by Awschalom's group. The substrate has the following structure As / n-GaAs* / Al$_x$Ga$_{1-x}$As (400 nm) / GaAs(001). the n-GaAs* layer can be of varying thickness and doping upon request. Over the years Shawn Mack has been generous in providing samples to our group. Common doping is usually between 1×10^{16}

cm^{-2} and 1×10^{19} cm^{-2} depending on the desired spin-based application. Similarly the thickness can vary, depending on the application and desired depletion region [103, 391, 102, 392, 393]. A typical sample, for which the only concern is high quality optical spin experiments, consists of 123 nm with optimal doping for longest spin lifetime [103] of $\sim 10^{16}$ cm^{-2}. The Al$_x$Ga$_{1-x}$As acts as an etch stop for TRFR experiments. For more detail see ref. [389]. Note: cleaving As capped GaAs may be toxic and a face mask should be worn. All dust should be properly disposed of.

2. Mount with Ta foil on corners to Thermoinics sample platen (pocket).

3. Gently wipe the sample face clean with IPA using a lens tissue. Never wipe with the same part of the lens tissue. The point is to remove any dust from the cleaving process. Re-wiping with the same lens tissue could scratch the surface by scraping the already removed dust particles back along the surface.

4. Blow dry with nitrogen.

5. Load into load-lock and pump down.

6. Once pumped, transfer onto the buffer heater or into the main chamber for desorbing of As capping layer. Note: in previous years, desorption of the As capping layer was done in the buffer chamber at ~320 °C according to the buffer heater thermocouple. However, recently, due to a teaching experience mishap, the buffer heater now sits further back in the buffer heater port. Desorbing As in the buffer heater now seems to contaminate GaAs samples and so desorbing As should take place in the main chamber. The reason for the current problem

in the buffer chamber is due to desorbing of gasses off the buffer chamber port walls during annealing, which doesn't seem to affect other annealing procedures (i.e. Graphene device annealing at 150 °C), but does affect the GaAs As desorbing. An advantage of desorbing in the main chamber is that the RHEED pattern can be carefully monitored to find the exact temperature for desorption and reconstruction.

7. In the main chamber, heat the GaAs substrate to 350 °C (T$_M$ ~ 440°C). At this temperature the As cap should desorb and the chamber pressure will rise. Wait for full desorption of the As layer. The chamber pressure should decrease to $\sim 1 \times 10^{-9}$ Torr. Monitor the RHEED pattern, which should appear after desorption. There should be no RHEED pattern before that As cap is desorbed.

8. Cool the sample to RT and re-orient the sample along [110] or [1$\bar{1}$0] direction.

9. Heat substrate to T$_S = 350$ °C (T$_M$ ~ 440 °C).

10. In 10 °C increments, heat the substrate until 2x4 reconstruction is achieved. The RHEED patterns for 2x4 reconstructed GaAs are shown in section 5.3, figures 5.2 a) and 5.2 b).

11. Cool the sample to RT and take RHEED along GaAs(001) [110] and GaAs(001) [1$\bar{1}$0] direction.

12. Warm up MgO cell to deposition power. HV = 4.8 kV. Emission $>$ 8 mA. 17mA is maximum power and usually means you are out of MgO and the e-beam is now punching through the MgO crystal to the Ta crucible and your samples will be contaminated with Ta. This can be verified checking for Ta in Auger spectroscopy data.

13. Move sample into deposition monitor position (beyond x = 1.9 inches) and load in deposition monitor. Take MgO rate. When done, close MgO shutter, wheel out the deposition monitor, and return sample to growth position (x = 1.3 inches). Typical MgO rate is ~ 1 – 1.5 Å/min with a background pressure of $\sim 1 \times 10^{-8}$ Torr.

14. Heat to T$_S = 300$ °C (T$_M \sim 390$ °C).

15. Deposit 2 nm e-beam MgO. Close MgO shutter at end of growth and turn off e-beam power supply.

16. Cool sample to RT and take final RHEED patterns along MgO(001) [110] // GaAs(001) [1$\bar{1}$0] and MgO(001) [100] // GaAs(001) [100].

10.3.2 MgO on Si(001) for Al/Fe/MgO/Si Collaboration with OSU

This is the growth recipe for the silicon spin injection collaboration with the Center for Emergent Materials (CEM) at The Ohio State University. Samples of commercial silicon on insulator (SOI) are shipped from OSU to UCR for growth. Measurements are performed at OSU. Note: For safety, **all etching processes for silicon should be done in the UCR Cleanroom at the specified Acid bench**. The cleanroom has proper safety equipment and clothing coverings including special gloves for working with HF, aprons for working with acids, and face masks. **You must get proper cleanroom and acids bench training by cleanroom facilities personnel AND special training for this particular etch from an older grad student before using this procedure.** Additional note: The cleanroom nitrile gloves sometimes have holes in them even though they should not. Be sure to wear two pairs

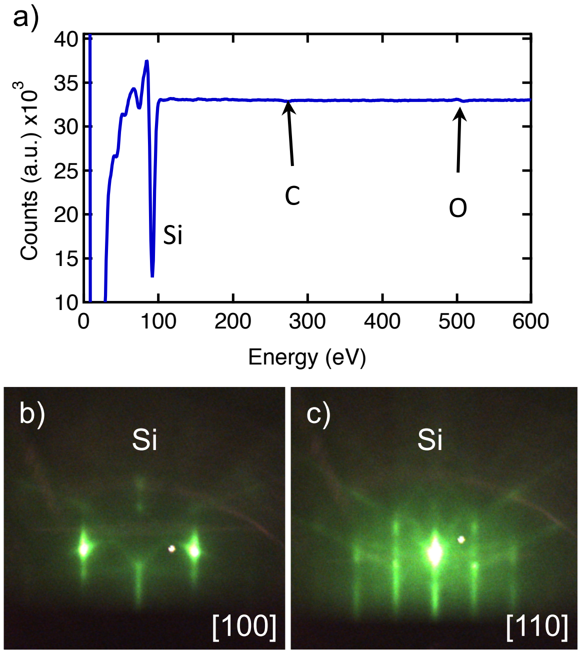

Figure 10.5: RHEED and Auger of Si. a) Auger spectroscopy of UHV annealed p-Si (SOI). p-SOI substrate was prepared as described in this recipe. RHEED of p-Si (SOI) along c) Si(001) [100] and d) Si(001) [110].

of nitrile gloves and bring an extra pair into the cleanroom in case you wish to dispose of the top pair and replace with a fresh set of gloves. Also, cleanliness of acid etching is extremely important and the beakers used for Si etching should only be used for this procedure, should be properly labeled, and kept separate from other stored beakers. This last one will keep people from using them accidentally for something else. We have had trouble with cross contamination of beakers affecting the subsequent growths.

Recipe

Si Substrate Preparation

A) Pre-clean the beakers before etching.

0. *Prep for later growths by taking Fe and Al deposition rates before sample is in the chamber. Target rates: Fe* $\sim$ *1 – 2 Å/min, Al* $\sim$ *1 – 2 Å/min. Typical background pressures due to elemental vapor pressure are* $< 1 \times 10^{-9}$ *Torr for Fe, and* $< 2 \times 10^{-9}$ *Torr for Al. Rates can be taken during etching time in UCR cleanroom (takes about 1/2 hour) and during load lock pump down time (takes about 1/2 hour).*

1. In UCR cleanroom, rinse graduated cylinder, plastic funnel, 2 plastic beakers, 2 glass beakers, Teflon tweezers and small jar with water three times each. We have special equipment in the UCR cleanroom for this.

2. Mix the piranha solution (12 ml H_2SO_4 99% and 12 ml H_2O_2 30%) in the *piranha etch* glass beakers and let sit for a few minutes.

3. Pour the same piranha solution into the *piranha rinse* glass beaker and wait a few minutes.

4. Rinse both piranha beakers three times. The piranha solution can be poured into the cleanroom sink which is set up for acid disposal.

5. Mix the dilute HF solution (100 ml DI H_2O and 3 ml HF (hydrofluoric acid) 50%) in the *HF etch* plastic beaker and wait a few minutes.

6. Pour the HF solution into the *HF rinse* plastic beaker.

7. Rinse both HF beakers three times. The HF solution can be poured into the cleanroom sink.

B) Si substrate etch

1. Mix a new batch of acid solutions in the proper beakers. (Pihrana: H_2SO_4(99%) : H_2O_2(30%) 12 ml:12 ml. HF: DI H2O2(100%):FH(50%) 100 ml:3 ml.) Fill the rinse beakers and small glass jar with DI.

2. Spray the Si substrate with DI and blow dry with nitrogen gas.

3. Using Teflon tweezers, place sample into *piranha etch* solution. Etch for 2 minutes. (The piranha etch is a strong metals etch, which is meant to clean the surface of contaminants.)

4. Using Teflon tweezers, remove sample from *piranha etch* solution and place in *piranha rinse* beaker. Let sit 1 minute.

5. Using Teflon tweezers, remove sample from *piranha rinse* and place in *HF etch* solution. Etch in HF solution for 1 minute. (HF dip etches any SiO_2 on the surface leaving the surface H-passivated Si. Si is hydrophobic and so water should ball up on the surface.)

6. Using Teflon tweezers, remove sample from *HF solution* and place in *HF rinse* beaker.

7. Using Teflon tweezers, remove sample from *HF rinse* and place in *small jar*, which should be half filled with DI. Do not blow dry. Place the cap on the small jar and screw tightly. Be careful, the small jar cap is not really water tight and it will leak. Hold the small jar upright at all times and try not to splash the water inside around. The substrate should be kept in the DI water at all times during transport and never exposed to air. The purpose of the small water

filled jar is to keep the silicon surface from re-oxidizing in the time it takes between the HF dip in the cleanroom and loading into the load lock in our lab.

8. Clean all beakers with DI rinse in the acids sink 3 times and dry them with nitrogen gas and then with kimwipes. Put everything away in the proper place.

9. Carry the sample in the small jar with DI back to the main lab.

C) Substrate anneal and Auger characterization

1. Sample should currently be in small jar with DI water to protect from oxidation. Do not expose Si to air longer then 5 minutes.

2. Remove sample from small jar with DI.

3. Blow dry with nitrogen.

4. Mount with Ta foil on corners to Thermoinics sample platen (pocket).

5. Load into load-lock and pump down. Once pumped, transfer sample to buffer chamber.

6. Do Auger spectroscopy on the sample (0-600 eV at 1 mV sens., 600-2000 at 100 – 300 μV sens.). Confirm Si peaks and examine C and O content.

7. Transfer sample into main chamber. Take RHEED images along [100] and [110] at RT

8. Anneal under UHV conditions at T$_S$ $= 550$ °C (T$_M$ ~ 650 °C) for 30 min. Annealing above 400 °C removes H-passivation.

9. Cool to RT and take RHEED images along [100] and [110].

10. Warm up auger with the sample still in the main chamber.

11. Transfer into the buffer chamber and do Auger spectroscopy (0-600 eV at 1 mV sens., 600-2000 at 100 – 300 μV sens.). It should be the same as before the anneal.

12. Transfer sample back into the main chamber.

e-beam MgO Growth on Si

1. After substrate anneal, subsequent Auger, and return of sample to main chamber, take RHEED images along Si(001) [100] and [110].

2. Warm up e-beam MgO cell to deposition power. HV = 4.8 kV. Emission $>$ 8 mA. 17mA is maximum power and usually means you are out of MgO and the e-beam is now punching through the MgO crystal to the Ta crucible and your samples will be contaminated with Ta. This can be verified checking for Ta in Auger spectroscopy data.

3. Move sample into deposition monitor position (beyond x = 1.9 inches) and load in deposition monitor. Take MgO rate. When done, close MgO shutter, wheel out the deposition monitor, and return sample to growth position (x = 1.3 inches). Typical MgO rate is $\sim$ 1 – 1.5 Å/min with a background pressure of $\sim 1 \times 10^{-8}$ Torr.

4. Heat substrate to $T_S = 200$ °C ($T_M \sim 270$ °C) and allow temperature to stabilize. Temperature stabilization is certain once T_M is constant.

5. Deposit 1.3 nm e-beam MgO at $T_S = 200$ °C. Close MgO shutter at end of growth and turn off e-beam power supply.

6. Cool sample to RT and take final RHEED patterns along MgO(001) [100] // Si(001) [100] and MgO(001) [110] // Si(001) [110] (Fig. 10.6). For MgO thicknesses below 2 nm, a RHEED pattern will be difficult to see. The growth is cube-on-cube.

7. Warm up auger while the sample is still in the main chamber.

8. Transfer into the buffer chamber and do Auger spectroscopy (0-600 eV at 1 mV sens., 600-2000 at 100 – 300 μV sens.). It should show clear Mg, Si, and O peaks.

9. Transfer sample back to main chamber.

Discussion and Analysis

200 °C is the optimal growth temperature of e-beam MgO on Si. This was determined by several growths at various substrate temperatures from the quality of the RHEED and AFM rms roughness. AFM on 2 nm e-beam MgO/Si(001) grown at 200 °C yielded an RMS roughness of 0.12 nm. At 2 nm, the MgO shows crystalline RHEED pattern (not shown) with cube-on-cube growth. For reference, growth at 400 °C resulted in rms roughness of 0.77 nm. RHEED images for the Si substrate and subsequent 1.3 nm MgO overlayer (as used in the Ohio state collaboration) is shown in figures 10.5 b) and 10.6 c), respectively. Of the three main semiconductors (Si, GaAs, Ge), MgO growth on Si is by far the worst. It has been reliably reported that growth of MgO on Si can result in interfacial oxidized Si, leaving at least 1 ML of SiO_x [338, 340]. Nevertheless, based on Yong Pu's work on spin injection in these samples, it has been determined that the materials we have provided give the lowest number of interfacial states in the reported literature for 3T spin injection experiments [394].

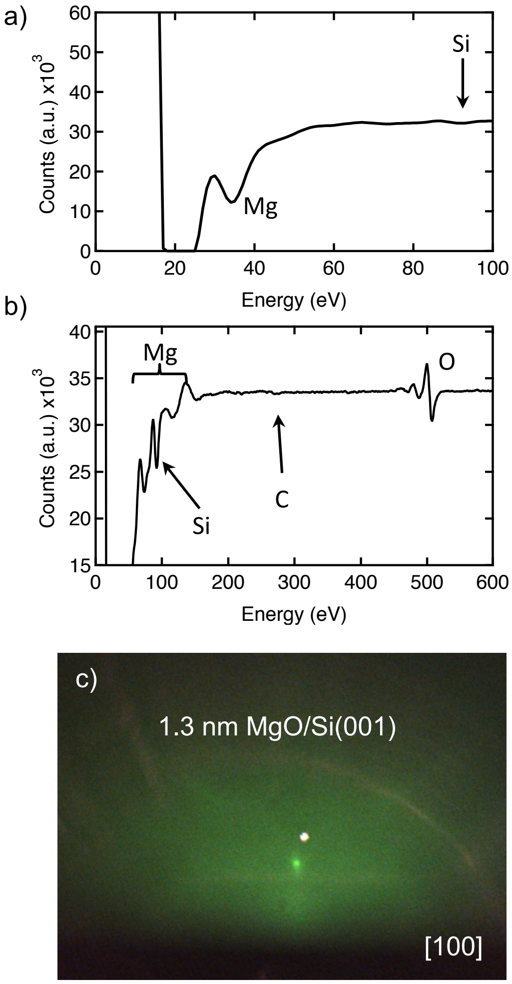

Figure 10.6: RHEED and Auger of e-beam MgO/Si. a) Auger spectroscopy of MgO (1.3 nm) / p-SOI(001). p-Si substrate was prepared as described in this recipe. b) RHEED MgO (1.3 nm) / Si(001) along [100].

Fe and Al Deposition on MgO/Si

Recipe

1. After e-beam MgO deposition, subsequent Auger, and return of sample to main chamber, take RHEED patterns along MgO(001) [100] // Si(001) [100] and MgO(001) [110] // Si(001) [110].

2. Deposit 10 nm elemental Fe at RT. P$_{MBE} < 1 \times 10^{-9}$ Torr.

3. Examine RHEED of Fe (10 nm) / MgO (2 nm) / Si(001).

4. Warm up auger while the sample is still in the main chamber.

5. Transfer into the buffer chamber and do Auger spectroscopy (0-800 eV at 1 mV sens.). It should show clear Fe peaks and possibly some remanence of the underlying Si, Mg, and O peaks.

Note: Auger spectroscopy at this point in the growth is critical to the subsequent fabrication based on wet etching at Ohio State as developed by Yong Pu. The slight oxidation of the Fe layer allows for smooth and sustained Al growth. Without the Auger step to slightly oxidize the Fe, the Al will not stick to the Fe layer and the resulting sample will come out looking too thin and "blue". These sample will not etch properly. The final film should look like an aluminum metal layer (i.e. the color should be that of aluminum (i.e. silvery-ish)).

6. Transfer sample back to main chamber.

7. Deposit 20 nm elemental Al at RT. P$_{MBE} < 2 \times 10^{-9}$ Torr.

8. Examine RHEED of Al (20 nm) / Fe (10 nm) / MgO (2 nm) / Si(001). It should be polycrystalline or amorphous.

9. Warm up auger while the sample is still in the main chamber.

10. Transfer into the buffer chamber and do Auger spectroscopy (0-800 eV at 1 mV sens., 800-2000 at 100 – 300 μV sens.). It should show Al peaks. The underlying MgO and Si should not be seen.

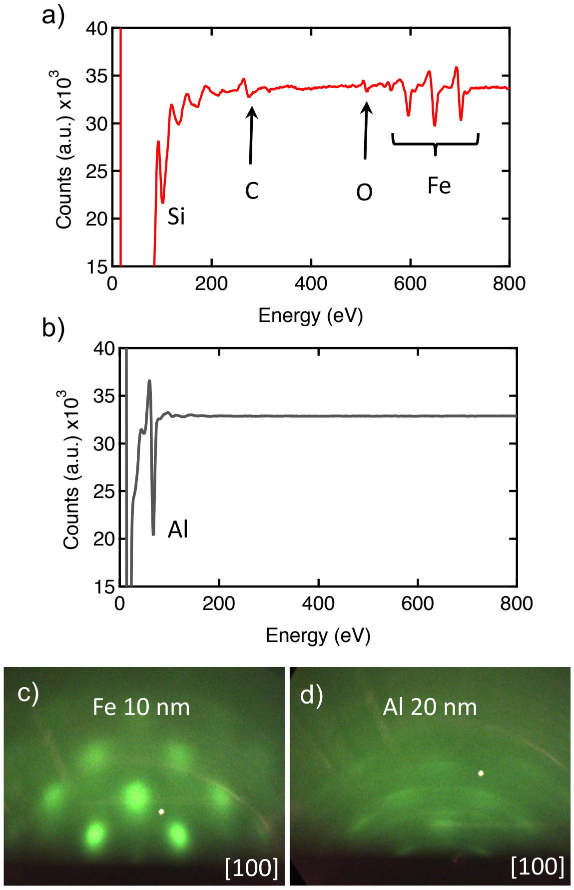

Figure 10.7: RHEED and Auger of Al/Fe/MgO/Si. a) Auger spectroscopy of Fe (10 nm) / MgO (1.3 nm) / p-SOI(001). b) Auger spectroscopy of Al (20 nm) / Fe (10 nm) / MgO (1.3 nm) / p-SOI(001). c) RHEED Fe (10 nm) / MgO (1.3 nm) / p-SOI(001) along [100]. d) RHEED Al (20 nm) / Fe (10 nm) / MgO (1.3 nm) / p-SOI(001) along [100].

10.4 EuO Growths on Various Substrates

Here I outline the growth procedures for growing EuO in the distillation and oxygen-limited regime on YSZ, EuO/MgO/GaAs, EuO/TiO_2/MgO, and EuO/HOPG. The main results of this work is summarized in chapters 6, 7, and 8.

10.4.1 EuO/YSZ(001)

Recipe

1. Warm up Eu cell to growth temperature to allow it to degas a bit during pump time.

Optional: Keep Eu cell at mid-range growth rate (2 Å/min) overnight for better degas.

2. Sonicate YSZ(001) substrate in Acetone for 10 minutes. YSZ(001) is generally 10 mm x 10 mm x 0.3 (or 0.5) mm double or single side polished from MTI corporation. Be careful, sometimes their substrates do not come oriented as advertised. Often it comes miscut with [100] not oriented along a cleaved plane. Optional: Sonicate additional 10 minutes in IPA.

3. Mount with Ta foil on corners to Thermoinics sample platen (pocket).

4. Load into load-lock and pump down.

5. While pumping, take Eu rate. Move manipulator into deposition monitor position (x $>$ 1.9). Wheel in deposition monitor. Eu rate should be between 8 and 9 Å/min. Pay close attention to the chamber pressure due to the Eu cell. When done, remove deposition monitor and put manipulator back into transfer position.

6. Transfer sample into main chamber.

YSZ has awful charging effect in the RHEED at low temperature. You will only get RHEED above 250 °C. Once you warm it up a bit, you can the orient it along an axis to monitor the sample during growth.

7. Oxygen anneal YSZ(001) substrate 600 °C at $P_{O_2} = 1 \times 10^{-7}$ Torr. Anneal for 3 hours and then close the O_2 leak.

8. Cool to RT. Take RHEED images while the sample is cooling. Below 250 °C, you may lose the RHEED pattern due to charging effect.

Optional Step: Once at RT, transfer the sample from the main chamber to the buffer chamber ($P_{buffer} < 5 \times 10^{-9}$ Torr). Run the TSP in the main chamber to remove any excess oxygen still remaining. even though this oxygen level should now be below 3×10^{-9} Torr, it can still affect the growth of EuO, which is very sensitive. Once done running the TSP, the main chamber pressure should now be the same base pressure from taking the Eu deposition rate earlier. Transfer sample back into the main chamber.

9. Take Eu rate again. Move manipulator into deposition monitor position (x $>$ 1.9). Wheel in deposition monitor. Eu rate should be between 8 and 9 Å/min. Pay close attention to the chamber pressure due to the Eu cell. When done, remove deposition monitor and put manipulator back into growth position (x = 1.3).

There are two reasons for this: i) remove excess oxygen from the chamber. The Eu acts effectively as a TSP. ii) After such a long oxygen anneal at high pressure it is a good idea to re-check the Eu rate is stable and has not dropped appreciably.

10. Heat substrate to $T_S = 450$ °C ($T_M \sim 540$ °C) and allow temperature to stabilize. Temperature stabilization is certain once T_M is constant.

11. Monitor RHEED along a particular axis. [100] often gives the better images, but [110] yields more information as those pesky Eu_2O_3 spots in the RHEED show up best along [110]. You can also set up a time lapse with high frame rate (1 picture every 0.25 seconds or faster) in order to try to obtain RHEED oscillations later. To do this you should be sure to crank

up the intensity on the initial RHEED image as it will fade as the first few monolayers are deposited. Eu deposited on YSZ forms EuO through oxidation supplied by the substrate. In the past I have seen up to 8 ML of growth this way by RHEED oscillations. You can analyze the time lapse after the data is recorded. It is a great improvement that we no longer have to try getting RHEED oscillations in real time with basically only one chance (per sample) to get it right.

12. Open the Eu shutter. This commences the growth of EuO (see Sec. 5.2). Monitor the chamber pressure carefully.

Upon opening the Eu shutter, the pressure will artificially spike due to Eu back heating. It takes $\sim$ *25 - 30 seconds per ML deposition of EuO through substrate supplied oxidation. The RHEED pattern will immediately begin to change. Wait at least 5 minutes for full distillation to occur. After this time the RHEED should be that of thin EuO lattice matched on the YSZ RHEED pattern. After the 5 minute wait time, the Eu vapor pressure, which is the dominant contributor to the current total chamber pressure, should have returned to close to the normal value (the pressure during at which the rate was taken with the deposition monitor).*

13. Wait minimum 5 minutes for full distillation.

14. Leak molecular oxygen such that the partial pressure is $P_{O_2} = 1 - 1.2 \times 10^{-8}$ Torr above the chamber background pressure. Do NOT exceed this value.

15. Grow for the desired amount of time. At this Eu rate and oxygen pressure, EuO will deposit at a rate of $\sim$ 1.67 nm/min (or 5 nm per 30 minutes).

16. Terminate the growth by closing the oxygen leak valve. NEVER close the Eu shutter first.

17. Wait 10 minutes for the residual oxygen in the chamber to pump down. The Eu shutter should still be open, but despite the high flux rate, the Eu material is simply re-evaporating off the surface or depositing a little bit of EuO due to oxidation with the residual O_2.

18. Close the Eu shutter and turn the Eu cell back to base temperature ($T_{Eu} \sim 220$ °C).

19. Cool sample to RT and take final RHEED patterns along EuO(001) [100] // YSZ(001) [100] and EuO(001) [110] // YSZ(001) [110]. The charging effect should be minimal with the EuO overlayer.

20. The sample can be capped at RT by e-beam MgO or Al. 2 – 5 nm is sufficient. A double cap of MgO covered with Al (or Pd) is more effective.

10.4.2 EuO/MgO/GaAs(001)

This section presents a step-by-step recipe for realizing the growth results presented in section 5.3, which contains the relevant RHEED patterns and is also available in [242].

Recipe

1. Follow the recipe for growing MgO on GaAs(001) in section 10.3.1.

2. After MgO growth, take Eu rate. Move the manipulator into deposition monitor position ($x > 1.9$). Wheel in deposition monitor. Eu rate should be between 8 and 9 Å/min. Pay close attention to the chamber pressure due to the Eu cell. When done, remove deposition monitor

and put manipulator back into growth position (x = 1.3).

Optional Alternative Procedure: Take Eu rate along with step 13 of section 10.3.1. And instead of cooling the sample down after the MgO growth (i.e. skip step 16), heat the sample directly to 450 °C and begin EuO growth.

Note: The thickness of the e-beam MgO buffer layer can be altered if desired. I have achieved EuO growth on 0.8 nm MgO on GaAs.

3. Heat substrate to T$_S$ $=$ 450 °C (T$_M$ $\sim$ 540 °C) and allow temperature to stabilize. Temperature stabilization is certain once T$_M$ is constant.

4. Open the Eu shutter. Unlike the case of YSZ, there should be no effect on the RHEED pattern of the underlying MgO buffer layer. Monitor the chamber pressure carefully.

5. Wait minimum 5 minutes for distillation and the chamber pressure to stabilize.

6. Leak molecular oxygen such that the partial pressure is P_{O_2} = 1 – 1.2×10^{-8} Torr above the chamber background pressure. Do NOT exceed this value.

7. Grow for the desired amount of time. At this Eu rate and oxygen pressure, EuO will deposit at a rate of $\sim$ 1.67 nm/min (or 5 nm per 30 minutes).

8. Terminate the growth by closing the oxygen leak valve. NEVER close the Eu shutter first.

9. Wait 10 minutes for the residual oxygen in the chamber to pump down. The Eu shutter should still be open, but despite the high flux rate, the Eu material is simply re-evaporating off the surface or depositing a little bit of EuO due to oxidation with the residual O_2.

10. Close the Eu shutter and turn the Eu cell back to base temperature (T$_{Eu}$ $\sim$ 220 °C).

11. Cool sample to RT and take final RHEED patterns along EuO(001) [100] // GaAs(001) [100] and EuO(001) [110] // GaAs(001) [$1\bar{1}0$] as shown in section 5.3, figures 5.2 e) and 5.2 f), respectively.

20. The sample can be capped at RT by e-beam MgO or Al. 2 – 5 nm is sufficient. A double cap of MgO covered with Al is more effective.

10.4.3 EuO/TiO$_2$/MgO(001)

This section presents a step-by-step recipe for realizing the growth results presented in section 6.4, which contains the relevant RHEED patterns and is also available in [243]. Also, the Methods section section 6.2) provides a comprehensive but concise description of the growth recipe.

Recipe

1. Follow the recipe for growing homoepitaxial 10 nm e-beam MgO buffer layers on MgO(001) in section 10.2.4.

2. With sample at RT and still in the main chamber, Take a Eu rate. Move manipulator into deposition monitor position ($x > 1.9$). Wheel in deposition monitor. Eu rate should be between 8 and 9 Å/min. Pay close attention to the chamber pressure due to the Eu cell. When done, close Eu shutter. Leave deposition monitor in place.

3. Turn on the Ti cell and let warm up. Turn up the filament first to 6 V, 4.4 A. Slowly put a little high voltage onto the grid of approximately 0.05 kV. There should be a current reading

on the power supply although it should be small (a few mA). Begin turning up the HV on the rod to $\sim$ 0.1 kV, there should be minimal current on the rod one or two mA. Slowly turn up the grid to $\sim$ 0.2 kV, and the rod to $\sim$ 2 – 3 kV. The current reading on the grid and rod should be about $\sim$ 60 mA and $\sim$ 15 – 20 mA, respectively.

4. Take Ti rate. This should be done as an immediate step before growing the Ti layer. The Ti e-beam rod source tends to decrease in rate over time and if you wait more than 1 hour between the taking the rate and actually growing the film, you may have a decreased rate by perhaps 20%. The rate should be somewhere between 0.6 – 1.0 Å/min. The cell background pressure should be $< 2 \times 10^{-9}$ Torr. When done, remove deposition monitor and put manipulator back into growth position (x = 1.3).

7. Deposit the desired amount of Ti for 1, 1.5, or 2 ML according to the TiO_2 plane as opposed to a monolayer of hexagonal Ti. For reference, 1 ML = 1.6 Å, 1.5 ML = 2.4 Å, and 2 ML = 3.2 Å. The numbers 1.6, 2.4, and 3.2 Å correspond to the amount of Ti to deposit based on hexagonal crystal structure. For instance, if you take a rate with the deposition monitor of 0.8 Å/min, you should deposit for exactly 2 minutes to achieve necessary number of Ti atoms for 1 ML of TiO_2 lattice matched to MgO. We have found that 2.1 Å of Ti is also reliable for producing the 2x2 TiO reconstruction with the additional higher periodic reconstruction. When done, turn off the Ti cell.

6. Heat substrate to $T_S = 500$ °C ($T_M \sim 610$ °C) and allow temperature to stabilize. Temperature stabilization is certain once T_M is constant.

7. Oxidize Ti layer at 500 °C at P_{O_2} = 1 – 5×10^{-8} Torr for 30 minutes. Close oxygen leak valve when done.

8. Cool sample to RT and take RHEED along MgO(001) [100] and MgO(001) [110] to look for special reconstructions in the MgO pattern. See section 6.4, figure 6.2.

9. Heat substrate to T_S = 500 °C ($T_M \sim 610$ °C) and allow temperature to stabilize. Temperature stabilization is certain once T_M is constant.

10. Open the Eu shutter. This commences the growth of EuO (see Sec. 6.4). Monitor the chamber pressure carefully.

Upon opening the Eu shutter, the pressure will artificially spike due to Eu back heating. It takes an estimated ~ 25 - 30 seconds per ML deposition of EuO through substrate supplied oxidation. The RHEED pattern will immediately begin to change. Wait at least 5 minutes for full distillation to occur. After this time the RHEED should be to that displayed in section 6.4, figures 6.4 a) and 6.4 b). After the 5 minute wait time, the Eu vapor pressure, which is the dominant contributor to the current total chamber pressure, should have returned to close to the normal value (the pressure during at which the rate was taken with the deposition monitor).

11. Wait minimum 5 minutes for full distillation.

12. Leak molecular oxygen such that the partial pressure is P_{O_2} = 1 – 1.2×10^{-8} Torr above the chamber background pressure. Do NOT exceed this value.

13. Grow for the desired amount of time. At this Eu rate and oxygen pressure, EuO will deposit at a rate of $\sim$ 1.67 nm/min (or 5 nm per 30 minutes).

14. Terminate the growth by closing the oxygen leak valve. NEVER close the Eu shutter first.

15. Wait 10 minutes for the residual oxygen in the chamber to pump down. The Eu shutter should still be open, but despite the high flux rate, the Eu material is simply re-evaporating off the surface or depositing a little bit of EuO due to oxidation with the residual O_2.

16. Close the Eu shutter and turn the Eu cell back to base temperature ($T_{Eu} \sim 220$ °C).

17. Cool sample to RT and take final RHEED patterns along EuO(001) [100] // MgO(001) [110] and EuO(001) [110] // MgO(001) [100]. The EuO layer will be rotated 45 ° in-plane with respect to the underlying MgO substrate.

18. The sample can be capped at RT by e-beam MgO or Al. 2 – 5 nm is sufficient. A double cap of MgO covered with Al is more effective.

10.4.4 EuO/HOPG(0001)

Recipe

1. Warm up Eu cell to growth temperature to allow it to degas a bit during pump time.

Optional: Keep Eu cell at mid-range growth rate (2 Å/min) overnight for better degas.

2. Prepare fresh HOPG substrate. HOPG(0001) substrate is grade ZYA from SPI.

3. Place HOPG substrate on a clean flat surface and apply 3M scotch tape uniformly pressed over the HOPG substrate surface. Gently rub with your thumb over the tape surface to press the tape to the substrate. Use soft carbon tweezers for extra rubbing to fill any additional crevasses.

4. Peel the tape off the substrate to reveal a clean HOPG surface. *Note: Repeat steps 3 and 4 at least once more to be sure of a clean surface*

5. Mount with Ta foil on corners to Thermoinics sample platen (pocket).

6. Load into load-lock and pump down.

7. While pumping, take Eu rate. Move manipulator into deposition monitor position ($x > 1.9$). Wheel in deposition monitor. Eu rate should be between 8 and 9 Å/min. Pay close attention to the chamber pressure due to the Eu cell. When done, remove deposition monitor and put manipulator back into transfer position.

8. Transfer sample into main chamber and examine the HOPG RHEED pattern. There is no need to examine different directions as HOPG has in-plane rotational disorder (see section 7.2, figure 7.2 a)).

9. Anneal in UHV at 600 °C for 1 hour.

10. Cool to $T_S = 550$ °C ($T_M \sim 670$ °C) and allow temperature to stabilize. Temperature stabilization is certain once T_M is constant.

11. Open the Eu shutter. The incoming Eu flux will re-evaporate off the sample surface (see Sec. 7.2) and the RHEED pattern will remain unaltered. Monitor the chamber pressure

carefully.

Upon opening the Eu shutter, the pressure will artificially spike due to Eu back heating. After the 5 minute wait time, the Eu vapor pressure, which is the dominant contributor to the current total chamber pressure, should have returned to close to the normal value (the pressure during at which the rate was taken with the deposition monitor).

12. Wait minimum 5 minutes for steady state of the Eu flux.

13. Leak molecular oxygen such that the partial pressure is P$_{O_2}$ = 1 – 1.2×10^{-8} Torr above the chamber background pressure. Do NOT exceed this value.

14. Grow for the desired amount of time. At this Eu rate and oxygen pressure, EuO will deposit at a rate of $\sim$ 1.67 nm/min (or 5 nm per 30 minutes).

15. Terminate the growth by closing the oxygen leak valve. NEVER close the Eu shutter first.

16. Wait 10 minutes for the residual oxygen in the chamber to pump down. The Eu shutter should still be open, but despite the high flux rate, the Eu material is simply re-evaporating off the surface or depositing a little bit of EuO due to oxidation with the residual O_2.

17. Close the Eu shutter and turn the Eu cell back to base temperature (T$_{Eu}$ $\sim$ 220 °C).

18. Cool sample to RT and take final RHEED pattern (see section 7.2, figure 7.2 b)).

19. The sample can be capped at RT by e-beam MgO or Al. 2 – 5 nm is sufficient. A double cap of MgO covered with Al is more effective.

10.5 Co/Pd Superstructures for Perpendicular Media

Very thin Co and Pd repeated layers (superlattices) are known to demonstrate perpendicular magnetic anisotropy (PMA) [395, 396, 397, 398, 26]. Magnetic anisotropy simply refers to a preferred orientation of magnetization along different axis directions in a solid. For instance, if a system has a preferred orientation along one axis in the solid, that will be the configuration that minimizes the magnetic energy and is called the 'easy' axis. In the case of thin films, there are a wide variety of growth and materials parameters that allow for significant control over the magnetic anisotropy [138], and is therefore crucial for commercial applications. Some important applications include interlayer exchange coupling (IEC) [399, 400, 401, 402, 403, 138], spin transfer torque (STT) [404, 405, 406], giant magnetoresistance (GMR) [1, 2, 399] tunneling magnetoresistance (TMR) [5, 6, 27], and magneto-optic (MO) [407] recording. There are several types of sources for anisotropy in a magnetic system. They are due to the shape of material (shape anisotropy), the internal electric fields combined with spin-orbit coupling (magneto-crystalline anisotropy), and mechanical deformation like strain or stress (strain anisotropy), and symmetry-breaking at the interface (surface anisotropy). Like all interface effects, it is extremely sensitive to the the atomic scale structure, and therefore can be easily controlled and optimized for the desired application through MBE.

The relevant energy for surface anisotropy along the film normal is given by [397, 398, 138],

$$E_A = K_V \cos^2\theta \times d + K_S \cos^2\theta \tag{10.1}$$

where E_A is the surface anisotropy energy in units of erg/cm^{-2}, d is the thickness of the magnetic thin film, K_S is the interface or surface anisotropy term, θ is the angle between the axis and the magnetization, and K_V is the volume anisotropy term in units of erg/cm^{-3}. K_V is given by,

$$K_V = K_{shape} + K_{M-C} + K_{strain} \tag{10.2}$$

where K_{shape}, K_{M-C}, and K_{strain} are the shape, magneto-crystalline, and strain anisotropy terms. The shape anisotropy is caused by energy dependence along different directions from the boundary conditions of the dipolar field resulting from the magnetization. On the other hand, the spin-orbit interaction is responsible for magneto-crystalline anisotropy and strain anisotropy. For thick films we can ignore K_S and the easy direction can be determined by the magnitude and signs of the different bulk anisotropy terms. For the perpendicular axis chosen, $K_V > 0$ (< 0) corresponds to a preference for in-plane (out-of-plane) orientation of the magnetization. Generally, for thin films, the magneto-crystalline anisotropy is dominated by the shape anisotropy. Thus, along the perpendicular axis, $K_{shape} > 0$ and films typically have magnetizations in-plane. However, within the plane of the film, the magneto-crystalline anisotropy will be relevant as in the case of Fe films on 2x4 reconstructed GaAs(001) [389, 48, 390].

We can now add K_S back into consideration. Regardless of the origin of K_S, we can understand why PMA appears in very thin films through equation 10.1. First, it is necessary that the surface term K_S favors the perpendicular direction (i.e. $K_S < 0$). Second, there is a competition between K_S and K_V to determine the lowest energy axis. As the film thickness decreases, a crossover can occur where $\mid K_V \times d \mid < \mid K_S \mid$. Therefore, the surface anisotropy term dominates. This will orient the easy axis along the out-of-plane axis.

A comprehensive review of PMA in a variety of structures including Co, Fe, and Ni with various interlayers (Pt, Pd, Au, Cu, etc..) is presented in [398]. Perpendicular magnetic anisotropy was first discovered in (Co/Pd)$_n$ superlattices in 1985 [395] for structures with many repeats ($n \sim 100$) of thin Co (4 – 12 Å) and Pd ($\sim$ 33 – 80 Å) bilayers. The microscopic nature of PMA is considered to have several contributions to the surface anisotropy term [Johnson]:

$$K_S = K_N + K_{coh} + K_{inc} \tag{10.3}$$

where K_N is the Néel surface anisotropy [408], K_{coh} is the surface strain anisotropy, and K_{inc} is the incoherent anisotropy term. K_N arises due to particular orientations at the surface of the internal electric fields and spin-orbit coupling. This is essentially a surface modified version of the bulk magneto-crystalline anisotropy due to the lowering of symmetry [408]. Similarly, the magneto-elastic (strain/stress) contribution to the bulk value K_{strain} can also be significantly altered at the interface and produce a surface anisotropy. K_{coh} is the *coherent* part of the magneto-elastic surface anisotropy and appears for systems in which the lattice mismatch is not too large, which allows for the layers to grow in a regime in which the magnetic layer experiences epitaxial tensile strain [397, 398]. On the other hand, when the lattice constants differ significantly (as is the case for Co/Pd), the layers will not grow strained, but can be characterized as epitaxial but with many dislocations. This is called *incoherent* and gives rise to the surface anisotropy term K_{inc}. Much of the behavior of the [(Co,Fe,Ni)/X]$_n$ bilayer superlattices, where X is a non-magnetic (usually a transition metal) element, can be reasonably explained with this model. The magneto-crystalline component to the surface anisotropy can be directly calculated, while the coherent and incoherent terms require some experimental input for the amount of strain induced through different growth techniques (i.e. sputter vs. MBE).

Interestingly, Co/Pd does not fall into the set of material systems that are easily explained through this model. It was shown by [409] that K_S is independent of the crystalline orientations of the Co/Pd bilayers, suggesting that the main source of anisotropy stems from K_{inc}. However, it has also been seen that K_S can be enhanced through annealing, which is associated with film smoothing [397]. This and other results would suggest a meaningful contribution from K_N [398, 410]. These issues were exacerbated by the difficulty in properly characterizing the structural quality for each group and each K_S experiment. At the time, advanced materials characterization techniques (RHEED) and magnetization measurements (SQUID) were less ubiquitous. In general the detailed microscopic origin of K_S is complex and depends strongly on the substrate, crystallinity, materials choice, roughness, and interdiffusion. Recent experiments provide new insights including the importance of local anisotropy, grain structure, d-d orbital hybridization leading to enhanced orbital contributions, and induced magnetism in the adjacent Pd layers [411, 412]. Fortunately, regardless of the complex origin of K_S, (Co/Pd)$_n$ provides a robust, orientation independent, system to taking advantage of room temperature perpendicular magnetization for spintronics applications.

We are interested in taking advantage of perpendicular anisotropy for perpendicular spin injection into GaAs. The goal of this project is to inject spins electrically and then detect them via slow muons as discussed in ref. [413]. In plane spin injection is not possible as the muons are sensitive to spin polarization oriented along the surface normal to the substrate. Also, the muon detection signal is increased by having large substrates with injected spin carriers over a large region (1.5 cm x 1.5 cm) and therefore large substrates are desired. For this, we have used 7×10^{16} /cm-2 n-GaAs(001) that we buy in 2 inch wafers. As shown in figure 10.4, these AXT substrates provide acceptable spin properties for our purposes here.

AXT GaAs(001) substrates are prepared by a wet chemical digital etch. Prepare 30% H_2O_2 and a DI rinse beaker for the peroxide step. The peroxide serves to oxidize the surface. Next, prepare a beaker of HCL:H_2O (1:1) and a DI rinse beaker for the acid step as well. The hydrochloric acid etches the oxide. Using teflon tweezers dip the sample in the peroxide for 1 minute, then dip into the DI rinse for the peroxide step for 15 – 30 s. Blow dry with N_2 gas. Next, dip the sample into the HCL solution for 1 minute, and then into the DI rinse for the acid step for 15 – 30 s. Blow dry with N_2 gas and then repeat the process. This oxidize/etch procedure should be repeated three times, thus the term digital. The digital etch

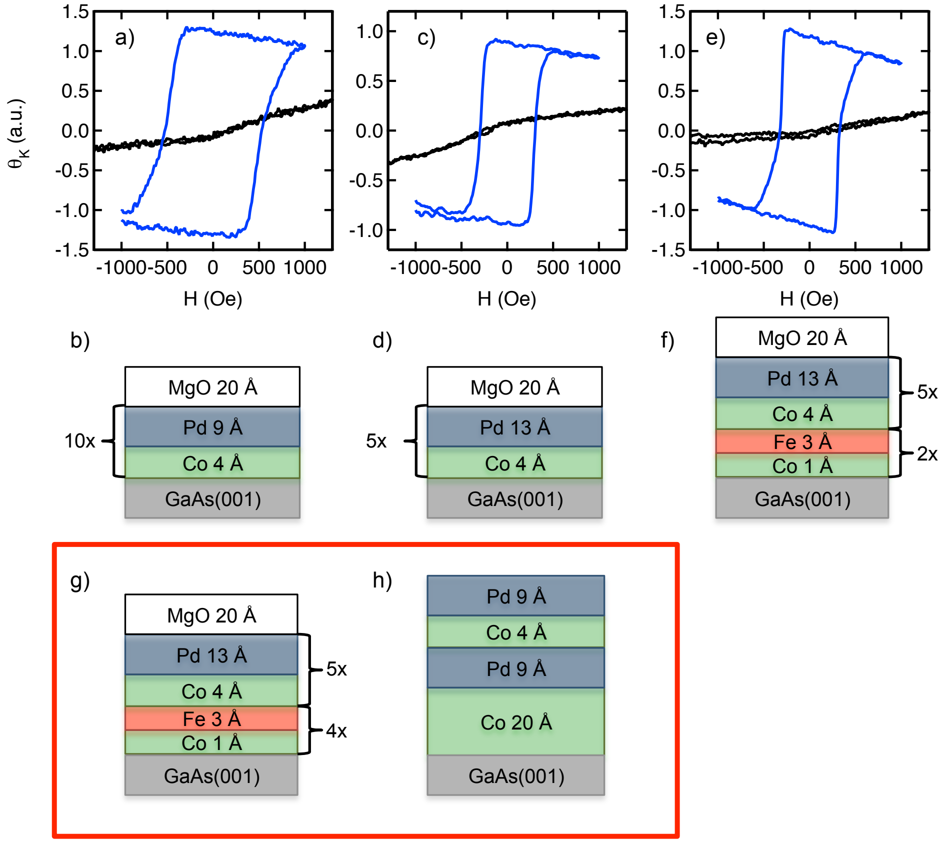

Figure 10.8: Comparison of Magnetic Behavior of Different Co/Pd Superlattices. a) Polar (blue curve) and longitudinal (black curve) MOKE plotted in arbitrary units. The data in a) corresponds to the structure shown in figure b). c) Polar (blue curve) and longitudinal (black curve) MOKE corresponding to the structure shown in figure d). e) Polar (blue curve) and longitudinal (black curve) MOKE corresponding to the structure shown in figure f). g) and h) The structures in the red box show structures that did not demonstrate PMA.

seems to produce better results than a single long peroxide and etch recipe. The sample is then annealed in UHV at 580 °C for 30 minutes.

Next, we investigate the Co/Pd growth and determine which bilayer repeats give PMA and the coercivity range we are looking for ($H_C < 500$ Oe). Fig. 10.8 shows the magnetic hysteresis loops as measured by polar MOKE at RT for several different Co/Pd superlattices. The hysteresis loop in fig. 10.8 a) (blue curve), which corresponds to the structure drawn in

10.8 b) with 4 ÅCo and 9 ÅPd repeated 10 times, demonstrates PMA with H_C = 520 Oe. A longitudinal MOKE scan (black curve) does not show any saturation in this field range indicating that the in-plane direction is a magnetically hard axis. The Co/Pd superlattice with 4 ÅCO and 13 ÅPd repeated 5 times, also demonstrated PMA with H_C = 300 Oe. Notably, the PMA (blue curves) demonstrated by these two structures shows high magnetic remanence (M_R = M_S), which is crucial for the upcoming muon experiments, which will seek to determine if there is spin injection at zero applied field. The diamagnetic background is likely due to the Pd layers.

For spin injection purposes, we are also concerned about the spin diffusion length in the spin injecting material. We do not wish to have Co/Pd bilayers directly at the interface as there is no spin polarization in the Pd layers which is expected to lead to lower spin injection efficiency. Therefore wee seek to have fully magnetic layers at the interface and the total thickness of these layers should approach the spin diffusion length in metals. For this, we would like to have at least 1 nm of magnetic material at the interface. We first investigate the now standard Co/Pd (4 Å/ 13 Å) 5 repeat structure with an additional Co/Fe (1 Å/3 Å) double bilayer at the interface as shown in fig. 10.8 f). The polar magnetic hysteresis loops for this structure is shown in 10.8 e) and is characterized by M_R = M_S, H_C = 320 Oe, and a slight twisting in the loop shape leading to an increase in the saturation field, H_S. This increase in M_S is directly related to relative increase in the volume anisotropy energy compared to the surface term due to the Co/Fe layers which do not contribute a significant contribution to the surface anisotropy term. However, the change in H_S is not large, and the magnetic hysteresis loops still show excellent properties. We have also investigated increasing the amount of magnetic material at the interface by adding extra Co/Fe bilayers at the interface to create a total structure [Co(4 Å)/Pd(13 Å)]$_5$/[Co(1 Å)/Fe(3 Å)]$_4$ as shown in figure 10.8 g). And we also investigate a thick Co buffer layer at the interface underneath the standard Co/Pd structure (Fig. 10.8). These structures did not demonstrate perpendicular magnetization. Therefore, we have determined that the structure presented in figure 10.8 f) gives the best compromise of coercivity, saturation magnetization, and spin diffusion length, without compromising the magnetic remanence.

For the purposes of spin injection, it may also be desirable to improve the spin injection efficiency by adding an MgO tunnel barrier. We next investigate the magnetic properties of Co/Pd layers with the interfacial Co/Fe double bilayer on MgO grown on GaAs. The GaAs substrate is prepared as before with the peroxide/HCL digital etch. In order to protect the edges of the sample from edge deposition and therefore create electric shorts between the interface and the back of the sample, we employ a Ta foil mask system that protects all sides of the sample, but leaves the majority of the sample face open for materials growth. Also, the Ta foil mask is compatible with the GaAs substrate UHV anneal. 1.5 nm of e-beam MgO is deposited on the GaAs substrate at RT. Following this, the Co/Fe double bilayer and Co/Pd superstructure is grown on top. Next, a wedge shutter is wheeled in front of the sample to block one small $\sim \frac{1}{4}$ inch $\times$ $\frac{1}{4}$ inch of the sample. Next 50 nm Pd is grown on top to act as a top electrical contact. The remaining $\sim \frac{1}{4}$ inch $\times$ $\frac{1}{4}$ inch area of total metal thickness $\sim$ 12 nm, is thin enough to allow for MOKE characterization. Lastly, the sample is flipped

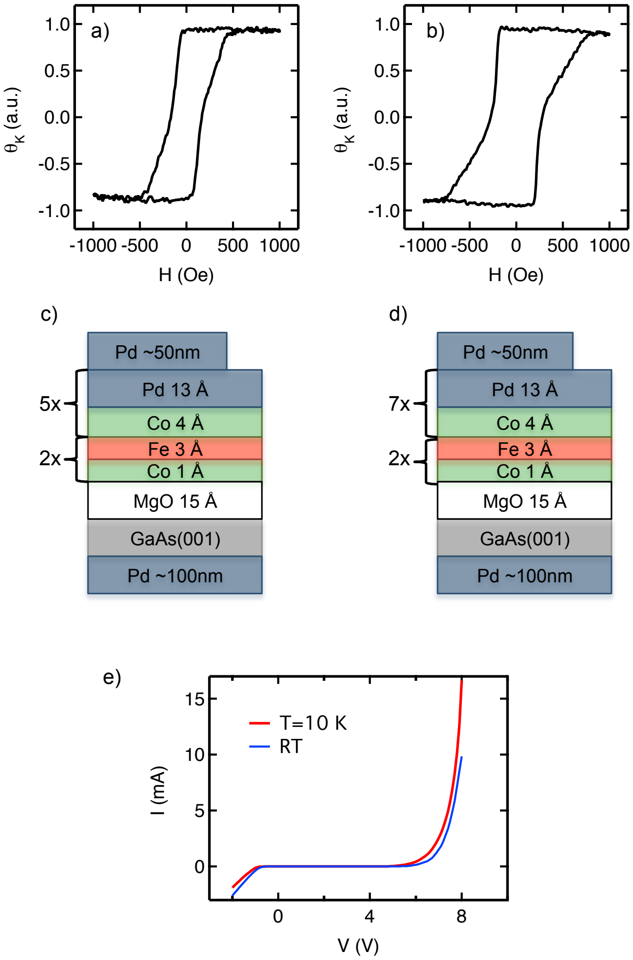

Figure 10.9: $[\mathrm{Co/Pd}]_n/[\mathrm{Co/Fe}]_m$ layers on MgO/GaAs(001) Characterization. a) Polar MOKE for 5 times repeated Co/Pd structure as shown in c) for growth on MgO (1.5 nm)/GaAs(001). b) Polar MOKE for 7 times repeated Co/Pd structure as shown in d) for growth on MgO (1.5 nm)/GaAs(001). e) DC I-V for these sample structures with a 50 nm Pd cap on top of the Co/Pd superstructure and 100 nm Pd layer grown on the unpolished back-side of the sample with forward bias applied relative to the $[\mathrm{Co/Pd/}]_n/[\mathrm{Co/Fe}]_m$/MgO/GaAs(001) interface.

over, carefully mounted so as to not scratch the front surface, and Ta foil masked off on the edges. It is then loaded back into the UHV growth chamber for 100 nm Pd contact grown on the back of the substrate. A sample of $[\mathrm{Co(4\ Å)/Pd(13\ Å)}]_5/[\mathrm{Co(1\ Å)/Fe(3\ Å)}]_4$/MgO (1.5 nm)/GaAs(001) is characterized by polar MOKE as shown in Fig. 10.9 a). The MOKE data demonstrates that the PMA behavior has changed compared to growth in the absence of the MgO barrier. On MgO, the sample shows a much lower coercivity of H_C = 170 Oe. H_S = 500 Oe and noticeably, the magnetization switching is apparent close to zero field. This makes for an undesirable situation as the robustness of our mandatory condition, $M_R = M_S$, is on the cusp of not being met. Therefore, we can increase the low field magnetization stability and increase the difference in anisotropy between in-plane and out-of-plane, thus increasing the necessary field to switch the magnetization, by adding two extra bilayers of Co/Pd and create the structure $[Co(4\ Å)/Pd(13\ Å)]_7/[Co(1\ Å)/Fe(3\ Å)]_4$/MgO (1.5 nm)/GaAs(001) as shown in figure 10.9 d). The sample is grown with identical preparation, Ta masking, and Pd electrodes. Figure 10.9 b) shows the polar MOKE measurement which demonstrates increased stability at low field, increased coercivity (H_C = 270 Oe), and increased saturation field (H_S = 790 Oe). These magnetization characteristics meets the requirements that we are looking for. Next we can measure DC I-V on this sample structure. Fig. 10.9 e) shows I-V curve at RT and T=10K. Positive voltage corresponds to forward bias of the PMA interface.

In conclusion, we have investigated $(Co/Pd)_n/(Co/Fe)_m$ structures as a means for realizing perpendicular magnetic media for future projects that will investigate spin properties in n-GaAs via decay of spin-polarized slow muons. The magnetic properties were optimized for structures with and without an MgO barrier in order to maximize the remanence ($M_R = M_S$) and place the coercivity and saturation field in a moderate range that is accessible by reasonably low magnetic fields of $\sim$ 1000 Oe. The I-V curves demonstrate relatively temperature independent operation.

Bibliography

[1] M. N. Baibich, J. M. Broto, A. Fert, F. N. Van Dau, F. Petroff, P. Etienne, G. Creuzet, A. Friederich, and J. Chazelas, Physical Review Letters **61**, 2472 (1988).

[2] G. Binasch, P. Grünberg, F. Saurenbach, W. Zinn, et al., Physical Review B **39**, 4828 (1989).

[3] M. Julliere, Physics Letters A **54**, 225 (1975).

[4] P. M. Tedrow and R. Meservey, Physical Review Letters **26**, 192 (1971).

[5] S. S. P. Parkin, C. Kaiser, A. Panchula, P. M. Rice, B. Hughes, M. Samant, and S. H. Yang, Nature Materials **3**, 862 (2004).

[6] S. Yuasa, T. Nagahama, A. Fukushima, Y. Suzuki, and K. Ando, Nature Materials **3**, 868 (2004).

[7] A. Fert, Reviews of Modern Physics **80**, 1517 (2008).

[8] R. J. Epstein, F. M. Mendoza, Y. K. Kato, and D. D. Awschalom, Nature Physics **1**, 94 (2005).

[9] R. Hanson and D. D. Awschalom, Nature **453**, 1043 (2008).

[10] B. B. Buckley, G. D. Fuchs, L. C. Bassett, and D. D. Awschalom, Science **330**, 1212 (2010).

[11] S. A. Crooker, J. Brandt, C. Sandfort, A. Greilich, D. R. Yakovlev, D. Reuter, A. D. Wieck, and M. Bayer, Physical Review Letters **104**, 36601 (2010).

[12] A. J. Ramsay, Semiconductor Science and Technology **25**, 103001 (2010).

[13] Y. Li, N. Sinitsyn, D. L. Smith, D. Reuter, A. D. Wieck, D. R. Yakovlev, M. Bayer, and S. A. Crooker, Physical Review Letters **108**, 186603 (2012).

[14] M. W. Wu, J. H. Jiang, and M. Q. Weng, Physics Reports **493**, 61 (2010).

[15] S. A. Wolf, D. D. Awschalom, R. A. Buhrman, J. M. Daughton, S. von Molnar, M. L. Roukes, A. Y. Chtchelkanova, and D. M. Treger, Science **294**, 1488 (2001).

[16] I. Žutić, J. Fabian, and S. D. Sarma, Reviews of Modern Physics **76**, 323 (2004).

[17] S. A. Wolf, A. Y. Chtchelkanova, and D. M. Treger, IBM Journal of Research and Development **50**, 101 (2006).

[18] C. Felser, G. H. Fecher, and B. Balke, Angewandte Chemie International Edition **46**, 668 (2007).

[19] D. D. Awschalom and M. E. Flatté, Nature Physics **3**, 153 (2007).

[20] J. Fabian, A. Matos-Abiague, C. Ertler, P. Stano, and I. Zutic, Acta Phys. Slovaca **57**, 565 (2007).

[21] M. Bibes and A. Barthelemy, IEEE Transactions on Electronic Devices **54**, 1003 (2007).

[22] S. D. Bader and S. S. P. Parkin, Annu. Rev. Condens. Matter Phys. **1**, 71 (2010).

[23] M. Bibes, J. E. Villegas, and A. Barthelemy, Advances in Physics **60**, 5 (2011).

[24] S. Sanvito, Chemical Society Reviews **40**, 3336 (2011).

[25] W. Han, K. M. McCreary, K. Pi, W. H. Wang, Y. Li, H. Wen, J. R. Chen, and R. K. Kawakami, Journal of Magnetism and Magnetic Materials **324**, 369 (2012).

[26] J. Stöhr and H. C. Siegmann, *Magnetism: from fundamentals to nanoscale dynamics*, vol. 15 (Springer Heidelberg, 2006).

[27] S. Yuasa, A. Fukushima, H. Kubota, Y. Suzuki, and K. Ando, Applied Physics Letters **89**, 042505 (2006).

[28] S. Datta and B. Das, Applied Physics Letters **56**, 665 (1990).

[29] M. Johnson and R. H. Silsbee, Physical Review Letters **55**, 1790 (1985).

[30] F. J. Jedema, H. B. Heersche, A. T. Filip, J. J. Baselmans, B. J. van Wees, et al., Nature **416**, 713 (2002).

[31] S. Takahashi and S. Maekawa, Physical Review B **67**, 052409 (2003).

[32] N. Tombros, C. Jozsa, M. Popinciuc, H. T. Jonkman, and B. J. van Wees, Nature **448**, 571 (2007).

[33] K. M. McCreary, Ph.D. thesis, University of California, Riverside (2012).

[34] W. Han, Ph.D. thesis, University of California, Riverside (2012).

[35] Y. Fukuma, L. Wang, H. Idzuchi, S. Takahashi, S. Maekawa, and Y. Otani, Nature Materials **10**, 527 (2011).

[36] H. Idzuchi, Y. Fukuma, L. Wang, and Y. Otani, Applied Physics Letters **101**, 022415 (2012).

[37] F. J. Jedema, A. T. Filip, and B. J. Van Wees, Nature **410**, 345 (2001).

[38] Y. K. Takahashi, S. Kasai, S. Hirayama, S. Mitani, and K. Hono, Applied Physics Letters **100**, 052405 (2012).

[39] P. Laczkowski, L. Vila, V.-D. Nguyen, A. Marty, J.-P. Attané, H. Jaffrès, J.-M. George, and A. Fert, Physical Review B **85**, 220404 (2012).

[40] Y. Niimi, D. Wei, H. Idzuchi, T. Wakamura, T. Kato, and Y. Otani, Physical Review Letters **110**, 016805 (2013).

[41] K. S. Novoselov, A. K. Geim, S. V. Morozov, D. Jiang, Y. Zhang, S. V. Dubonos, I. V. Grigorieva, and A. A. Firsov, Science **306**, 666 (2004).

[42] A. K. Geim and K. S. Novoselov, Nature Materials **6**, 183 (2007).

[43] A. H. Castro Neto, F. Guinea, N. M. R. Peres, K. S. Novoselov, and A. K. Geim, Reviews of Modern Physics **81**, 109 (2009).

[44] K. S. Novoselov, A. K. Geim, S. V. Morozov, D. Jiang, M. I. Katsnelson, I. V. Grigorieva, S. V. Dubonos, and A. A. Firsov, Nature **438**, 197 (2005).

[45] Y. Zhang, Y.-W. Tan, H. L. Stormer, and P. Kim, Nature **438**, 201 (2005).

[46] E. J. H. Lee, K. Balasubramanian, R. T. Weitz, M. Burghard, and K. Kern, Nature Nanotechnology **3**, 486 (2008).

[47] A. K. Geim, Reviews of Modern Physics **83**, 851 (2011).

[48] X. Li, W. Cai, J. An, S. Kim, J. Nah, D. Yang, R. Piner, A. Velamakanni, I. Jung, E. Tutuc, et al., Science **324**, 1312 (2009).

[49] S. Bae, H. Kim, Y. Lee, X. Xu, J.-S. Park, Y. Zheng, J. Balakrishnan, T. Lei, H. R. Kim, Y. I. Song, et al., Nature Nanotechnology **5**, 574 (2010).

[50] Y. W. Tan, Y. Zhang, K. Bolotin, Y. Zhao, S. Adam, E. H. Hwang, S. D. Sarma, H. L. Stormer, and P. Kim, Physical Review Letters **99**, 246803 (2007).

[51] K. Pi, K. M. McCreary, W. Bao, W. Han, Y. F. Chiang, Y. Li, S.-W. Tsai, C. N. Lau, and R. K. Kawakami, Physical Review B **80**, 075406 (2009).

[52] K. I. Bolotin, F. Ghahari, M. D. Shulman, H. L. Stormer, and P. Kim, Nature **462**, 196 (2009).

[53] X. Du, I. Skachko, A. Barker, and E. Y. Andrei, Nature Nanotechnology **3**, 491 (2008).

[54] K. I. Bolotin, K. J. Sikes, Z. Jiang, M. Klima, G. Fudenberg, J. Hone, P. Kim, and H. L. Stormer, Solid State Communications **146**, 351 (2008).

[55] C. R. Dean, A. F. Young, I. Meric, C. Lee, L. Wang, S. Sorgenfrei, K. Watanabe, T. Taniguchi, P. Kim, K. L. Shepard, et al., Nature Nanotechnology **5**, 722 (2010).

[56] A. S. Mayorov, R. V. Gorbachev, S. V. Morozov, L. Britnell, R. Jalil, L. A. Ponomarenko, P. Blake, K. S. Novoselov, K. Watanabe, T. Taniguchi, et al., Nano Letters **11**, 2396 (2011).

[57] X. Du, I. Skachko, F. Duerr, A. Luican, and E. Y. Andrei, Nature **462**, 192 (2009).

[58] M. I. Katsnelson, K. S. Novoselov, and A. K. Geim, Nature Physics **2**, 620 (2006).

[59] A. F. Young and P. Kim, Nature Physics **5**, 222 (2009).

[60] N. Stander, B. Huard, and D. Goldhaber-Gordon, Physical Review Letters **102**, 26807 (2009).

[61] D. Huertas-Hernando, F. Guinea, and A. Brataas, Physical Review B **74**, 155426 (2006).

[62] H. Min, J. E. Hill, N. A. Sinitsyn, B. R. Sahu, L. Kleinman, and A. H. MacDonald, Physical Review B **74**, 165310 (2006).

[63] Y. Yao, F. Ye, X. L. Qi, S. C. Zhang, and Z. Fang, Physical Review B **75**, 041401(R) (2007).

[64] S. Chen, Q. Wu, C. Mishra, J. Kang, H. Zhang, K. Cho, W. Cai, A. A. Balandin, and R. S. Ruoff, Nature Materials (2012).

[65] E. W. Hill, A. K. Geim, K. S. Novoselov, F. Schedin, and P. Blake, IEEE Transactions on Magnetics **42**, 2694 (2006).

[66] M. Nishioka and A. Goldman, Applied Physics Letters **90**, 252505 (2007).

[67] W. H. Wang, K. Pi, Y. Li, Y. F. Chiang, P. Wei, J. Shi, and R. K. Kawakami, Physical Review B **77**, 020402 (2008).

[68] S. Cho, Y.-F. Chen, and M. S. Fuhrer, Applied Physics Letters **91**, 123105 (2007).

[69] M. Popinciuc, C. Jozsa, P. J. Zomer, A. Veligura, H. T. Jonkman, and B. J. van Wees, Physical Review B **80**, 214427 (2009).

[70] C. Józsa, T. Maassen, M. Popinciuc, P. J. Zomer, A. Veligura, H. T. Jonkman, and B. J. van Wees, Physical Review B **80**, 241403(R) (2009).

[71] W. Han, K. Pi, K. M. McCreary, Y. Li, J. J. I. Wong, A. G. Swartz, and R. K. Kawakami, Physical Review Letters **105**, 167202 (2010).

[72] W. Han and R. K. Kawakami, Physical Review Letters **107**, 047207 (2011).

[73] S. Jo, D. K. Ki, D. Jeong, H. J. Lee, and S. Kettermann, Physical Review B **84**, 075453 (2011).

[74] W. Han, W. H. Wang, K. Pi, K. M. McCreary, W. Bao, Y. Li, F. Miao, C. N. Lau, and R. K. Kawakami, Physical Review Letters **102**, 137205 (2009).

[75] T.-Y. Yang, J. Balakrishnan, F. Volmer, A. Avsar, M. Jaiswal, J. Samm, S. R. Ali, A. Pachoud, M. Zeng, M. Popinciuc, et al., Physical Review Letters **107**, 047206 (2011).

[76] T. Maassen, F. K. Dejene, M. H. D. Guimarães, C. Józsa, and B. J. van Wees, Physical Review B **83**, 115410 (2011).

[77] B. Dlubak, M. B. Martin, C. Deranlot, B. Servet, S. Xavier, R. Mattana, M. Sprinkle, C. Berger, W. A. D. Heer, D. Petroff, et al., Nature Physics **8**, 557 (2012).

[78] T. Maassen, J. J. van den Berg, N. IJbema, F. Fromm, T. Seyller, R. Yakimova, and B. J. van Wees, Nano Letters **12**, 1498 (2012).

[79] T. Maassen, J. J. van den Berg, E. H. Huisman, H. Dijkstra, F. Fromm, T. Seyller, and B. J. van Wees, Physical Review Letters **110**, 067209 (2013).

[80] M. H. D. Guimarães, A. Veligura, P. J. Zomer, T. Maassen, I. J. Vera-Marun, N. Tombros, and B. J. van Wees, Nano Letters **12**, 3512 (2012).

[81] I. Neumann, J. Van de Vondel, G. Bridoux, M. V. Costache, F. Alzina, C. M. S. Torres, and S. O. Valenzuela, Small **9**, 156 (2013).

[82] P. J. Zomer, M. H. D. Guimarães, N. Tombros, and B. J. van Wees, arXiv preprint arXiv:1209.1999 (2012).

[83] C. Ertler, S. Konschuh, M. Gmitra, and J. Fabian, Physical Review B **80**, 041405(R) (2009).

[84] F. Ochoa, A. H. Castro Neto, and F. Guinea, Physical Review Letters **108**, 206808 (2012).

[85] A. H. Castro Neto and F. Guinea, Physical Review Letters **103**, 026804 (2009).

[86] P. Zhang and M. W. Wu, Physical Review B **84**, 045304 (2011).

[87] D. Huertas-Hernando, F. Guinea, and A. Brataas, Eur. Phys. J. Spec. Top. **148**, 177 (2007).

[88] D. Huertas-Hernando, F. Guinea, and A. Brataas, Physical Review Letters **103**, 146801 (2009).

[89] P. Zhang and M. W. Wu, New Journal of Physics **14**, 033015 (2012).

[90] R. J. Elliott, Physical Review **96**, 266 (1954).

[91] Y. Yafet, Solid State Physics **14**, 1 (1963).

[92] M. I. D'yakonov and V. I. Perel, Sov. Phys. Solid State **13**, 3023 (1971).

[93] C. Weeks, J. Hu, J. Alicea, M. Franz, and R. Wu, Physical Review X **1**, 021001 (2011).

[94] K. M. McCreary, K. Pi, and R. K. Kawakami, Applied Physics Letters **98**, 192101 (2011).

[95] T. Maassen, I. J. Vera-Marun, M. H. D. Guimarães, and B. J. van Wees, Physical Review B **86**, 235408 (2012).

[96] S. P. Dash, S. Sharma, J. C. L. Breton, J. Peiro, H. Jaffrès, J.-M. George, A. Lemaître, and R. Jansen, Physical Review B **84**, 054410 (2011).

[97] W. Han, J.-R. Chen, D. Wang, K. M. McCreary, H. Wen, A. G. Swartz, J. Shi, and R. K. Kawakami, Nano Letters **12**, 3443 (2012).

[98] Y. Ohno, D. K. Young, B. a. Beschoten, F. Matsukura, H. Ohno, and D. D. Awschalom, Nature **402**, 790 (1999).

[99] R. Fiederling, M. Keim, G. Reuscher, W. Ossau, G. Schmidt, A. Waag, and L. W. Molenkamp, Nature **402**, 787 (1999).

[100] Y. K. Kato, R. C. Myers, A. C. Gossard, and D. D. Awschalom, Science **306**, 1910 (2004).

[101] S. A. Crooker, M. Furis, X. Lou, C. Adelmann, D. L. Smith, C. J. Palmstrøm, and P. A. Crowell, Science **309**, 2191 (2005).

[102] X. Lou, C. Adelmann, S. A. Crooker, E. S. Garlid, J. Zhang, K. S. M. Reddy, S. D. Flexner, C. J. Palmstrøm, and P. A. Crowell, Nature Physics **3**, 197 (2007).

[103] J. M. Kikkawa and D. D. Awschalom, Physical Review Letters **80**, 4313 (1998).

[104] F. Meier and B. P. Zakharchenya, *Optical orientation* (North-Holland Amsterdam, 1984).

[105] R. K. Kawakami, Y. Kato, M. Hanson, I. Malajovich, J. M. Stephens, E. Johnston-Halperin, G. Salis, A. C. Gossard, and D. D. Awschalom, Science **294**, 131 (2001).

[106] P. Kotissek, M. Bailleul, M. Sperl, A. Spitzer, D. Schuh, W. Wegscheider, C. H. Back, and G. Bayreuther, Nature Physics **3**, 872 (2007).

[107] H. Dery and L. J. Sham, Physical Review Letters **98**, 46602 (2007).

[108] H. J. Zhu, M. Ramsteiner, H. Kostial, M. Wassermeier, H.-P. Schönherr, and K. H. Ploog, Physical Review Letters **87**, 16601 (2001).

[109] H. C. Koo, J. H. Kwon, J. Eom, J. Chang, S. H. Han, and M. Johnson, Science **325**, 1515 (2009).

[110] A. Ohtomo and H. Y. Hwang, Nature **427**, 423 (2004).

[111] N. Reyren, M. Bibes, E. Lesne, J.-M. George, C. Deranlot, S. Collin, A. Barthélémy, and H. Jaffrès, Physical Review Letters **108**, 186802 (2012).

[112] J. Mannhart and D. G. Schlom, Science **327**, 1607 (2010).

[113] H. Y. Hwang, Y. Iwasa, M. Kawasaki, B. Keimer, N. Nagaosa, and Y. Tokura, Nature Materials **11**, 103 (2012).

[114] A. D. Caviglia, S. Gariglio, N. Reyren, D. Jaccard, T. Schneider, M. Gabay, S. Thiel, G. Hammerl, J. Mannhart, and J.-M. Triscone, Nature **456**, 624 (2008).

[115] N. Reyren, S. Thiel, A. D. Caviglia, L. F. Kourkoutis, G. Hammerl, C. Richter, C. W. Schneider, T. Kopp, A.-S. Rüetschi, D. Jaccard, et al., Science **317**, 1196 (2007).

[116] C. Bell, S. Harashima, Y. Kozuka, M. Kim, B. G. Kim, Y. Hikita, and H. Y. Hwang, Physical Review Letters **103**, 226802 (2009).

[117] M. Ben Shalom, M. Sachs, D. Rakhmilevitch, A. Palevski, and Y. Dagan, Physical Review Letters **104**, 126802 (2010).

[118] A. D. Caviglia, M. Gabay, S. Gariglio, N. Reyren, C. Cancellieri, and J.-M. Triscone, Physical Review Letters **104**, 126803 (2010).

[119] J. A. Bert, B. Kalisky, C. Bell, M. Kim, Y. Hikita, H. Y. Hwang, and K. A. Moler, Nature Physics **7**, 767 (2011).

[120] A. Tsukazaki, A. Ohtomo, T. Kita, Y. Ohno, H. Ohno, and M. Kawasaki, Science **315**, 1388 (2007).

[121] Y. Kozuka, M. Kim, H. Ohta, Y. Hikita, C. Bell, and H. Y. Hwang, Applied Physics Letters **97**, 222115 (2010).

[122] B. Jalan, S. Stemmer, S. Mack, and S. J. Allen, Physical Review B **82**, 081103 (2010).

[123] C. Sahin, G. Vignale, and M. E. Flatte, To Be Submitted (2013).

[124] J. Lee, N. Sai, and A. A. Demkov, Physical Review B **82**, 235305 (2010).

[125] Y. Wang, M. K. Niranjan, J. D. Burton, J. M. An, K. D. Belashchenko, and E. Y. Tsymbal, Physical Review B **79**, 212408 (2009).

[126] J. R. Arthur, Surface Science **500**, 189 (2002).

[127] M. A. Herman and H. Sitter, *Molecular beam epitaxy: fundamentals and current status* (Springer-Verlag Berlin, 1989).

[128] A. Y. Cho, Journal of Crystal Growth **111**, 1 (1991).

[129] A. Y. Cho, Journal of Crystal Growth **201–202**, 1 (1999).

[130] E. F. Schubert, Journal of Vacuum Science & Technology A: Vacuum, Surfaces, and Films **8**, 2980 (1990).

[131] E. F. Schubert, *Doping in III-V semiconductors* (Cambridge, UK: Cambridge University Press, 1993).

[132] N. L. Stormer, Reviews of Modern Physics **71**, 875 (1999).

[133] W. P. McCray, Nature Nanotechnology **2**, 259 (2007).

[134] D. C. Tsui, H. L. Stormer, and A. C. Gossard, Physical Review Letters **48**, 1559 (1982).

[135] M. F. Crommie, C. P. Lutz, D. M. Eigler, et al., Science **262**, 218 (1993).

[136] D. G. Schlom, J. H. Haeni, J. Lettieri, C. D. Theis, W. Tian, J. C. Jiang, and X. Q. Pan, Materials Science and Engineering: B **87**, 282 (2001).

[137] D. G. Schlom and C. H. Ahn, Nature **456**, 582 (2008).

[138] J. J. I. Wong, Ph.D. thesis, University of California, Riverside (2012).

[139] W. Braun, *Applied RHEED: reflection high-energy electron diffraction during crystal growth*, vol. 154 (Springer Verlag, 1999).

[140] C. C. Chang, Surface Science **25**, 53 (1971).

[141] F. Schedin, A. K. Geim, S. V. Morozov, E. W. Hill, P. Blake, M. I. Katsnelson, and K. S. Novoselov, Nature Materials **6**, 652 (2007).

[142] X. Dong, D. Fu, W. Fang, Y. Shi, P. Chen, and L. J. Li, Small **5**, 1422 (2009).

[143] X. Wang, X. Li, L. Zhang, Y. Yoon, P. K. Weber, H. Wang, J. Guo, and H. Dai, Science **324**, 768 (2009).

[144] K. M. McCreary, K. Pi, A. G. Swartz, W. Han, W. Bao, C. N. Lau, F. Guinea, M. I. Katsnelson, and R. K. Kawakami, Physical Review B **81**, 115453 (2010).

[145] D. B. Farmer, R. Golizadeh-Mojarad, V. Perebeinos, Y. M. Lin, G. S. Tulevski, J. C. Tsang, and P. Avouris, Nano Letters **9**, 388 (2008).

[146] Y. H. Lu, W. Chen, Y. P. Feng, and P. M. He, The Journal of Physical Chemistry B **113**, 2 (2008).

[147] J. Choi, H. Lee, K. Kim, B. Kim, and S. Kim, The Journal of Physical Chemistry Letters **1**, 505 (2009).

[148] G. Giovannetti, P. A. Khomyakov, G. Brocks, V. M. Karpan, J. Van den Brink, and P. J. Kelly, Physical Review Letters **101**, 26803 (2008).

[149] Z. Ni, Y. Wang, T. Yu, and Z. Shen, Nano Research **1**, 273 (2008).

[150] K. Zou, X. Hong, D. Keefer, and J. Zhu, Physical Review Letters **105**, 126601 (2010).

[151] L. A. Ponomarenko, R. Yang, T. M. Mohiuddin, M. I. Katsnelson, K. S. Novoselov, S. V. Morozov, A. A. Zhukov, F. Schedin, E. W. Hill, and A. K. Geim, Physical Review Letters **102**, 206603 (2009).

[152] J. Martin, N. Akerman, G. Ulbricht, T. Lohmann, J. H. Smet, K. Von Klitzing, and A. Yacoby, Nature Physics **4**, 144 (2007).

[153] Y. Zhang, V. W. Brar, C. Girit, A. Zettl, and M. F. Crommie, Nature Physics **5**, 722 (2009).

[154] A. Deshpande, W. Bao, F. Miao, C. N. Lau, and B. J. LeRoy, Physical Review B **79**, 205411 (2009).

[155] F. Xia, T. Mueller, R. Golizadeh-Mojarad, M. Freitag, Y. Lin, J. Tsang, V. Perebeinos, and P. Avouris, Nano Letters **9**, 1039 (2009).

[156] T. Mueller, F. Xia, M. Freitag, J. Tsang, and P. Avouris, Physical Review B **79**, 245430 (2009).

[157] J. Park, Y. H. Ahn, and C. Ruiz-Vargas, Nano Letters **9**, 1742 (2009).

[158] J. H. Chen, C. Jang, S. Adam, M. S. Fuhrer, E. D. Williams, and M. Ishigami, Nature Physics **4**, 377 (2008).

[159] S. Adam, E. H. Hwang, V. M. Galitski, and S. D. Sarma, PNAS **104**, 18392 (2007).

[160] E. H. Hwang, S. Adam, and S. Das Sarma, Physical Review Letters **98**, 186806 (2007).

[161] J.-H. Chen, W. G. Cullen, C. Jang, M. S. Fuhrer, and E. D. Williams, Physical Review Letters **102**, 236805 (2009).

[162] D. C. Elias, R. R. Nair, T. M. G. Mohiuddin, S. V. Morozov, P. Blake, M. P. Halsall, A. C. Ferrari, D. W. Boukhvalov, M. I. Katsnelson, A. K. Geim, et al., Science **323**, 610 (2009).

[163] Z. H. Ni, L. A. Ponomarenko, R. R. Nair, R. Yang, S. Anissimova, I. V. Grigorieva, F. Schedin, P. Blake, Z. X. Shen, E. H. Hill, et al., Nano Letters **10**, 3868 (2010).

[164] M. Wojtaszek, N. Tombros, A. Caretta, P. H. M. van Loosdrecht, and B. J. van Wees, Journal of Applied Physics **110**, 063715 (2011).

[165] X. Hong, S.-H. Cheng, C. Herding, and J. Zhu, Physical Review B **83**, 085410 (2011).

[166] F. Withers, M. Dubois, and A. K. Savchenko, Physical Review B **82** (2010).

[167] J. Moser, H. Tao, S. Roche, F. Alzina, C. M. S. Torres, and A. Bachtold, Physical Review B **81**, 205445 (2010).

[168] I. Childres, L. A. Jauregui, J. Tian, and Y. P. Chen, New Journal of Physics **13**, 025008 (2011).

[169] K. Pi, Ph.D. thesis, University of California, Riverside (2010).

[170] M. I. Katsnelson, F. Guinea, and A. K. Geim, Physical Review B **79**, 195426 (2009).

[171] K. Pi, W. Han, K. M. McCreary, A. G. Swartz, Y. Li, and R. K. Kawakami, Physical Review Letters **104**, 187201 (2010).

[172] B. T. Matthias, R. M. Bozorth, and J. H. Van Vleck, Physical Review Letters **7**, 160 (1961).

[173] J. H. Van Vleck, Journal of Applied Physics **39**, 365 (1968).

[174] A. Mauger and C. Godart, Physics Reports **141**, 51 (1986).

[175] F. Cardarelli, ed., *Materials Handbook: a concise desktop reference* (Springer-Verlag, London, 2008), 2nd ed.

[176] K. Y. Ahn and M. W. Shafer, Journal of Applied Physics **41**, 1260 (1970).

[177] M. R. Oliver, J. O. Dimmock, A. L. McWhorter, and T. B. Reed, Physical Review B **5**, 1078 (1972).

[178] Y. Shapira, S. Foner, and T. B. Reed, Physical Review B **8**, 2299 (1973).

[179] A. Schmehl, V. Vaithyanathan, A. Herrnberger, S. Thiel, C. Richter, M. Liberati, T. Heeg, M. Rockerath, L. F. Kourkoutis, S. Muhlbauer, et al., Nature Materials **6**, 882 (2007).

[180] T. Yamasaki, K. Ueno, A. Tsukazaki, T. Fukumura, and M. Kawasaki, Applied Physics Letters **98**, 082116 (2011).

[181] P. G. Steeneken, Ph.D. thesis, University of Groningen (2002).

[182] Y. Hajati, M. Zargar Shoushtari, and G. Rashedi, Journal of Applied Physics **112**, 013901 (2012).

[183] Y. Asano, T. Yoshida, Y. Tanaka, and A. A. Golubov, Physical Review B **78**, 014514 (2008).

[184] L. Dell'Anna and A. De Martino, Physical Review B **80**, 155416 (2009).

[185] L. Dell'Anna and A. De Martino, Physical Review B **79**, 045420 (2009).

[186] L. Dell'Anna and A. De Martino, Physical Review B **83**, 155449 (2011).

[187] E. Faizabadi, M. Esmaeilzadeh, and F. Sattari, The European Physical Journal B-Condensed Matter and Complex Systems **85**, 1 (2012).

[188] S. Grover, S. Ghosh, and M. Sharma, Modelling and Simulation in Materials Science and Engineering **20**, 045010 (2012).

[189] Y. Gu, Y. H. Yang, J. Wang, and K. S. Chan, Journal of Applied Physics **105**, 103711 (2009).

[190] H. Haugen, D. Huertas-Hernando, and A. Brataas, Physical Review B **77**, 115406 (2008).

[191] N. V. Hung, A. Bournel, P. Dollfus, and N. Van Lien, in *Journal of Physics: Conference Series* (IOP Publishing, 2009), vol. 187, p. 012037.

[192] Y. F. Hsu and G. Y. Guo, Physical Review B **81**, 045412 (2010).

[193] M. Khodas, I. A. Zaliznyak, and D. E. Kharzeev, Physical Review B **80**, 125428 (2009).

[194] Y. X. Li, The European Physical Journal B-Condensed Matter and Complex Systems **68**, 119 (2009).

[195] W. Liewrian, R. Hoonsawat, I. Tang, et al., Physica E: Low-dimensional Systems and Nanostructures **42**, 1287 (2010).

[196] W. Liewrian, I. Tang, R. Hoonsawat, et al., Physica E: Low-dimensional Systems and Nanostructures **44**, 327 (2011).

[197] J. Linder, A. M. Black-Schaffer, and A. Sudbø, Physical Review B **82**, 041409 (2010).

[198] J. F. Liu and K. S. Chan, Nanotechnology **22**, 395201 (2011).

[199] P. Michetti, P. Recher, and G. Iannaccone, Nano Letters **10**, 4463 (2010).

[200] P. Michetti and P. Recher, Physical Review B **84**, 125438 (2011).

[201] A. G. Moghaddam and M. Zareyan, Solid State Communications **149**, 1106 (2009).

[202] F. M. Mojarabian and G. Rashedi, Physica E: Low-dimensional Systems and Nanostructures (2011).

[203] N. Myoung and G. Ihm, Journal of Applied Physics **109**, 053716 (2011).

[204] V. H. Nguyen, A. Bournel, and P. Dollfus, Journal of Applied Physics **109**, 073717 (2011).

[205] Z. P. Niu, F. X. Li, B. G. Wang, L. Sheng, and D. Y. Xing, The European Physical Journal B-Condensed Matter and Complex Systems **66**, 245 (2008).

[206] Z. P. Niu, Journal of Physics: Condensed Matter **23**, 435302 (2011).

[207] Z. Qiao, S. A. Yang, W. Feng, W. K. Tse, J. Ding, Y. Yao, J. Wang, and Q. Niu, Physical Review B **82**, 161414 (2010).

[208] Z. Qiao, H. Jiang, X. Li, Y. Yao, and Q. Niu, Physical Review B **85**, 115439 (2012).

[209] M. Salehi, M. Alidoust, and G. Rashedi, Journal of Applied Physics **108** (2010).

[210] Y. G. Semenov, K. W. Kim, and J. M. Zavada, Applied Physics Letters **91**, 153105 (2007).

[211] Y. G. Semenov, J. M. Zavada, and K. W. Kim, Journal of Applied Physics **107**, 064507 (2010).

[212] Y. G. Semenov, J. M. Zavada, and K. W. Kim, Physical Review B **77**, 235415 (2008).

[213] Y. G. Semenov, J. M. Zavada, and K. W. Kim, Physical Review Letters **101**, 147206 (2008).

[214] M. Sharma and S. Ghosh, Journal of Physics: Condensed Matter **23**, 055501 (2011).

[215] B. Soodchomshom, I. Tang, R. Hoonsawat, et al., Physica C: Superconductivity **469**, 689 (2009).

[216] B. Soodchomshom, I. Tang, R. Hoonsawat, et al., Physica E: Low-dimensional Systems and Nanostructures **41**, 1310 (2009).

[217] B. Soodchomshom, I. Tang, R. Hoonsawat, et al., Physica C: Superconductivity **470**, 31 (2010).

[218] B. Soodchomshom, I. Tang, R. Hoonsawat, et al., Physics Letters A **372**, 5054 (2008).

[219] Q. Sun, Z. Jiang, Y. Yu, and X. C. Xie, Physical Review B **84**, 214501 (2011).

[220] Q. Sun and X. C. Xie, Physical Review Letters **104**, 66805 (2010).

[221] H. Y. Tian, Y. H. Yang, and J. Wang, The European Physical Journal B-Condensed Matter and Complex Systems **85**, 1 (2012).

[222] W. K. Tse, Z. Qiao, Y. Yao, A. H. MacDonald, and Q. Niu, Physical Review B **83**, 155447 (2011).

[223] Q. P. Wu, X. D. He, and Z. F. Liu, The European Physical Journal B-Condensed Matter and Complex Systems **85**, 1 (2012).

[224] Q. P. Wu, X. D. He, and Z. F. Liu, Physica E: Low-dimensional Systems and Nanostructures (2011).

[225] L. I. Xiao-Wei, Chinese Physics Letters **28**, 047401 (2011).

[226] Y. L. Yang, C. Bai, and X. D. Zhang, The European Physical Journal B-Condensed Matter and Complex Systems **72**, 217 (2009).

[227] H. X. Yang, A. Hallal, D. Terrade, X. Waintal, S. Roche, and M. Chshiev, Phys. Rev. Lett. **110**, 046603 (2013).

[228] T. Yokoyama, Physical Review B **77**, 073413 (2008).

[229] T. Yokoyama and J. Linder, Physical Review B **83**, 081418 (2011).

[230] Y. Yu, Q. Liang, and J. Dong, Physics Letters A **375**, 2858 (2011).

[231] F. Zhai and L. Yang, Applied Physics Letters **98**, 062101 (2011).

[232] Q. Zhang, K. S. Chan, and Z. Lin, Applied Physics Letters **98**, 032106 (2011).

[233] Q. Zhang, J. F. Liu, Z. Lin, and K. S. Chan, Journal of Applied Physics **112**, 073701 (2012).

[234] Q. Zhang, Z. Lin, and K. S. Chan, Journal of Physics: Condensed Matter **24**, 075302 (2012).

[235] Z. Y. Zhang, Journal of Physics: Condensed Matter **21**, 095302 (2009).

[236] Q. Zhang, D. Fu, B. Wang, R. Zhang, and D. Y. Xing, Physical Review Letters **101**, 47005 (2008).

[237] J. Zou and G. Jin, EPL (Europhysics Letters) **87**, 27008 (2009).

[238] J. Zou, G. Jin, and Y. Ma, Journal of Physics: Condensed Matter **21**, 126001 (2009).

[239] B. Zhou, X. Chen, H. Wang, K. H. Ding, and G. Zhou, Journal of Physics: Condensed Matter **22**, 445302 (2010).

[240] R. W. Ulbricht, A. Schmehl, T. Heeg, J. Schubert, and D. G. Schlom, Applied Physics Letters **93**, 102105 (2008).

[241] R. Sutarto, S. G. Altendorf, B. Coloru, M. Moretti Sala, T. Haupricht, C. F. Chang, Z. Hu, C. Schüßler-Langeheine, N. Hollmann, H. Kierspel, et al., Physical Review B **79**, 205318 (2009).

[242] A. G. Swartz, J. Ciraldo, J. J. I. Wong, Y. Li, W. Han, T. Lin, S. Mack, J. Shi, D. D. Awschalom, and R. K. Kawakami, Applied Physics Letters **97**, 112509 (2010).

[243] A. G. Swartz, J. J. I. Wong, I. V. Pinchuk, and R. K. Kawakami, Journal of Applied Physics **111**, 083912 (2012).

[244] A. G. Swartz, P. M. Odenthal, Y. Hao, R. S. Ruoff, and R. K. Kawakami, ACS Nano **6**, 10063 (2012).

[245] K. Momma and F. Izumi, J. Appl. Crystallogr. **41**, 653 (2008).

[246] T. Kasuya, Journal of Applied Physics **41**, 1090 (1970).

[247] C. E. Moore, *Atomic Energy Levels* (National Bureau of Standards Circular, 1958), no. 467 ed.

[248] L. Pauling, *The Nature of the Chemical Bond* (Cornell University Press, Ithaca, N.Y., 1960).

[249] G. Güntherodt, P. Wachter, and D. M. Imboden, Zeitschrift für Physik B Condensed Matter **12**, 292 (1971).

[250] N. J. C. Ingle and I. S. Elfimov, Physical Review B **77**, 121202 (2008).

[251] T. S. Santos, J. S. Moodera, K. V. Raman, E. Negusse, J. Holroyd, J. Dvorak, M. Liberati, Y. U. Idzerda, and E. Arenholz, Physical Review Letters **101**, 147201 (2008).

[252] M. J. Freiser, S. Holtzberg Methfessel, G. D. Petit, M. W. Shafer, and J. C. Suits, Helv. Phys. Acta **41**, 832 (1969).

[253] P. A. M. Dirac, *The Principles of Quantum Mechanics* (Clarendon, Oxford, 1947), 3rd ed.

[254] W. Heisenberg, Zeitschrift für Physik A Hadrons and Nuclei **49**, 619 (1928).

[255] N. W. Ashcroft and N. D. Mermin, *Solid State Physics* (Thomas Learning, Inc., 1976).

[256] C. Zener, Physical Review **81**, 440 (1951).

[257] O. W. Dietrich, A. J. Henderson, and H. Meyer, Physical Review B **12**, 2844 (1975).

[258] T. Kasuya, IBM Journal of Research and Development **14**, 214 (1970).

[259] O. W. Dietrich, J. Als-Nielsen, and L. Passell, Physical Review B **14**, 4923 (1976).

[260] W. Nolting, G. Borstel, and W. Borgiel, Physical Review B **35**, 7015 (1987).

[261] W. Liu, G. Hong, D. Dai, L. Li, and M. Dolg, Theoretical Chemistry Accounts: Theory, Computation, and Modeling (Theoretica Chimica Acta) **96**, 75 (1997).

[262] R. Schiller, W. Müller, and W. Nolting, Physical Review B **64**, 134409 (2001).

[263] R. Schiller and W. Nolting, Physical Review Letters **86**, 3847 (2001).

[264] R. Schiller and W. Nolting, Solid State Communications **118**, 173 (2001).

[265] J. Kunes, W. Ku, and W. E. Pickett, Journal of the Physical Society of Japan **74**, 1408 (2005).

[266] W. Söllinger, W. Heiss, R. T. Lechner, K. Rumpf, P. Granitzer, H. Krenn, and G. Springholz, Physical Review B **81**, 155213 (2010).

[267] X. Wan, J. Dong, and S. Y. Savrasov, Physical Review B **83**, 205201 (2011).

[268] H. Wang, C. Schuster, and U. Schwingenschlögl, Chemical Physics Letters **524**, 68 (2012).

[269] P. G. Steeneken, L. H. Tjeng, I. Elfimov, G. A. Sawatzky, G. Ghiringhelli, N. B. Brookes, and D. J. Huang, Physical Review Letters **88**, 47201 (2002).

[270] H. Miyazaki, T. Ito, H. J. Im, S. Yagi, M. Kato, K. Soda, and S. Kimura, Physical Review Letters **102**, 227203 (2009).

[271] P. Liu, J. A. C. Santana, Q. Dai, X. Wang, P. A. Dowben, and J. Tang, Physical Review B **86**, 224408 (2012).

[272] N. M. Souza-Neto, D. Haskel, Y. C. Tseng, and G. Lapertot, Physical Review Letters **102**, 57206 (2009).

[273] P. Liu and J. Tang, Physical Review B **85**, 224417 (2012).

[274] H. Miyazaki, H. J. Im, K. Terashima, S. Yagi, M. Kato, K. Soda, T. Ito, and S. Kimura, Applied Physics Letters **96**, 232503 (2010).

[275] S. G. Altendorf, A. Efimenko, V. Oliana, H. Kierspel, A. D. Rata, and L. H. Tjeng, Physical Review B **84**, 155442 (2011).

[276] S. G. Altendorf, N. Hollmann, R. Sutarto, C. Caspers, R. C. Wicks, Y. Y. Chin, Z. Hu, H. Kierspel, I. S. Elfimov, H. H. Hsieh, et al., Physical Review B **85**, 081201 (2012).

[277] T. Mairoser, A. Schmehl, A. Melville, T. Heeg, W. Zander, J. Schubert, D. E. Shai, E. J. Monkman, K. M. Shen, T. Z. Regier, et al., Applied Physics Letters **98**, 102110 (2011).

[278] T. Mairoser, A. Schmehl, A. Melville, T. Heeg, L. Canella, P. Böni, W. Zander, J. Schubert, D. E. Shai, E. J. Monkman, et al., Physical Review Letters **105**, 257206 (2010).

[279] M. Arnold and J. Kroha, Physical Review Letters **100**, 46404 (2008).

[280] P. Liu, J. Tang, J. A. Colón Santana, K. D. Belashchenko, and P. A. Dowben, Journal of Applied Physics **109**, 07C311 (2011).

[281] A. Melville, T. Mairoser, A. Schmehl, D. E. Shai, E. Monkman, J. W. Harter, T. Heeg, B. Hollander, J. Schubert, K. M. Shen, et al., Applied Physics Letters **100**, 222101 (2012).

[282] K. Y. Ahn, Applied Physics Letters **17**, 347 (1970).

[283] M. Muller, G. X. Miao, and J. S. Moodera, Journal of Applied Physics **105**, 07C917 (2009).

[284] E. Negusse, J. Dvorak, J. S. Holroyd, M. Liberati, T. S. Santos, J. S. Moodera, E. Arenholz, and Y. U. Idzerda, Journal of Applied Physics **105**, 07C930 (2009).

[285] M. Barbagallo, T. Stollenwerk, J. Kroha, N. J. Steinke, N. D. M. Hine, J. F. K. Cooper, C. H. W. Barnes, A. Ionescu, P. Monteiro, J. Y. Kim, et al., Physical Review B **84**, 075219 (2011).

[286] D. F. Forster, J. Klinkhammer, C. Busse, S. G. Altendorf, T. Michely, Z. Hu, Y. Y. Chin, L. H. Tjeng, J. Coraux, and D. Bourgault, Physical Review B **83**, 045424 (2011).

[287] G. V. Samsanov, ed., *The Oxide Handbook* (IFI/Plenum, New York, 1985), 2nd ed.

[288] N. Iwata, G. Pindoria, T. Morishita, and K. Kohn, Journal of the Physical Society of Japan **69**, 230 (2000).

[289] J. J. I. Wong, L. Ramirez, A. G. Swartz, A. Hoff, W. Han, Y. Li, and R. K. Kawakami, Physical Review B **81**, 094406 (2010).

[290] S. Wang, Y. Zhang, N. Abidi, and L. Cabrales, Langmuir **25**, 11078 (2009).

[291] M. Fiebig, Journal of Physics D: Applied Physics **38**, R123 (2005).

[292] T. Maruyama, Y. Shiota, T. Nozaki, K. Ohta, N. Toda, M. Mizuguchi, A. Tulapurkar, T. Shinjo, M. Shiraishi, S. Mizukami, et al., Nature Nanotechnology **4**, 158 (2009).

[293] M. Weisheit, S. Fähler, A. Marty, Y. Souche, C. Poinsignon, and D. Givord, Science **315**, 349 (2007).

[294] X. He, Y. Wang, N. Wu, A. N. Caruso, E. Vescovo, K. D. Belashchenko, P. A. Dowben, and C. Binek, Nature Materials **9**, 579 (2010).

[295] V. Garcia, M. Bibes, L. Bocher, S. Valencia, F. Kronast, A. Crassous, X. Moya, S. Enouz-Vedrenne, A. Gloter, D. Imhoff, et al., Science **327**, 1106 (2010).

[296] S. Valencia, A. Crassous, L. Bocher, V. Garcia, X. Moya, R. Cherifi, C. Deranlot, K. Bouzehouane, S. Fusil, A. Zobelli, et al., Nature Materials **10**, 753 (2011).

[297] J. J. I. Wong, A. G. Swartz, R. Zheng, W. Han, and R. K. Kawakami, Physical Review B **86**, 060409 (2012).

[298] P. M. Tedrow, J. E. Tkaczyk, and A. Kumar, Physical Review Letters **56**, 1746 (1986).

[299] S. Y. Huang, X. Fan, D. Qu, Y. P. Chen, W. G. Wang, J. Wu, T. Y. Chen, J. Q. Xiao, and C. L. Chien, Physical Review Letters **109**, 107204 (2012).

[300] T. Stehlin, M. Feller, P. Guyot-Sionnest, and Y.-R. Shen, Optics letters **13**, 389 (1988).

[301] Y. Fan, H. B. Zhao, G. Lüpke, A. T. Hanbicki, C. H. Li, and B. T. Jonker, Physical Review B **85**, 165311 (2012).

[302] R. J. Epstein, I. Malajovich, R. K. Kawakami, Y. Chye, M. Hanson, P. M. Petroff, A. C. Gossard, and D. D. Awschalom, Physical Review B **65**, 121202 (2002).

[303] Y. Li, Y. Chye, Y. F. Chiang, K. Pi, W. H. Wang, J. M. Stephens, S. Mack, D. D. Awschalom, and R. K. Kawakami, Physical Review Letters **100**, 237205 (2008).

[304] N. Nakagawa, H. Y. Hwang, and D. A. Muller, Nature Materials **5**, 204 (2006).

[305] M. Basletic, J.-L. Maurice, C. Carrétéro, G. Herranz, O. Copie, M. Bibes, É. Jacquet, K. Bouzehouane, S. Fusil, and A. Barthélémy, Nature Materials **7**, 621 (2008).

[306] S. S. A. Seo, Z. Marton, W. S. Choi, G. W. J. Hassink, D. H. A. Blank, H. Y. Hwang, T. W. Noh, T. Egami, and H. N. Lee, Applied Physics Letters **95**, 082107 (2009).

[307] A. Tsukazaki, S. Akasaka, K. Nakahara, Y. Ohno, H. Ohno, D. Maryenko, A. Ohtomo, and M. Kawasaki, Nature Materials **9**, 889 (2010).

[308] Q. Song, K. H. Chow, M. Egilmez, I. Fan, M. D. Hossain, R. F. Kiefl, S. R. Kreitzman, C. D. P. Levy, G. D. Morris, T. J. Parolin, et al., Physica B: Condensed Matter **404**, 619 (2009).

[309] O. V. Yazyev, Reports on Progress in Physics **73**, 056501 (2010).

[310] A. C. Ferrari, J. C. Meyer, V. Scardaci, C. Casiraghi, M. Lazzeri, F. Mauri, S. Piscanec, D. Jiang, K. S. Novoselov, S. Roth, et al., Physical Review Letters **97**, 187401 (2006).

[311] V. M. Pereira, F. Guinea, J. M. B. Lopes dos Santos, N. M. R. Peres, and A. H. Castro Neto, Physical Review Letters **96**, 36801 (2006).

[312] W.-M. Huang, J.-M. Tang, and H.-H. Lin, Physical Review B **80**, 121404 (2009).

[313] E. J. Duplock, M. Scheffler, and P. J. D. Lindan, Physical Review Letters **92**, 225502 (2004).

[314] P. O. Lehtinen, A. S. Foster, Y. Ma, A. V. Krasheninnikov, and R. M. Nieminen, Physical Review Letters **93**, 187202 (2004).

[315] O. V. Yazyev and L. Helm, Physical Review B **75**, 125408 (2007).

[316] D. W. Boukhvalov, M. I. Katsnelson, and A. I. Lichtenstein, Physical Review B **77**, 035427 (2008).

[317] M. A. H. Vozmediano, M. P. López-Sancho, T. Stauber, and F. Guinea, Physical Review B **72**, 155121 (2005).

[318] H. Kumazaki and D. Hirashima, Journal of Magnetism and Magnetic Materials **310**, 2256 (2007).

[319] J. J. Palacios, J. Fernández-Rossier, and L. Brey, Physical Review B **77**, 195428 (2008).

[320] B. Uchoa, V. N. Kotov, N. M. R. Peres, and A. H. Castro Neto, Physical Review Letters **101**, 026805 (2008).

[321] E. H. Lieb, Physical Review Letters **62**, 1201 (1989).

[322] L. Pisani, J. A. Chan, B. Montanari, and N. M. Harrison, Physical Review B **75**, 064418 (2007).

[323] O. V. Yazyev and M. I. Katsnelson, Physical Review Letters **100**, 047209 (2008).

[324] P. Esquinazi, D. Spemann, R. Hohne, A. Setzer, K.-H. Han, and T. Butz, Physical Review Letters **91**, 227201 (2003).

[325] L. Xie, X. Wang, J. Lu, Z. H. Ni, Z. Luo, H. Mao, R. Wang, Y. Wang, H. Huang, D. Qi, et al., Applied Physics Letters **98**, 193113 (2011).

[326] J. Cervenka, M. I. Katsnelson, and C. F. J. Flipse, Nature Physics **5**, 840 (2009).

[327] H. S. S. Ramakrishna Matte, K. S. Subrahmanyam, and C. N. R. Rao, Journal of Physical Chemistry C **113**, 9982 (2009).

[328] Y. Wang, Y. Huang, Y. Song, X. Zhang, Y. Ma, J. Liang, and Y. Chen, Nano Letters **9**, 220 (2009).

[329] M. Sepioni, R. R. Nair, S. Rablen, J. Narayanan, F. Tuna, R. Winpenny, A. K. Geim, and I. V. Grigorieva, Physical Review Letters **105**, 207205 (2010).

[330] R. R. Nair, M. Sepioni, I.-L. Tsai, O. Lehtinen, J. Keinonen, A. V. Krasheninnikov, T. Thomson, A. K. Geim, and I. V. Grigorieva, Nature Physics **8**, 199 (2012).

[331] R. R. Nair, I. Tsai, M. Sepioni, O. Lehtinen, J. Keinonen, A. V. Krasheninnikov, A. H. Castro Neto, A. K. Geim, I. V. Grigorieva, et al., arXiv preprint arXiv:1301.7611 (2013).

[332] A. Candini, C. Alvino, W. Wernsdorfer, and M. Affronte, Physical Review B **83**, 121401 (2011).

[333] J.-H. Chen, L. Li, W. G. Cullen, E. D. Williams, and M. S. Fuhrer, Nature Physics **7**, 535 (2011).

[334] J. Jobst and H. B. Weber, Nature Physics **8**, 352 (2012).

[335] H. Ott, S. J. Heise, R. Sutarto, Z. Hu, C. F. Chang, H. H. Hsieh, H.-J. Lin, C. T. Chen, and L. H. Tjeng, Physical Review B **73**, 094407 (2006).

[336] J. Lettieri, V. Vaithyanathan, S. K. Eah, J. Stephens, V. Sih, D. D. Awschalom, J. Levy, and D. G. Schlom, Applied Physics Letters **83**, 975 (2003).

[337] A. Fujimori, M. Grioni, and J. H. Weaver, Physical Review B **33**, 726 (1986).

[338] K. J. Hubbard and D. G. Schlom, Journal of Materials Research **11**, 2757 (1996).

[339] C. M. Boubeta, J. L. Menendez, J. L. Costa-Kramer, J. M. Garcia, J. V. Anguita, B. Bescos, A. Cebollada, F. Briones, A. V. Chernykh, I. V. Malikov, et al., Surface Science **482–485, Part 2**, 910 (2001).

[340] J. W. Reiner, A. M. Kolpak, Y. Segal, K. F. Garrity, S. Ismail-Beigi, C. H. Ahn, and F. J. Walker, Advanced Materials **22**, 2919 (2010).

[341] S. Yadavalli, M. H. Yang, and C. P. Flynn, Physical Review B **41**, 7961 (1990).

[342] W. Han, Y. Zhou, Y. Wang, Y. Li, J. J. I. Wong, K. Pi, A. G. Swartz, K. M. McCreary, F. Xiu, K. L. Wang, et al., Journal of Crystal Growth **312**, 44 (2009).

[343] X. Jiang, R. Wang, R. M. Shelby, R. M. Macfarlane, S. R. Bank, J. S. Harris, and S. S. P. Parkin, Physical Review Letters **94**, 056601 (2005).

[344] T. Sasaki, T. Oikawa, T. Suzuki, M. Shiraishi, Y. Suzuki, and K. Tagami, Applied Physics Express **2**, 053003 (2009).

[345] Y. Zhou, W. Han, L.-T. Chang, F. Xiu, M. Wang, M. Oehme, I. A. Fischer, J. Schulze, R. K. Kawakami, and K. L. Wang, Physical Review B **84**, 125323 (2011).

[346] R. A. McKee, F. J. Walker, E. D. Specht, G. E. Jellisen, and L. A. Boatner, Physical Review Letters **72**, 2741 (1994).

[347] D. M. Lind, S. D. Berry, G. Chern, H. Mathias, and L. R. Testardi, Physical Review B **45**, 1838 (1992).

[348] R. D. Shannon, Acta Crystallogr., Sect. A: Cryst. Phys. Diff., Theor. Gen. Crystallogr. **32**, 751 (1976).

[349] H. Kawanowa, D. Mori, Y. Gotohand, and R. Souda, Surf. Interface Anal. **36**, 1001 (2004).

[350] R. Rausch and W. Nolting, Journal of Physics: Condensed Matter **21**, 376002 (2009).

[351] J. Zou, G. Jin, and Y.-Q. Ma, Journal of Physics: Condensed Matter **21**, 126001 (2009).

[352] V. E. Henrich and P. A. Cox, *The surface science of metal oxides* (Cambridge university press, 1996).

[353] Y. Hao, Y. Wang, L. Wang, Z. Ni, Z. Wang, R. Wang, C. K. Koo, Z. Shen, and J. T. L. Thong, Small **6**, 195 (2009).

[354] A. Gupta, G. Chen, P. Joshi, S. Tadigadapa, and Eklund, Nano Letters **6**, 2667 (2006).

[355] L. M. Malard, M. A. Pimenta, G. Dresselhaus, and M. S. Dresselhaus, Physics Reports **473**, 51 (2009).

[356] B. Tang, H. Guoxin, and H. Gao, Applied Spectroscopy Reviews **45**, 369 (2010).

[357] S. Pisana, M. Lazzeri, C. Casiraghi, K. S. Novoselov, A. K. Geim, A. C. Ferrari, and F. Mauri, Nature Materials **6**, 198 (2007).

[358] A. Das, S. Pisana, B. Chakraborty, S. Piscanec, S. K. Saha, U. V. Waghmare, K. S. Novoselov, H. R. Krishnamurthy, A. K. Geim, A. K. Sood, et al., Nature Nanotechnology **3**, 210 (2008).

[359] Z. H. Ni, H. M. Wang, Y. Ma, J. Kasim, Y. H. Wu, and Z. X. Shen, ACS Nano **2**, 1033 (2008).

[360] Z. H. Ni, T. Yu, Y. H. Lu, Y. Y. Wang, Y. P. Feng, and Z. X. Shen, ACS Nano **2**, 2301 (2008).

[361] F. Ding, H. Ji, Y. Chen, A. Herklotz, K. Dörr, Y. Mei, A. Rastelli, and O. G. Schmidt, Nano Letters **10**, 3453 (2010).

[362] Z. Cheng, Q. Zhou, C. Wang, Q. Li, C. Wang, and Y. Fang, Nano Letters **11**, 767 (2011).

[363] J. Zhou, Q. Wang, Q. Sun, X. S. Chen, Y. Kawazoe, and P. Jena, Nano Letters **9**, 3867 (2009).

[364] D. Soriano, N. Leconte, P. Ordejon, J.-C. Charlier, J.-J. Palacios, and S. Roche, Physical Review Letters **107**, 016602 (2011).

[365] H. Lee, Y.-W. Son, N. Park, S. Han, and J. Yu, Physical Review B **72**, 174431 (2005).

[366] M. M. Ugeda, I. Brihuega, F. Guinea, and J. M. Gomez-Rodriguez, Physical Review Letters **104**, 096804 (2010).

[367] C. Tao, L. Jiao, O. V. Yazyev, Y.-C. Chen, J. Feng, X. Zhang, R. B. Capaz, J. M. Tour, A. Zettl, S. G. Louie, et al., Nature Physics **7**, 616 (2011).

[368] M. K. Chan, Q. O. Hu, J. Zhang, T. Kondo, C. J. Palmstrøm, and P. A. Crowell, Physical Review B **80**, 161206 (2009).

[369] G. Salis, A. Fuhrer, and S. F. Alvarado, Physical Review B **80**, 115332 (2009).

[370] T. D. Nguyen, Y. Sheng, M. Wohlgenannt, and T. D. Anthopoulos, Synthetic Metals **157**, 930 (2007).

[371] T. Nguyen, G. Hukic-Markosian, F. Wang, L. Wojcik, X.-G. Li, E. Ehrenfreund, and Z. Vardeny, Nature Materials **9**, 345 (2010).

[372] R. E. Dietz and P. W. Selwood, Journal of Applied Physics **30**, S101 (1959).

[373] M. Boudart, J. A. Dumesic, and H. Topsøe, Proceedings of the National Academy of Sciences **74**, 806 (1977).

[374] R. Vollmer, T. Gutjahr-Löser, J. Kirschner, S. van Dijken, and B. Poelsema, Physical Review B **60**, 6277 (1999).

[375] M. Weinert and J. W. Davenport, Physical Review Letters **54**, 1547 (1985).

[376] P. Nordlander, S. Holloway, and J. K. Nørskov, Surface Science **136**, 59 (1984).

[377] J. K. Furdyna, Journal of Applied Physics **64**, 29 (1988).

[378] G. Bastard and R. Ferreira, Surface Science **267**, 335 (1991).

[379] D. Griffiths, *Introduction to quantum mechanics* (Pearson Prentice Hall, Upper Saddle Riverer, NJ 07458, 2005), 2nd ed.

[380] G. Mihajlović, S. I. Erlingsson, K. Výborný, J. E. Pearson, S. D. Bader, and A. Hoffmann, Physical Review B **84**, 132407 (2011).

[381] C. Weber, N. Gedik, J. Moore, J. Orenstein, J. Stephens, and D. D. Awschalom, Nature **437**, 1330 (2005).

[382] M. Wojtaszek, I. J. Vera-Marun, T. Maassen, and B. J. van Wees, arXiv preprint arXiv:1209.2365 (2012).

[383] B. Birkner, D. Pachniowski, A. Sandner, M. Ostler, T. Seyller, J. Fabian, M. Ciorga, D. Weiss, and J. Eroms, Physical Review B **87**, 081405 (2013).

[384] M. A. Cazalilla, A. Iucci, F. Guinea, and A. H. Castro Neto, arXiv preprint arXiv:1207.3135 (2012).

[385] C. Lee, X. Wei, J. W. Kysar, and J. Hone, Science **321**, 385 (2008).

[386] H. Dery, H. Wu, B. Ciftcioglu, M. Huang, Y. Song, R. K. Kawakami, J. Shi, I. Krivorotov, I. Zutic, and L. J. Sham, IEEE Transactions on Electronic Devices **59**, 259 (2012).

[387] J. H. Chen, C. Jang, S. Adam, M. S. Fuhrer, E. D. Williams, and M. Ishigami, Nature Physics **4**, 377 (2009).

[388] W. H. Wang, W. Han, K. Pi, K. M. McCreary, F. Miao, W. Bao, C. N. Lau, and R. K. Kawakami, Applied Physics Letters **93**, 183107 (2008).

[389] Y. Li, Ph.D. thesis, University of California, Riverside (2010).

[390] G. Wastlbauer and J. A. C. Bland, Advances in Physics **54**, 137 (2005).

[391] A. T. Hanbicki, B. T. Jonker, G. Itskos, G. Kioseoglou, and A. Petrou, Applied Physics Letters **80**, 1240 (2002).

[392] Q. O. Hu, E. S. Garlid, P. A. Crowell, and C. J. Palmstrøm, Physical Review B **84**, 085306 (2011).

[393] K. Ando, S. Takahashi, J. Ieda, H. Kurebayashi, T. Trypiniotis, C. H. W. Barnes, S. Maekawa, and E. Saitoh, Nature Materials **10**, 655 (2011).

[394] Y. Pu, J. Beardsley, P. M. Odenthal, A. G. Swartz, R. K. Kawakami, P. C. Hammel, E. Johnston-Halperin, J. Sinova, and J. P. Pelz, in review (2013).

[395] P. F. Carcia, A. D. Meinhaldt, and A. Suna, Applied Physics Letters **47**, 178 (1985).

[396] F. J. A. Den Broeder, H. C. Donkersloot, H. J. G. Draaisma, and W. J. M. De Jonge, Journal of Applied Physics **61**, 4317 (1987).

[397] F. J. A. Den Broeder, W. Hoving, and P. J. H. Bloemen, Journal of Magnetism and Magnetic Materials **93**, 562 (1991).

[398] M. T. Johnson, P. J. H. Bloemen, F. J. A. Den Broeder, and J. J. De Vries, Reports on Progress in Physics **59**, 1409 (1996).

[399] S. S. P. Parkin, N. More, and K. P. Roche, Physical Review Letters **64**, 2304 (1990).

[400] S. S. P. Parkin, R. Bhadra, and K. P. Roche, Physical Review Letters **66**, 2152 (1991).

[401] M. D. Stiles, Journal of Magnetism and Magnetic Materials **200**, 322 (1999).

[402] R. K. Kawakami, E. Rotenberg, H. J. Choi, E. J. Escorcia-Aparicio, M. O. Bowen, J. H. Wolfe, E. Arenholz, Z. D. Zhang, N. V. Smith, and Z. Q. Qiu, Nature **398**, 132 (1999).

[403] R. K. Kawakami, E. Rotenberg, E. J. Escorcia-Aparicio, H. J. Choi, J. H. Wolfe, N. V. Smith, and Z. Q. Qiu, Physical Review Letters **82**, 4098 (1999).

[404] M. D. Stiles and A. Zangwill, Physical Review B **66**, 014407 (2002).

[405] J. C. Sankey, Y. T. Cui, J. Z. Sun, J. C. Slonczewski, R. A. Buhrman, and D. C. Ralph, Nature Physics **4**, 67 (2007).

[406] S. Mangin, D. Ravelosona, J. A. Katine, M. J. Carey, B. D. Terris, and E. E. Fullerton, Nature Materials **5**, 210 (2006).

[407] W. B. Zeper, Ph.D. thesis, Technical University Twente, The Netherlands (1991).

[408] L. Néel, J. Phys. Radium **15**, 225 (1954).

[409] B. N. Engel, C. D. England, R. A. Van Leeuwen, M. H. Wiedmann, and C. M. Falco, Physical Review Letters **67**, 1910 (1991).

[410] C. A. F. Vaz, J. A. C. Bland, and G. Lauhoff, Reports on Progress in Physics **71**, 056501 (2008).

[411] J. M. Shaw, H. T. Nembach, T. J. Silva, S. E. Russek, R. Geiss, C. Jones, N. Clark, T. Leo, and D. J. Smith, Physical Review B **80**, 184419 (2009).

[412] N. Nakajima, T. Koide, T. Shidara, H. Miyauchi, H. Fukutani, A. Fujimori, K. Iio, T. Katayama, M. Nỳvlt, and Y. Suzuki, Physical Review Letters **81**, 5229 (1998).

[413] K. Yokoyama, Ph.D. thesis, University of California, Riverside (2009).